BERGISCHE
UNIVERSITÄT
WUPPERTAL

JÜLICH
FORSCHUNGSZENTRUM

Tomographic reconstruction of gravity wave parameters from satellite-borne airglow observations

Dissertation

zur Erlangung des Grades
Doktor der Naturwissenschaften (Dr. rer. nat.)

vorgelegt der

Bergischen Universität Wuppertal
Fakultät für Mathematik und Naturwissenschaften

von

Rui Song

Wuppertal, 2018

Die Dissertation kann wie folgt zitiert werden:

urn:nbn:de:hbz:468-20180316-101809-7
[http://nbn-resolving.de/urn/resolver.pl?urn=urn%3Anbn%3Ade%3Ahbz%
3A468-20180316-101809-7]

ABSTRACT

Gravity waves (GWs) play an important role in atmospheric dynamics. Especially in the mesosphere and lower thermosphere (MLT) dissipating GWs provide a major contribution to the driving of the global wind system. The scales of GWs are often too small for most general circulation models (GCMs) to be resolved, and the effect of GWs on the global circulation has to be parameterized in the models. Therefore global observations are needed to better constrain GW parameterizations, as well as the part of the GW spectrum that is explicitly resolved in GCMs. The small scales of GWs are, however, also a challenge for global observations from space.

Limb sounding is often used in satellite missions because it provides information about the middle atmosphere dynamics with a good vertical resolution. However, typical limb sounders have a poor horizontal resolution along the instruments' line-of-sight (LOS). Conversely, nadir sounders have a better horizontal resolution, but suffer from a poor vertical resolution. For this reason, the wave structures deduced from satellite observations are limited either in vertical or horizontal resolution due to the viewing geometry. In this thesis, novel satellite-borne observation strategies are investigated for the purpose of resolving 2-D or 3-D small-scale GW structures in the MLT region with unprecedented spatial resolution. The proposed observation strategies are simulated for an instrument measuring atmospheric temperatures from the rotational structure of O_2 A-band airglow emissions.

One observation mode is tailored to detect GWs in the mesopause region by combining limb and sub-limb measurements for improving the spatial resolution that conventional limb sounders can achieve. This observation mode works only for the layered emissions with high optical thickness in the lower atmosphere (e.g. O_2 A-band nightglow). A key element of this observation mode is the ability of the satellite to operate in so called 'target mode', i.e. to stare with the instrument's LOS at a particular point in the atmosphere and collect radiances at different viewing angles. These multi-angle

measurements of a selected region allow for a 2-D tomographic reconstruction of the atmospheric state, in particular of GW structures. Simulation results have shown that one major advantage of this observation strategy is that GWs can be observed on much smaller scale than conventional limb observations. The derived GW sensitivity function demonstrates that the 'target mode' observations are able to capture GWs with horizontal wavelengths as short as $\sim$50 km for a large range of vertical wavelengths. This is far better than the horizontal wavelength limit of 100-200 km obtained from conventional limb sounding.

Another observation strategy is proposed for a 3-D tomographic reconstruction of GWs by combining consecutive limb measurements from multiple horizontal directions. This observation strategy is applicable to any kind of airglow emissions, including layered and non-layered (e.g. O_2 A-band dayglow) emissions. It includes two different observation modes, namely the 'sweep mode A' and 'sweep mode B'. The basic idea of this observation strategy is to horizontally sweep the instrument's LOS such that the volume of interest can be observed from multiple directions. Simulation results have shown that the sweep modes are capable of reconstructing 3-D wave structures. The 'sweep mode A' combines forward-, backward-, and side-looking measurements for a 3-D tomographic retrieval of GWs. But this observation mode is only sensitive to GWs propagating perpendicularly to the orbital track. The 'sweep mode B' is based on a pseudo 3-D tomographic reconstruction technique. It reconstructs 3-D wave structures by combining the projected 2-D waves in the along- and across-track directions. Numerical results have shown that the horizontal resolution in both along- and across-track directions are affected by an adjustable turning angle, which can also adjust the spatial coverage of this observation mode. The 'sweep mode B' provides an unbiased estimation of the real horizontal wavelength of a wave, which can be further used to reduce the errors in deducing GW momentum flux, a parameter that is directly related to the potential driving of the background winds by GWs.

Contents

Chapter 1

Introduction

1.1 Atmospheric structure

The Earth is surrounded by a thin blanket of gases that we call the atmosphere. It is composed of a mixture of species such as nitrogen, oxygen, carbon dioxide, water vapor and ozone. The atmosphere is relatively thin compared to the size of the Earth, but it protects life on the Earth from harmful solar radiation. The lower part of the atmosphere is known as the homosphere (<100 km), in which the diffusion is dominated by turbulent mixing and the mixing ratio of inert gases tends to be independent of altitude. The region above 100 km is called heterosphere, where atmospheric species are fractionated according to the molecular weight, with lighter species concentrated in higher altitudes. Since the Earth's atmosphere is not uniform but has significant variations in temperature, it can be further divided into four layers according to their distinct temperature gradient: the troposphere, stratosphere, mesosphere and thermosphere.

Figure 1.1 shows a typical structure of the atmospheric temperature as a function of altitude. The temperature data is derived from the MSIS (Mass Spectrometer Incoherent Scatter) extended model (*Hedin*, 1991) (run at 51° N, 10° E, in May 2017). The boundaries between adjacent layers are defined as the tropopause, stratopause and mesopause, where the vertical gradient in the temperature profiles changes.

The troposphere is the layer closest to the Earth's surface and contains $\sim$85% of the mass of the total atmosphere. It extends from the surface to an altitude of 8 km near the poles and up to 18 km over the equator. During the day, the sunlight that reaches the Earth is partly reflected back to space by the surface or clouds. Most of the radiation, however, is absorbed by the Earth's surface. The heat stored by the absorption of solar radiation is transferred from the ground to the troposphere by long-wave radiation, heat conduction and convection. Tropospheric temperature decreases with altitude with a

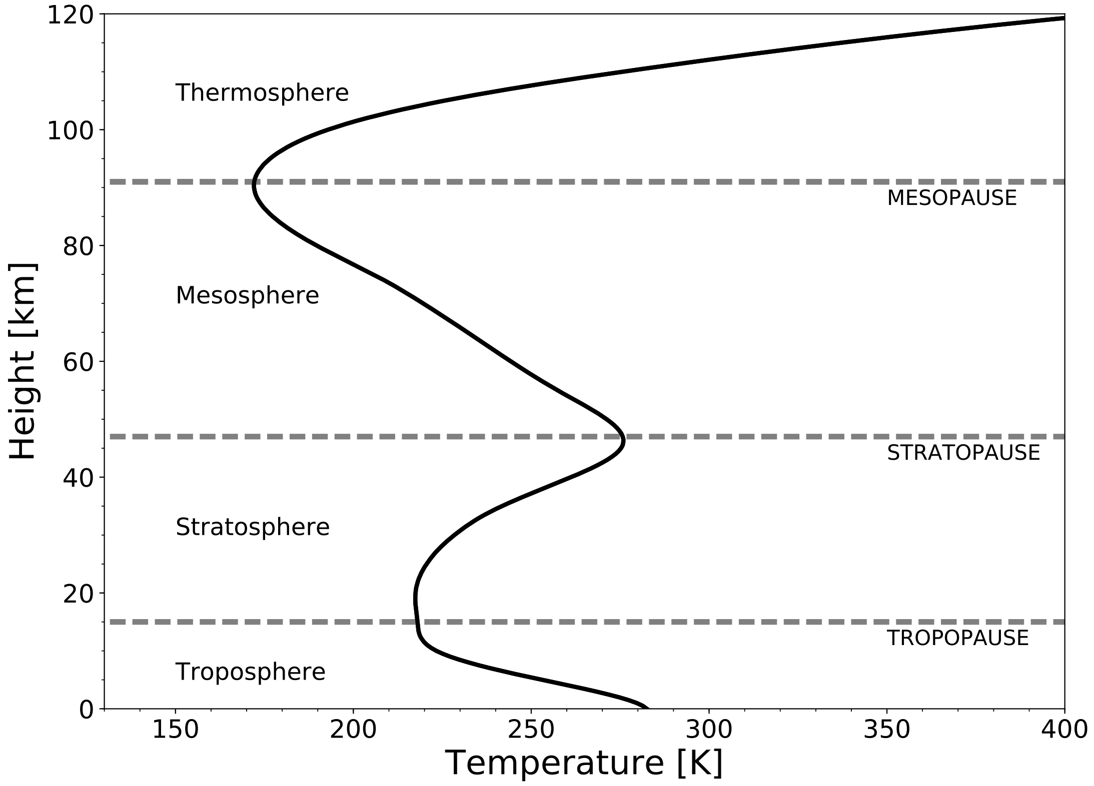

Figure 1.1: Atmosphere temperature structure (solid black curve) as a function of altitude, with labeled boundaries (dashed gray line). The data is taken from the MSIS-E-90 model run at 51° N, 10° E, in May 2017.

lapse rate of ∼6.5 K/km, mainly due to expansion and associated adiabatic cooling. The troposphere is capped by the tropopause, where the temperature gradient equals to zero.

The stratosphere extends above the tropopause to an altitude of ∼50 km. The stratosphere contains high concentrations of ozone and the absorption of ultraviolet (UV) radiation from the Sun by ozone is the main energy source for this layer. The cooling of the stratosphere is due to carbon dioxide that emits infrared radiation back to space. The temperature in the stratosphere rises with increasing altitude. Such a temperature structure creates a stable atmospheric condition with very little air mixing in the vertical direction. The stratopause caps the top of the stratosphere, separating it from the mesosphere above.

The mesosphere covers the region from ∼50 to 80 km above the Earth's surface. In the mesosphere temperature decreases with increasing altitude because the absorption of solar UV radiation by ozone falls off and, importantly, the strong emission of infrared radiation by carbon dioxide dominates the cooling in this region. A temperature minimum is reached in the mesopause region.

The thermosphere is located above the mesopause. The gas molecules are widely separated at this altitude. The few molecules in the thermosphere absorb much of the high-energy UV radiation and have a low collisional quenching rate, causing a rapidly increased temperature profile throughout the layer.

1.2 The dynamics in the mesosphere and lower thermosphere (MLT)

The altitude range of the mesosphere and lower thermosphere (MLT) covers between $\sim$50 and 110 km. It forms the upper part of the middle atmosphere, which extends from $\sim$10 to 110 km. The dynamics of the MLT is dominated by atmospheric waves including planetary waves, tides and gravity waves (GWs) (*Vincent*, 2015). The atmospheric waves are mainly excited in the lower atmosphere and propagate into the middle and upper atmosphere. The energy and momentum dissipation through GW breaking is the main driver for the large-scale circulation in the MLT region (*Lindzen*, 1981; *Holton*, 1982; *Garcia and Solomon*, 1985).

1.2.1 Atmospheric tides

Atmospheric tides can cause very large perturbations in the temperature, wind and density fields. In the MLT region, the amplitude of temperature perturbation induced by atmospheric tides can reach several tens of K. Atmospheric tides are primarily excited by solar heating in the troposphere and stratosphere, where the infrared radiation is absorbed by water vapor and UV radiation is absorbed by ozone, respectively. Atmospheric tides are also generated by the gravitational effect, but much smaller than those generated by solar heating (*Chapman and Lindzen*, 1970). The atmospheric tides with large amplitude are dominated by those with periods of 24 (diurnal) and 12 (semidiurnal) hours. However, tides with periods of 8 (terdiurnal) and 6 (quaterdiurnal) hours can be also observed with significant amplitude.

Atmospheric tides can be separated into two types: migrating and non-migrating solar tides. Migrating tides are sun synchronous such that they appear to move westwards from the point view of a ground based observer. Since migrating tides do not move relatively to the Sun, their influence on the atmosphere is therefore steady. The variations in tides observed from ground are caused by the Earth's rotation through a pattern that is fixed relative to the Sun. Seasonal variations of migrating tides can be observed as the Earth tilts within this pattern. In contrast, non-migrating tides do not follow the motion of the sun, they can move either eastwards or westwards relative to the sun. It is generally recognized there are two main excitation sources of non-migrating tides (*Miyoshi et al.*, 2017). First, thermal excitation associated with cumulus convection in the troposphere can generate non-migrating tides. The absorption of solar radiation in the atmosphere and at the surface has diurnal variation, producing diurnal variation in the cumulus convective activity. In cases where the convective activity has a zonally nonuniform structure, non-migrating tides are excited by the latent heat release (*Hagan and Forbes*, 2003). The other excitation source of non-migrating tides is the nonlinear interactions between two waves. For example, the nonlinear interaction between the stationary planetary wave and the migrating tide can generate two non-migrating tides (*Angelats i Coll and Forbes*, 2002).

1.2.2 Planetary waves

Planetary waves, known as Rossby waves, also cause large scale oscillations in the atmosphere. Since the Earth's rotation is responsible for the formation of such large scale waves, the horizontal wavelength of these waves is planetary. These waves have important effects on the dynamics and chemistry in the MLT. They shape in part the general circulation and transport chemical species in long horizontal distances.

Planetary waves can be divided into forced mode and free mode waves. Forced mode waves are stationary, mainly excited in the lower atmosphere by topography such as mountains and also by the heating contrasts between land and ocean. Free mode waves have periods close to the natural resonance of the atmosphere and are not maintained by forcing effects. Free mode waves are observed in periods of 2, 5, 10 and 16 days (*Mitchell et al.*, 1999; *Tunbridge et al.*, 2011; *Chen et al.*, 2011; *Ern et al.*, 2013; *Liu et al.*, 2015).

Planetary waves can cause sudden stratospheric warmings and the breakdown of the polar vortex during a final warming in the northern hemisphere. In the MLT region, planetary waves interact strongly with atmospheric tides and create a modulation of the tidal amplitudes at planetary wave periods (*Pancheva et al.*, 2000). There is also evidence that planetary waves play a role in filtering GWs (*Lieberman et al.*, 2013).

1.2.3 Atmospheric gravity waves (GWs)

Compared with atmospheric tides and planetary waves, GWs are short or mesoscale waves. Their horizontal scales range from tens to thousands of km. GWs are ubiquitous in the atmosphere with periods ranging from minutes to hours. GWs generated in the lower atmosphere transfer significant amount of energy and momentum into the MLT. The momentum deposition through wave breaking drives the large-scale circulation in the MLT.

Since buoyancy is the primary restoring force for this oscillation, atmospheric GWs can be also called buoyancy waves. Generally, the GWs are studied under the simplification of the linear theory. It provides the dispersion and polarization relations of GWs under linearized solutions of fluid dynamical equations. Details of the linear theory are given in *Fritts and Alexander* (2003). The GW dispersion relation can be written as

$$\hat{\omega}^2 = \frac{N^2(k^2+l^2)+f^2(m^2+\frac{1}{4H^2})}{k^2+l^2+m^2+\frac{1}{4H^2}} \tag{1.1}$$

where $\hat{\omega}$ is the intrinsic frequency of the wave, i.e. the frequency relative to the background flow. (k,l,m) are the wavenumber components, N is the buoyancy frequency, f is the Coriolis parameter and H is the scale height. This GW dispersion relation can be transformed as

$$m^2 = \frac{(k^2+l^2)(N^2-\hat{\omega}^2)}{(\hat{\omega}^2-f^2)} - \frac{1}{4H^2} \tag{1.2}$$

This dispersion relation relates the intrinsic frequency of a wave to the spatial structure (k,l,m) and to the properties of the background atmosphere. The solution allows for GWs with a broad range of properties. Given a GW propagating vertically, the wavenumber k,l,m are real and the intrinsic frequency must be confined to the range $N > \hat{\omega} > |f|$. All parts of this spectrum are important for the dynamics of the middle atmosphere. Since the properties of a wave can vary strongly during the propagation through the atmosphere, models describing the wave propagation across a wide range of conditions need to retain all terms in Eq. 1.1 in their analysis. However, simplified forms can be used to represent waves in certain limited regions of the spectrum. They are high-frequency waves ($\hat{\omega} \gg f$), medium-frequency waves ($N \gg \hat{\omega} \gg f$) and low-frequency waves ($\hat{\omega} \sim f$), respectively. The derivation of simplified forms are summarized in *Fritts and Alexander* (2003).

The generation mechanisms of GWs in the lower atmosphere have been extensively studied. The dominant sources of GWs include orography, convection and wind shear. GWs have strong effects on the dynamical and thermal structure of the atmosphere, including larger scale waves (tides and planetary waves) and background winds. These cumulative impacts induced by GWs are of global scale. However, the scale of individual GW can be rather small (a few km), which may pose a challenge for both observations and models. In the next section, current technologies for the observations of GWs are introduced.

1.3 Observations of GWs in the atmosphere

Ideally, a GW can be tracked from the source in the lower atmosphere to the region where it dissipates energy and momentum. However, this requirement can hardly be achieved for several reasons. First, the entire vertical range of a GW event may extend from the lower atmosphere up to the mesosphere. This large vertical range can not be easily covered by individual measuring systems. In addition, the vertical propagation of GWs is often accompanied by a horizontal motion. This will result in a wave moving beyond the ranges where the observation regions are located. Likewise, the short periods (down to a few minutes) and small scales (down to a few km) of GWs are also challenges for current observation technologies. Therefore, different instruments have been developed in the last decades for the observation of GWs, which are summarized in the following:

Ground-based instruments are limited in geographic extent but can provide information about local time variations and small horizontal variations of GWs. They obtain this information by various techniques, one of them being passive optical sounding of the airglow emissions. In the MLT, chemical processes at different altitudes produce various airglow emissions. Typical airglows in the MLT include hydroxyl Meinel (emission altitude around 87 km), the oxygen atmospheric band (emission altitude between 91 and 95 km), the sodium D line (emission altitude around 90 km) and the oxygen green line emissions (emission altitude between 95 and 100 km). Since the photons emitted by airglow are overlaid by scattered sunlight during day time, ground-based airglow observations are limited to nighttime with a clear-sky condition. In recent decades, there are a number of studies showing the temperature and wave characteristics in the MLT observed by passive ground-based instruments (*Nakamura et al.*, 1999; *Pautet and Moreels*, 2002; *Suzuki et al.*, 2004, 2010; *Kalicinsky et al.*, 2016). In addition to passive instruments, active ground-based instruments, e.g. medium frequency (MF) radars (*Hoffmann et al.*, 2010, 2011) and meteor radars (*Fritts et al.*, 2010; *Placke et al.*, 2011), are also used to give information about local time variations of GWs. Although various networks of ground-based stations have been built to increase the spatial coverage of the observations, they are still far from providing a global view of atmospheric dynamics in the MLT.

Recent advances in satellite instrumentation made it possible to measure GWs from a global perspective, allowing for identification of their spectral characterization and geographic distribution (*Preusse et al.*, 2002; *Wu*, 2004; *Ern et al.*, 2004; *Hoffmann and Alexander*, 2009; *Ern et al.*, 2017). Basic properties of GWs (e.g. amplitudes, wavelengths and phases) can be extracted from the observed temperature fields. As a valuable indicator to identify and quantify GWs, temperature is often measured in satellite-borne atmospheric sounders, including both limb sounder and nadir sounder.

Limb sounding is used in many satellite missions because it provides important information about the middle atmosphere dynamics with a good vertical resolution ($\sim$1-3 km). The Limb Infrared Monitor of the Stratosphere (LIMS) provided temperature profiles between 15 and 60 km at a vertical resolution of 1.8 km (*Remsberg et al.*, 2004). Utilizing LIMS data, *Fetzer and Gille* (1994) derived temperature variances caused by GWs with vertical wavelengths of $\sim$6-50 km and horizontal wavelengths longer than $\sim$200 km. Global Positioning System (GPS) signals can be used to derive the temperature in the altitude range of $\sim$15-40 km with the radio occultation technique (*Rocken et al.*, 1997). The derived temperature perturbations have been used by *Tsuda et al.* (2000) to extract mesoscale GWs with vertical wavelengths of $\sim$2-10 km. The Cryogenic Infrared Spectrometers and Telescopes for the Atmosphere (CRISTA) delivered temperature data from $\sim$20 to 80 km, and GWs with vertical wavelengths of $\sim$5-25 km and $\sim$6-30 km were derived from CRISTA-1 and CRISTA-2, respectively (*Eckermann and Preusse*, 1999; *Preusse et al.*, 2002). With its high vertical resolution ($<$1 km), the High Resolution Dynamics Limb Sounder (HIRDLS) data gave information about GWs with vertical wavelengths of $\sim$2-16 km in the altitude range of $\sim$20-60 km (*Alexander et al.*, 2008; *Ern et al.*, 2011). Compared to limb soundings, nadir soundings have a better horizontal resolution, but suffer from a poor vertical resolution. They include the Advanced Microwave Sounding Unit (AMSU) (*Wu*, 2004) and the Atmospheric Infrared Sounder (AIRS) (*Alexander and Barnet*, 2007; *Hoffmann and Alexander*, 2009; *Ern et al.*, 2017).

Space-borne instruments provide a global view of the middle atmosphere dynamics. However, the deduced wave structures are limited either in vertical or horizontal resolution due to the viewing geometry. In very recent years, new observation strategies have been used on airborne platforms, e.g. the German research aircraft HALO (High Altitude and Long Range Research Aircraft) and the Russian aircraft Geophysica, to demonstrate a way forward for satellite observations. GLORIA (Gimballed Limb Observer for Radiance Imaging of the Atmosphere) is a new remote sensing infrared limb sounder operated on the HALO aircraft (*Riese et al.*, 2014). Since the GLORIA instrument is capable of adjusting its viewing direction in specific patterns, it allows to view the same atmospheric volume repeatedly from multiple angles. Three-dimensional (3-D) atmospheric structures can be reconstructed from such observations using tomographic retrieval schemes. This observation scenario on GLORIA was proposed by *Ungermann et al.* (2011) and applied by *Kaufmann et al.* (2015) and *Krisch et al.* (2017).

The flexibility provided by the airborne instruments makes the reconstruction of GWs in a real 3-D atmospheric volume possible. However, the vertical range, as well as the horizontal coverage of the observed atmospheric volume, is limited by the maximum height that the aircraft can reach. In addition, aircraft observations are often limited by flight hours because of the expense. Currently, there is no satellite in orbit that can measure 3-D small-scale atmospheric structures with a good vertical resolution globally.

Therefore, in this thesis novel satellite-borne observation strategies to detect 2-D and 3-D small-scale atmospheric structures are proposed. Specifically, a ‘target mode’ for measuring 2-D atmospheric structures in the mesopause region, and two ‘sweep modes’ for measuring 3-D atmospheric structures in the MLT region are proposed, respectively. The ‘target mode’ works only for the layered emissions with high optical thickness in the lower atmosphere, and the ‘sweep modes’ are applicable to any kind of emissions.

1.4 Chapter summary

This chapter introduced the basic structure of the Earth’s atmosphere. According to the temperature gradient, the atmosphere can be divided into four layers: the troposphere, stratosphere, mesosphere and thermosphere. The mechanisms relevant for the energy absorption and release in each layer were discussed. The atmosphere is defined as the mesosphere and lower thermosphere (MLT) in the altitude range between 50 and 110 km. This region is highly affected by atmospheric waves, including planetary waves, tides and GWs, which are mainly excited in the lower atmosphere.

Although GWs are short or mesoscale waves, they play an important role in driving the large-scale circulation in the MLT. The major techniques for the observation of GWs were summarized, including ground-based, air-borne and satellite-borne observations. These observations have their distinct advantages in resolving GW structures, but are often limited either in spatial coverage or resolution. The development of novel observation strategies to derive 2-D or 3-D small-scale GWs with a global coverage is therefore highly desirable.

Chapter 2

Temperature measurements from O_2 A-band airglow observations

In this thesis, the envisaged satellite-borne observation strategies use the rotational structure of airglow emissions to derive temperature and wave characteristics in the MLT region. This requires the emitting states of the airglow should be long-lived, and the rotational distribution should be thermalized, so that it can be described by the kinetic temperature. It is best, if this emission is visible for nadir or sub-limb sounding during nighttime, so that the volume of interest can be observed at multiple viewing angles. This requires that the observed emission is restricted to a limited altitude range and that any emission from lower parts of the atmosphere or the Earth's surface cannot reach the instrument. Thus, the atmosphere below the emission layer needs to be optically thick for those emissions. This limits the number of potential airglow emissions significantly, because most of them are hotband transitions between two excited vibrational states. The number density of the lower state of a hotband transition is typically too low to absorb background radiation from the lower atmosphere. Therefore we have to search for airglow emissions, whose lower state is a ground state of a frequent atmospheric species. This is the case for the oxygen atmospheric band (O_2 A-band) airglow emission at 762 nm, which is visible during both day- and nighttime. In this chapter, the production and loss mechanisms of the O_2 A-band airglow are presented, along with the model that simulates airglow perturbations induced by atmospheric GWs. The rotational structure of this airglow emission and its radiative transfer through the atmosphere are also discussed. The forward model and retrieval scheme have been developed in order to simulate the processes of deriving the temperature from satellite-borne observations.

2.1 O_2 A-band airglow emission

The O_2 A-band emission refers to the transition from the second excited state $O_2(b^1\Sigma)$ to the ground state $O_2(X^3\Sigma)$. It centers at the wavelength of 762 nm with a life time of $\sim$12 s. The main production and loss processes of the $O_2(b^1\Sigma)$ were given by *Bucholtz et al.* (1986). The main sources for the production of $O_2(b^1\Sigma)$ can be summarized as: 1) resonant absorption in A-band and B-band; 2) quenching from the $O(^1D)$ that was produced in the photolysis of O_2 and O_3; 3) a two-step Barth process. A schematic of the mechanisms associated with O_2 A-band airglow emission is illustrated in Fig. 2.1.

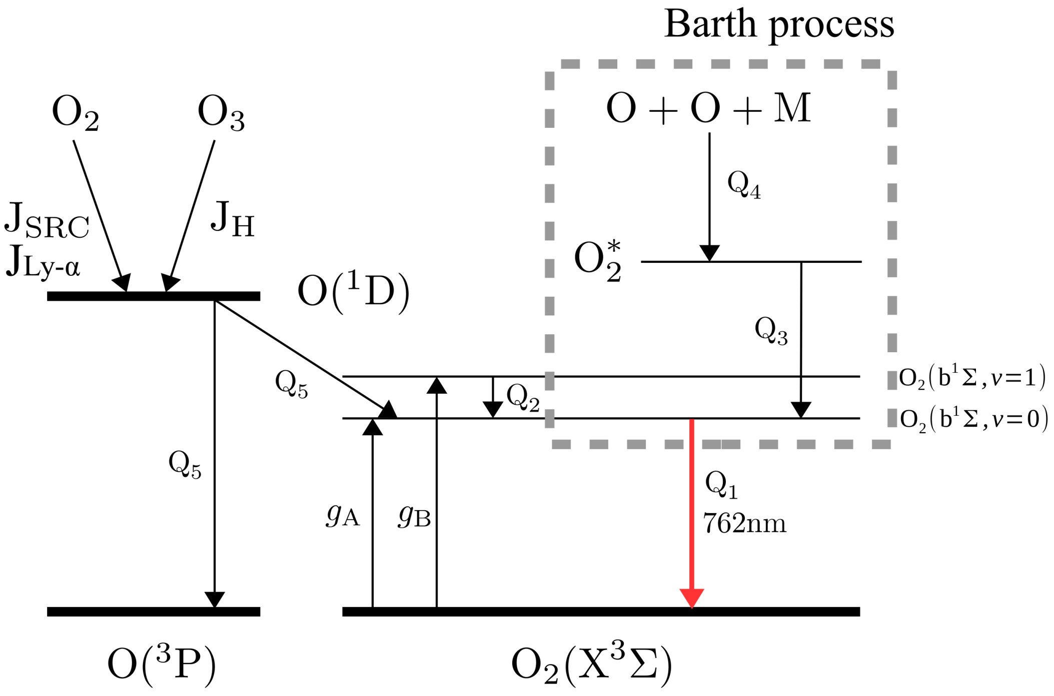

Figure 2.1: Mechanisms associated with the production of O_2 A-band airglow. The photochemical reaction coefficient are represented by factor J and g, and the collisional quenching rates are represented by Q. J_{SRC} and $J_{Ly\text{-}\alpha}$ are the photolysis frequencies of O_2 in the Schumann-Runge Continuum (SRC) and in the Lyman-α line, respectively. J_H is the photolysis frequency of O_3 in the Hartley band.

2.1.1 Production and loss mechanisms

First, O_2 in the ground state can be excited by the absorption of solar radiation and produce $O_2(b^1\Sigma)$. The $O_2(X^3\Sigma)$ absorbs photons in the A-band (762 nm) and B-band (689 nm), respectively. Since the excited oxygen with vibrational state 1 can be rapidly deactivated to state 0 before being quenched into the ground state, it should also be accounted for as part of the A-band emission.

$$O_2 + h\upsilon(762nm) \xrightarrow{g_A} O_2(b^1\Sigma, v = 0) \tag{2.1}$$

$$O_2 + h\upsilon(689nm) \xrightarrow{g_B} O_2(b^1\Sigma, v = 1) \tag{2.2}$$

where g_A and g_B are the solar excitation rates at 762 nm and 689 nm, respectively. The calculations of g-factors are carried out by evaluating the absorption coefficients on a line-by-line basis and integrating over the spectral domain. A detailed description and relevant equations for calculating g-factors can be found in *Bucholtz et al.* (1986). Following the equations, altitude dependent g-factors can be derived in both A-band and B-band. The results show that the A-band dominates the production of $O_2(b^1\Sigma)$ due to the resonance absorption in all altitudes because the calculated g_A value is roughly one order of magnitude larger than g_B. It was also found that the variations of g-factors in different altitudes are very small above 60 km and can be neglected without losing accuracy above 70 km. A typical value of 5.94×10^{-9} and 3.54×10^{-10} are used for the estimation of g_A and g_B in the MLT, respectively (*Christensen et al.*, 2012). After the g-factors are obtained, the $O_2(b^1\Sigma)$ produced by resonant absorption can be calculated as the sum of the A-band excitation and B-band excitation:

$$P_{\mathrm{res}} = g_A[O_2] + P_B \tag{2.3}$$

where $g_A[O_2]$ denotes the part produced by direct A-band absorption, and P_B is the part due to deactivation of $O_2(b^1\Sigma, v = 1)$. P_B can be further calculated as

$$P_B = \frac{K\, g_B[O_2]}{A_{771} + K + k_{3B}[O_3]} \tag{2.4}$$

where A_{771} is Einstein A coefficient for spontaneous emission of the O_2 (1-1) band at 771 nm, and K is calculated as

$$K = k_{0B}[O] + k_{1B}[O_2] + k_{2B}[N_2] \tag{2.5}$$

All the k values that appear in Eq. 2.4 and Eq. 2.5 represent the quenching coefficients and the values are given in A.2.

Collisions between $O(^1D)$ and O_2 in the ground state are another source of $O_2(b^1\Sigma)$.

In the mesosphere, there are two main sources of $O(^1D)$: photodissociation of O_3 in the Hartley band and photodissociation of O_2 in the Schumann-Runge Continuum (SRC) and in the Lyman-α line,

$$O_2 + h\upsilon \xrightarrow{J_2} O(^1D) + O(^3P) \tag{2.6}$$

$$O_3 + h\upsilon \xrightarrow{J_3} O(^1D) + O_2(^1\Delta) \tag{2.7}$$

where J_2 and J_3 are the photolysis frequencies of O_2 and O_3, respectively. In the photochemical equilibrium state, the concentration of $O(^1D)$ in the mesosphere is calculated as

$$[O(^1D)] = \frac{J_2[O_2] + J_3[O_3]}{A_{1D} + k_1[O_2] + k_2[N_2]} \tag{2.8}$$

where A_{1D} is the Einstein A coefficient of $O(^1D)$, k_1 and k_2 are the rate coefficients for the quenching by O_2 and N_2, respectively. The concentration of $O_2(b^1\Sigma)$ excited through the collision with $O(^1D)$ can be calculated after the concentration of $O(^1D)$ is known,

$$P_{O(^1D)} = \varphi k_1[O(^1D)][O_2] \tag{2.9}$$

where k_1 is the rate constant, φ is the efficiency of this process.

The last process of producing $O_2(b^1\Sigma)$ is a two-step Barth process (*McDade et al.*, 1986; *Murtagh et al.*, 1990). Since the Barth-process is independent of solar radiation, it contributes to the production of $O_2(b^1\Sigma)$ both in daytime and nighttime. This process consists of a 3-body recombination by atomic oxygen,

$$O + O + M \longrightarrow O_2^* + M \tag{2.10}$$

$$O_2^* + O_2 \longrightarrow O_2(b^1\Sigma) + O_2 \tag{2.11}$$

Since O_2^* can be also quenched by atomic oxygen, the concentration of $O_2(b^1\Sigma)$ produced by the Barth-process can be calculated as

$$P_{\mathrm{Barth}} = \frac{k_5[O]^2[O_2][M]}{C_{O_2}[O_2] + C_O[O]} \tag{2.12}$$

where k_5 is the rate coefficient of Reaction 2.10 and 2.11, $C_{O_2}[O_2]$ and $C_O[O]$ are the quenching coefficients of O_2 and O, respectively. The effect of quenching by N_2 is included in $C_{O_2}[O_2]$.

The total concentration of $O_2(b^1\Sigma)$ can be estimated by combining the contributions from the three sources mentioned above,

$$[O_2(b^1\Sigma)] = P_{res} + P_{O(^1D)} + P_{Barth} \tag{2.13}$$

If the considered condition is nighttime, the Barth-process is the only source that will produce $O_2(b^1\Sigma)$. Then the calculation of $O_2(b^1\Sigma)$ concentration can be simpler,

$$[O_2(b^1\Sigma)] = P_{Barth} \tag{2.14}$$

At last, the O_2 A-band volume emission rate, i.e. the photons emitted from the $O_2(b^1\Sigma)$ in the A-band region, can be calculated,

$$\eta = \frac{F_c A_{1\Sigma}[O_2(b^1\Sigma)]}{A_{1\Sigma} + k_0[N_2] + k_3[O_3] + k_4[O_2] + k_6[O]} \tag{2.15}$$

where F_c is the transition probability of this process, $A_{1\Sigma}$ is the Einstein A coefficient of A-band emission, and k values are quenching coefficients. All the values of rate coefficients used for the calculation of O_2 A-band emission are given in the Appendix. A.2.

2.1.2 Photolysis rates

As presented in the previous section, the main mechanisms for the production of $O(^1D)$ during daytime are the photodissociations of O_2 (Reaction 2.6) and O_3 (Reaction 2.7). Given an altitude z, the photolysis rate of an absorb at this altitude can be represented as

$$J(z) = \int F(\tilde{\nu}, z)\sigma_i(\tilde{\nu})\phi(\tilde{\nu})d\tilde{\nu} \tag{2.16}$$

where $F(\tilde{\nu}, z)$ is the actinic flux at altitude z, $\sigma_i(\tilde{\nu})$ the absorption cross section within the spectral interval, $\phi(\tilde{\nu})$ the quantum yield. The value of $F(\tilde{\nu}, z)$ is calculated from the actinic flux at the top of the atmosphere $F(\tilde{\nu}, \infty)$,

$$F(\tilde{\nu}, z) = F(\tilde{\nu}, \infty)e^{-\int_z^\infty \sigma_i(s)n_i(s)ch(\chi)ds} \tag{2.17}$$

where $n_i(s)$ is the number density of the absorber at position s. The exponential term $\int_z^\infty \sigma_i(s)n_i(s)ch(\chi)ds$ in Eq. 2.17 denotes the optical depth, integrating from the altitude z to the top of the atmosphere. The factor $ch(\chi)$ takes into account the effects of the Sun's position and the Earth's curvature (*Smith and Smith*, 1972; *Rodrigo et al.*, 1986), and can be approximated as

$$ch(\chi) = \left[\frac{1 - R^2 \sin(\chi)^2}{(R+z)^2}\right]^{-\frac{1}{2}} \tag{2.18}$$

where R is the Earth's radius, z is the altitude and χ is the solar zenith angle. The photolysis rates can be calculated from Eq. 2.17 and Eq. 2.18. The photolysis of O$_2$ is due to the absorption in the Schumann Runge Continuum (SRC) between 137-175 nm (J_{SRC}) and the Lyman-α line at 121.6 nm ($J_{\text{Lyman-}\alpha}$). Therefore, the overall O$_2$ photolysis frequency J_2 is calculated as

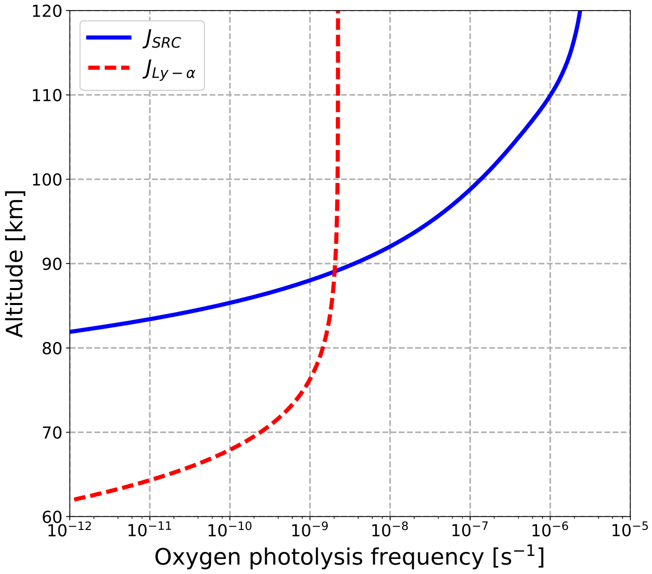

Figure 2.2: Contributions of Schumann Runge Continuum (SRC) and Lyman-α line to the O$_2$ photolysis. The background atmosphere is taken from the HAMMONIA model, run at 30° N and 140° W for 14:30 local solar time.

$$J_2 = J_{\mathrm{SRC}} + J_{\text{Lyman-}\alpha} \tag{2.19}$$

where both J_{SRC} and $J_{\text{Lyman-}\alpha}$ can be estimated individually following Eq. 2.16.

Figure 2.2 shows the contribution of the SRC and the Lyman-α line to the O$_2$ photolysis rate at a solar zenith angle of 0°. The number densities of O$_2$ are taken from the HAMMONIA model. As shown in Fig. 2.2, the SRC dominates the O$_2$ photolysis above 90 km. Whereas in the mesosphere, the contribution from the $J_{\text{Lyman-}\alpha}$ line is more important, especially between 70 and 80 km.

In addition, the effect of solar zenith angle (SZA) on the O$_2$ photolysis rate is ana-

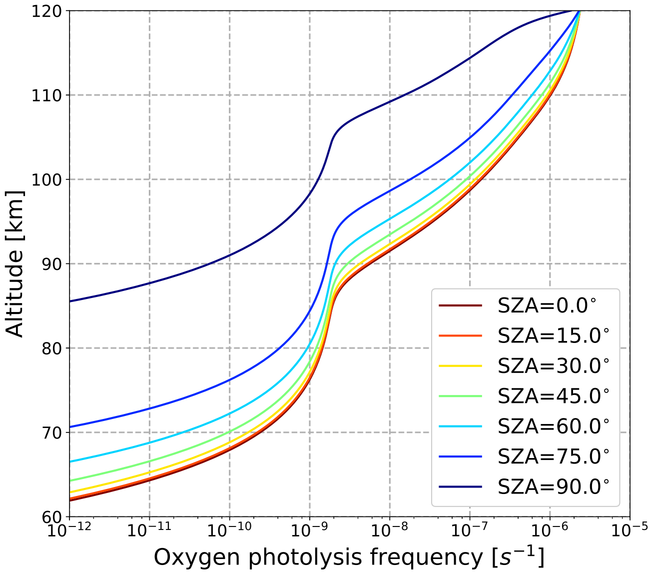

Figure 2.3: O_2 photolysis rates at different solar zenith angles. The atmosphere condition is the same as in Fig. 2.2.

lyzed in Fig. 2.3. As expected, higher solar zenith angles cause a decline of the photolysis rate J_2 because the attenuation of actinic flux on its way through the atmosphere is increased in longer slant paths. At the altitude of 90 km, J_2 with a solar zenith angle of 0° is 100 times larger than 90°.

The photolysis rate of O_3 (J_3) is calculated in the same way as O_2. The absorption region responsible for the photolysis of O_3 is the Hartley band, between 198 and 310 nm. The altitude dependence of J_3 is relatively weak compared with J_2. Typically, the J_3 has a constant value of $\sim 7.1 \times 10^{-3}$ s^{-1} in the MLT.

2.1.3 Volume emission rate

The total volume emission rate of O_2 A-band airglow can be calculated using Eq. 2.1 - Eq. 2.19. The background atmosphere, including the temperature T and the number densities of various constituents, is taken from the HAMMONIA model. Fig. 2.4 show the vertical profile of N_2, O_2, O_3 and atomic oxygen number densities at noon (a) and midnight (b) condition, respectively. Since the mixing ratios of N_2 and O_2 are fairly uniform up to the mesopause, their number densities decrease exponentially with altitude. However, the number density of O_3 and atomic oxygen are highly affected by the abundance of solar radiation. The difference of [O] between noon and midnight is largest below 85 km, where [O] drops rapidly for the midnight condition. In con-

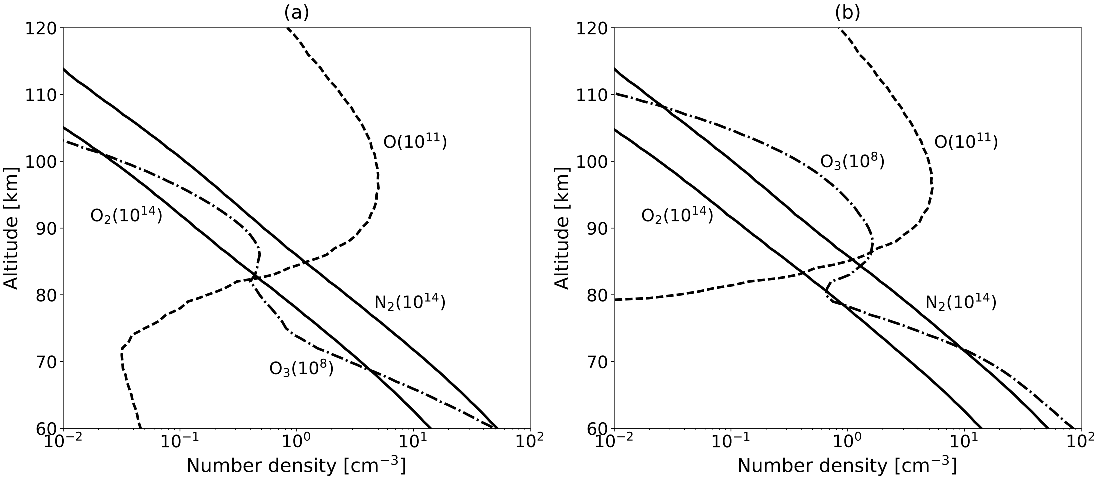

Figure 2.4: Number density of N_2, O_2, O_3 and atomic oxygen at altitudes between 60 and 120 km at noon (a) and midnight (b) condition. The data are taken from the HAMMONIA model, run at 30° N and 180° E for daytime (a), and 30° N and 0° E for nighttime (b).

trast, [O_3] is less abundant at noon because a part of O_3 is consumed by the photolysis reaction.

Based on this atmospheric state, the O_2 A-band volume emission rate can be modelled for daytime condition as shown in Fig. 2.5 (a), and nighttime condition in Fig. 2.5 (b), respectively. The atmospheric conditions are the same as in Fig. 2.4. The total volume emission rates as well as the contributions from different sources are calculated following the airglow emission model presented in the previous section. In the daytime all the processes are active, whereas in the nighttime only the Barth process contributes to the the total emission. As shown in Fig. 2.5 (a), the collision with $O(^1D)$ produced by the photolysis of O_2 is the major source of the emission in the altitude above 95 km. Below 95 km, the A-band resonant absorption predominates the production of $O_2(b^1\Sigma)$. At nighttime, the total emission is produced by the Barth mechanism and peaks at $\sim$ 93 km. Below this peak altitude, the decrease in the emission is due to the declining abundance of atomic oxygen. Above this peak altitude, the number density of O_2 decreases with increasing altitude, and therefore less O_2^* can be quenched to produce $O_2(b^1\Sigma)$.

2.1.4 Rotational structure of the O_2 A-band emission

Since the lifetime of the $O_2(b^1\Sigma)$ state is more than 12 s, it can be assumed that the molecule is in rotational local thermodynamic equilibrium (*Vallance Jones*, 1974). This

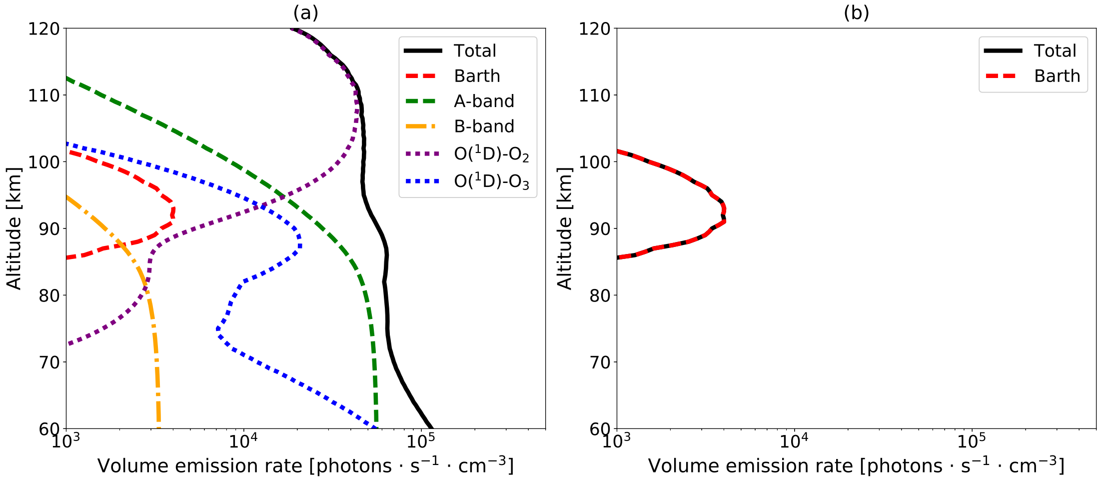

Figure 2.5: Modeled vertical profile of O_2 A-band volume emission rates at altitudes between 60 and 120 km at noon (a) and midnight (b), respectively. The background atmosphere that is taken from the HAMMONIA model is the same as in Fig. 2.4. A-band and B-band (dashed green line and dot-dashed orange line, respectively) are the contributions from the resonant absorption. $O(^1D)$-O_2 and $O(^1D)$-O_3 (dotted purple line and blue line, respectively) are the contributions from the collision with $O(^1D)$. The dashed red line is the contribution from the Barth process. The black curve denotes the total A-band emission.

allows to derive the kinetic temperature of the atmosphere from the rotational band structure of the emissions. Under thermal equilibrium conditions, the O_2 A-band rotational excitation follows the Boltzmann distribution at a rotational temperature T, which is assumed to be equal to the background temperature. The number of photons that appears in an individual rotational line is given by η_{rot}:

$$\eta_{\text{rot}} = \eta \frac{g'}{Q(T)} \exp(\frac{-hcE'}{kT}) A_i \tag{2.20}$$

where h is the Planck constant, c is the speed of light, k is the Boltzmann constant. E' and $g'$are the upper state energy and upper state degeneracy, respectively. A_i is the Einstein coefficient of the transition. All these parameters within the A-band are derived from the 2016 edition of the HITRAN (High Resolution Transmission) database (*Gordon et al.*, 2017), and also given in A.1. $Q(T)$ is the rotational partition function that is written as

$$Q(T) = \sum g' \exp(\frac{-hcE'}{kT}) \tag{2.21}$$

Figure 2.6 shows the rotational structure of the O_2 A-band emission at different tem-

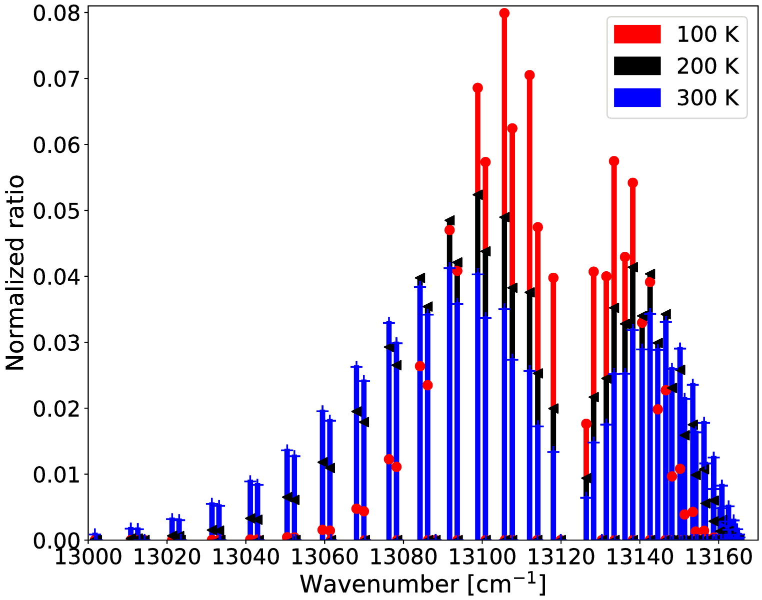

Figure 2.6: The rotational structure of O_2 A-band emission at 100, 200 and 300 K. The data is taken from the HITRAN2012 database. At each temperature, the distribution function is normalized to the sum of all the lines in the spectrum.

perature values: 100, 200 and 300 K. At each temperature, the distribution function is normalized to the sum of all the lines in the spectrum. At low temperature conditions, the emissions are concentrated near the center of the spectrum. The higher rotational levels become more populated when the temperature increases, and the emission disperses to the wings of the spectrum as shown in Fig. 2.6. In other words, the emissions at different wavenumbers have different temperature dependences. In fact, a subset of six emission lines has proven to give an optimal setup for a potential satellite mission aiming to the derivation of kinetic temperature from the O_2 A-band (*Deiml et al.*, 2017). They include emission lines at wavenumbers of 13084.20, 13086.13, 13091.71, 13093.66, 13098.85 and 13100.82 cm^{-1}. The six lines show both positive and negative temperature dependence of rotational structures. They can be individually measured to derive the temperature without an absolute calibration. The temperature dependence of these six lines between 150 and 300 K are shown in Fig. 2.7.

2.1.5 Airglow perturbations induced by GWs

The intensity of airglow is perturbed away from the stable state when the GW penetrates into the emission layer in the middle atmosphere. This perturbation of the airglow in-

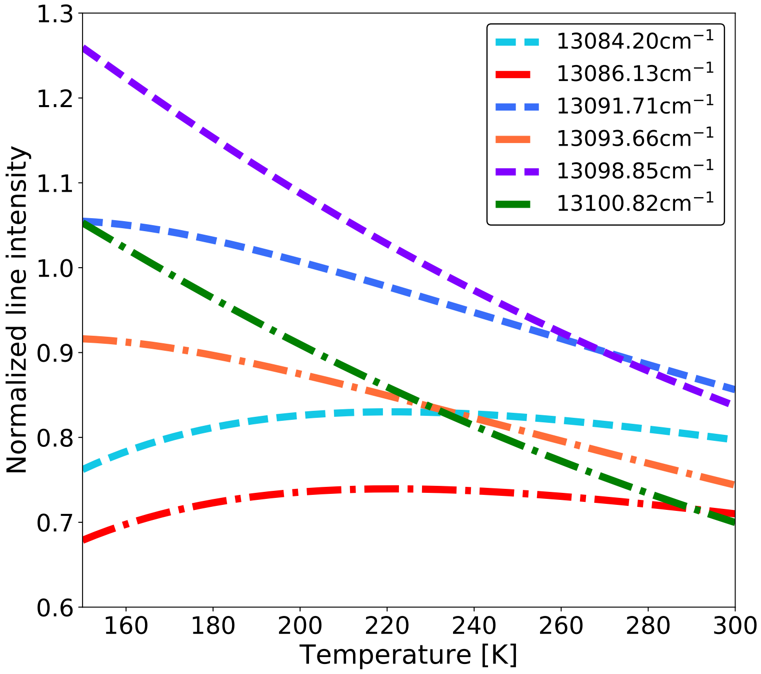

Figure 2.7: Temperature dependence of the six rotational lines of the O_2 A-Band emission between 150 and 300 K. The center wavenumbers for the lines are given in the figure legend. The intensity is normalized at the wavenumber of 13098.85 cm^{-1} for a temperature of 230 K.

tensity can occur because the atmospheric temperature and constituents relevant for the investigated emissions are perturbed by the wave. In this section, a model that describes the relations between the GW and O_2 A-band airglow perturbations is presented.

Following conventional assumption, we consider an adiabatic and windless atmosphere. A monochromatic wave perturbation added in the background temperature T_0 at position (x,z) can be written as (*Fritts and Alexander*, 2003),

$$T(x,y,z,t) = T_0(x,y,z,t) + A\cos\left(\frac{2\pi x}{\lambda_x} + \frac{2\pi y}{\lambda_y} + \frac{2\pi z}{\lambda_z} - \hat{\omega} t\right) \tag{2.22}$$

where A is the wave amplitude, λ_z the vertical wavelength, λ_x and λ_y the horizontal wavelengths in x and y directions, respectively. $\hat{\omega}$ is the ground-relative (Eulerian) frequency, which equals to the the intrinsic frequency in the case of a windless atmosphere. We used the following expression (*Ward*, 1999) to calculate the vertical displacement

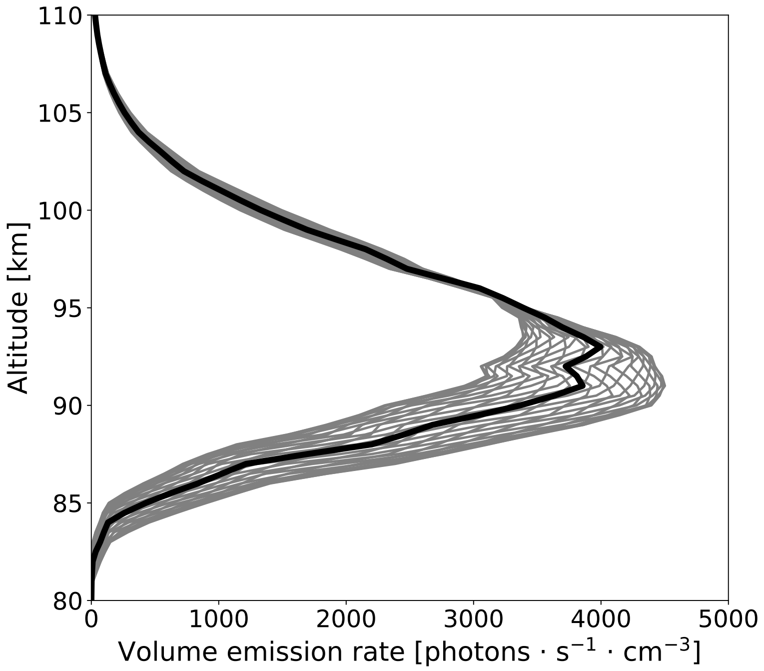

Figure 2.8: Unperturbed (thick solid line) and perturbed (thin gray lines) O_2 A-band night volume emission rates. The background atmosphere is taken from the HAMMONIA model run at midnight. The GW is generated with a vertical wavelength of 25 km and an amplitude of 10 K. The gray curves represent the airglow perturbed by a GW at 24 different phases, each 15° apart.

δz of an air parcel from its equilibrium height $z+\delta z$:

$$T(x,z,\delta z) \approx T(x,z) + (\Gamma_{ad} - \Gamma)\delta z \tag{2.23}$$

where Γ and Γ_{ad} are the local and adiabatic lapse rates, respectively. Then, the perturbed density (background density plus perturbation) ρ' at fixed height z can be calculated as density at equilibrium height $z+\delta_z$:

$$\rho'(x,z) = \rho(x,z,\delta z) \approx \rho(x,z)\exp^{-\kappa\delta z/H} \tag{2.24}$$

with the scale height H. In the quantity $\kappa = (c_p/c_v - 1)$, c_p and c_v represent heat capacities at constant pressure and volume, respectively. Given ρ', the number densities for perturbed major gases are calculated as (*Liu*, 2003; *Vargas et al.*, 2007):

$$\frac{[N_2]'}{[N_2]} = \frac{[O_2]'}{[O_2]} = \frac{\rho'}{\rho} \tag{2.25}$$

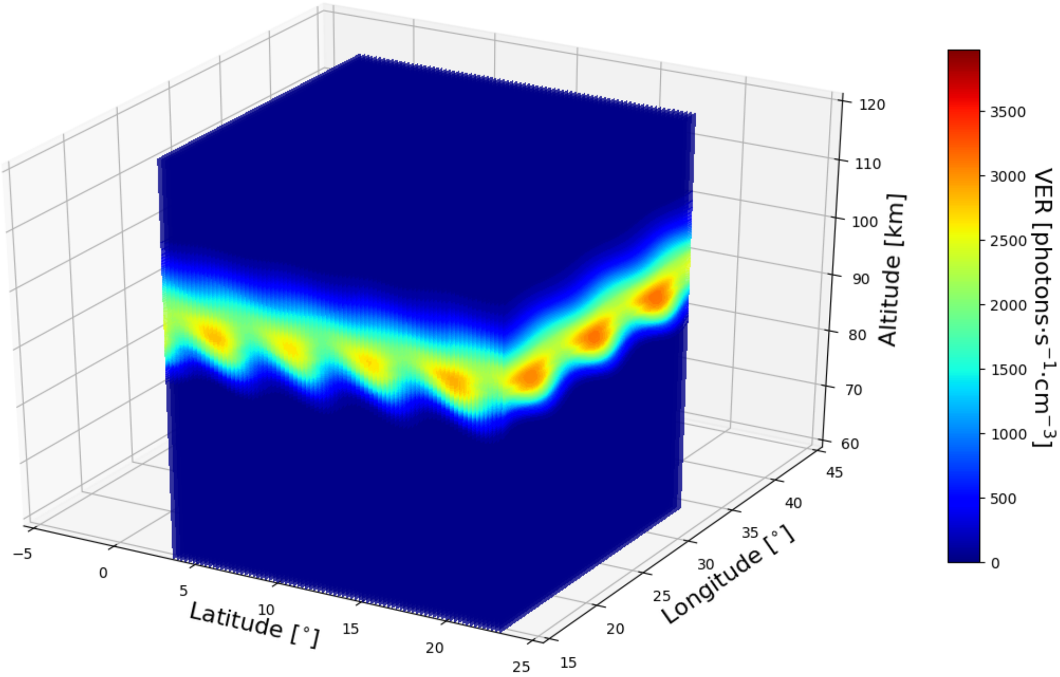

Figure 2.9: Simulated 3-D nightglow emissions perturbed by a wave with a vertical wavelength of 25 km and a horizontal wavelength of 407 km (equivalent to a horizontal wavelength of 500 km and 700 km in the north-south and east-west direction, respectively).

Because the mixing ratio of atomic oxygen is not constant with altitude, the perturbed volume mixing ratio ν' is calculated as follows (*Ward*, 1999):

$$\nu'_O(x,z) = \nu_O(x,z,\delta_z) \approx \nu_O(x,z+\delta_z) \tag{2.26}$$

To illustrate the effect of a GW on the vertical structure of the nightglow emission, a wave with a vertical and horizontal wavelength of 25 km and 407 km, respectively, and an amplitude of 10 K is simulated. The effect on the vertical structure (for different phases of the wave) is illustrated in Fig. 2.8 and the horizontal perturbation of the nightglow is shown in Fig. 2.9.

In Fig. 2.8, vertical profiles showing GW induced airglow perturbations are simulated using the equations above. The unperturbed background atmospheric temperature, atmospheric number density and number densities of various constituents are taken from the HAMMONIA model for midnight condition. As shown in Fig. 2.8, the unperturbed O_2 A-band nightglow altitude profile peaks at around 93 km with an intensity of about

4000 photons $\cdot$ s^{-1} $\cdot$ cm^{-3}. The full-width at half-maximum (FWHM) of the emission layer is about 10 km. The simulated GW has a vertical wavelength of 25 km and an amplitude of 10 K. Nightglow emissions perturbed by this simulated wave with 30 different phases (each 15° apart) are included in the figure. Fig. 2.9 shows the effect of the wave perturbation in the horizontal direction. The horizontal wavelength of the wave projected along the north-south and east-west direction is 500 km and 700 km, respectively.

2.2 Radiative transfer

A radiative transfer model describes how much spectral radiance is measured by an instrument for a given atmospheric state. In this study, a radiative transfer model that integrates the photons emitted by A-band airglow along the ray path and takes into account the atmospheric attenuation is needed and therefore introduced in this section.

Given O_2 A-band emissions in rotational structure η_{rot} and O_2 number density n, the spectral irradiance $I(\tilde{\nu})$ observed by the instrument can be calculated as a path integral along the LOS, in photons $\cdot$ s^{-1} $\cdot$ cm^{-2},

$$I(\tilde{\nu}) = \int_{-\infty}^{\infty} \eta(s)_{\mathrm{rot}}\, \phi(\tilde{\nu},s)\, \exp[-\int_{-s}^{\infty} n(s')\, \sigma(s')\, \phi(\tilde{\nu},s)\, ds']\, ds \tag{2.27}$$

where σ is the absorption cross section. s represents the propagation path through the atmosphere to the instrument along the LOS. The line broadening at wavenumber $\tilde{\nu}$ is characterized by the function $\phi(\tilde{\nu})$.

This propagation path s consists of a set of points at the crossings of the LOS with specified atmospheric grids, along with the distance between neighboring points. As the satellite instrument is above the atmosphere, this geometrical calculation starts at the point where the ray enters the top of the atmosphere, and ends where it leaves the top of the atmosphere. This path is then tracked backwards for the calculation of radiation absorption as shown in Eq. 2.27. A detailed raytracing calculation will be introduced in the next part.

Since O_2 A-band emission is self-absorbed though the atmosphere, a Voigt function (*Stamnes et al.*, 2017) is used to characterize the line shape broadening of O_2 molecule. It convolves the effects of the Lorentz line shape and the Doppler line shape broadening. The Lorentz (pressure-broadened) line shape is predominating in the lower atmosphere, and defined as

$$\phi_L(\tilde{\nu}) = \frac{1}{\pi} \frac{\gamma_{\mathrm{air}}}{(\tilde{\nu}-\tilde{\nu}_0)^2 + \gamma_{\mathrm{air}}^2} \tag{2.28}$$

where $\tilde{\nu}_0$ is the central wavenumber. γ_{air} is the Lorentz half width, which can be calculated based on a reference half width γ_0 at standard temperature T_0 and pressure P_0,

$$\gamma_{\text{air}} = \gamma_0 (\frac{p}{p_0})(\frac{T_0}{T})^{n_{\text{air}}} \tag{2.29}$$

where the reference Lorentz half width γ_0 (at $p = 1$ atm and $T = 296$ K) and temperature exponent n_{air} can be obtained from the HITRAN database.

Unlike pressure induced Lorentz broadening, the Doppler broadening is induced by the thermal motion of the molecules. Doppler broadening is more significant in the thinner upper atmosphere, and can be characterized by a Gaussian function. The Doppler lineshape function, at wavenumber $\tilde{\nu}$ with a central wavenumber $\tilde{\nu}_0$ is defined as

$$\phi_D(\tilde{\nu}) = \frac{1}{\alpha_D\sqrt{\pi}}\exp\left[-\frac{(\tilde{\nu}-\tilde{\nu}_0)^2}{\alpha_D^2}\right] \tag{2.30}$$

where $\alpha_D\sqrt{\ln 2}$ equals to the Doppler half width γ_{self}, with α_D defined as

$$\alpha_D = \tilde{\nu}_0\sqrt{\frac{2k_BT}{mc^2}} \tag{2.31}$$

where c is the speed of light, k is Boltzmann's constant, m is the weight of molecular oxygen, and T is the atmospheric temperature.

Figure 2.10 compares the half width of Lorentz broadening and Doppler broadening for the wavenumber 13093.65 cm^{-1} at altitudes between 60 km and 120 km. Above 60 km, the Doppler broadening is at least a thousand times larger than Lorentz broadening. Therefore, the Voigt function can be replaced by a Doppler function for the calculation of the O_2 A-band absorption in the middle atmosphere.

The simulation of line broadening is followed by a line-by-line calculation that integrates the line intensity in the spectral range. This line-by-line calculation has to be implemented by the sampling on a fine spectral grid. As a consequence, the computational cost increases largely for an accurate estimation of the absorption through the atmosphere. In order to reduce the computational cost, an adaptive sampling grid is used for this line-by-line calculation. More specifically, a denser spectral step is sampled near the center of the emission line while a coarser one is used in the wings of the line. Fig. 2.11 shows an example of how this adaptive sampling grid is used in the line-by-line calculation. Since the half-width of O_2 self broadening ($\sim$0.015 cm^{-1}) is much smaller than the minimum distance between two neighboring emission lines ($\sim$2 cm^{-1}), multiple emission lines will not be overlapped in the wings. Therefore, a single emission line at 13091.71 cm^{-1} is used as an example in Fig. 2.11 without taking into account other emission lines. As shown in this figure, the spectral step within the

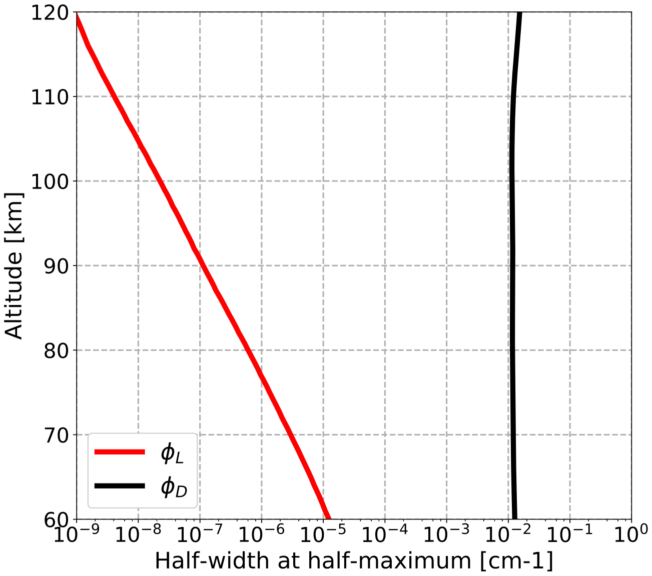

Figure 2.10: Half-width at half-maximum for O_2 Doppler broadening ϕ_D (black line) and Lorentz broadening ϕ_L (red line) at altitudes between 60 and 120 km.

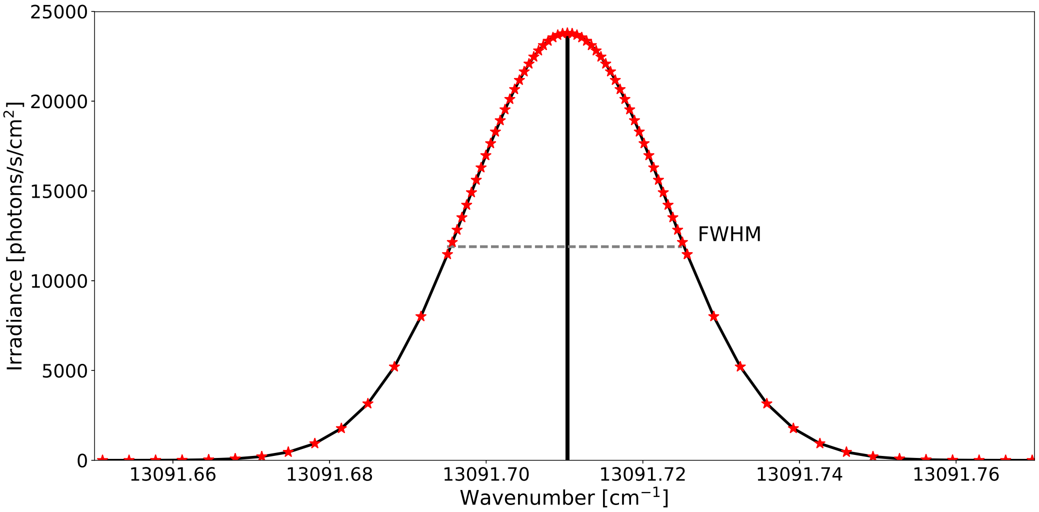

Figure 2.11: Example of using an adaptive sampling grid for the line-by-line absorption calculation. The emission is one of the strong lines within the O_2 A-band, located at 13091.71 cm^{-1}. The red stars represent the sampling positions. The dashed-gray line is the full-width at half-maximum (FWHM) of this emission line. Note that no other emission lines overlap with this plotted emission line in the specified spectral range.

half width is 5 times denser than that in the wings. Sampling on this adaptive grid for a line-by-line calculation is much more efficient than using a fixed spectral step, while the calculated absorptions from the two methods show no significant difference.

Based on this line-by-line calculation, the transmission of O_2 A-band dayglow through the atmosphere can be estimated within the required spectral range (13084-13101 cm^{-1}). Fig. 2.12 shows the total transmission for typical limb sounding measurements with tangent altitudes ranging from 60 to 110 km with an interval of 1 km. It can be seen that very little emission (< 30%) is transmitted to the instrument for an observed tangent altitude of 60 km, and 50% is transmitted at an observed tangent altitude of 73 km. At tangent altitudes above 87 km, the transmission of A-band emission is larger than 90%. Fig. 2.13 shows the transmission of O_2 A-band emission at different tangent altitudes for individual emission lines. It can be seen that the calculated transmission at the tangent altitude is generally lower than the total transmission. This is because the total transmission is also contributed by the atmosphere above the tangent layer. At higher altitudes, the total transmission and the transmission at tangent altitudes show no significant difference. Therefore, in this study the atmosphere is assumed to be optically thin for A-band emissions at altitudes above 87 km.

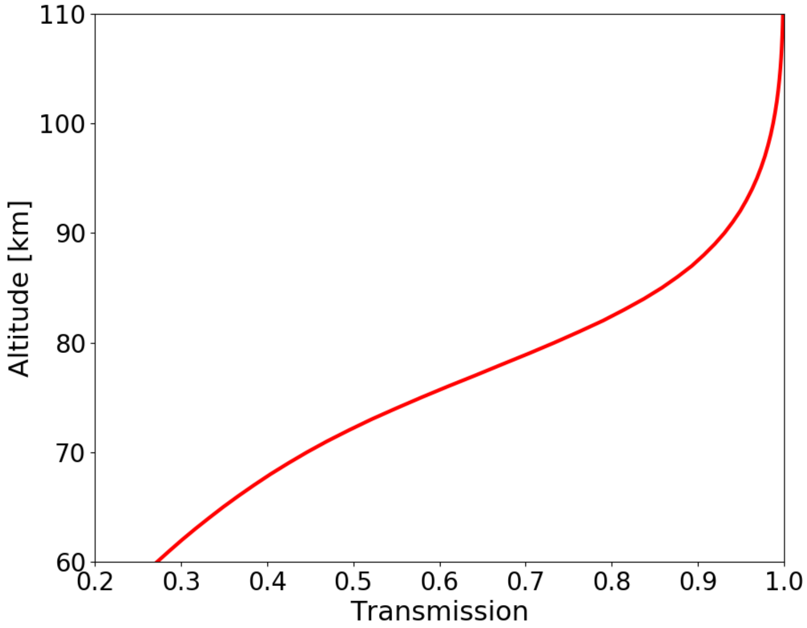

Figure 2.12: Total transmission of A-band dayglow for typical limb sounding measurements with tangent altitudes ranging from 60 to 110 km with an interval of 1 km. The spectral range for this calculation is between 13084 and 13101 cm^{-1}.

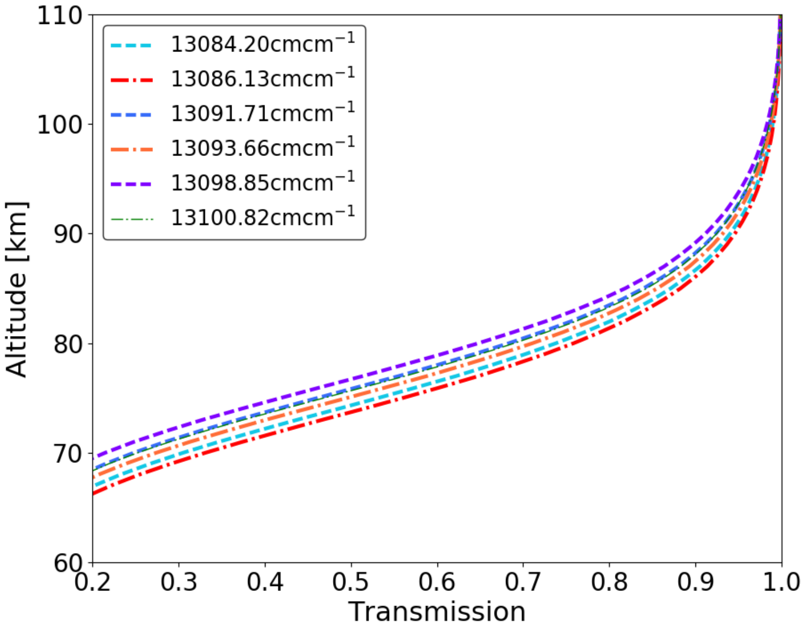

Figure 2.13: Transmission of A-band dayglow at different tangent altitudes for typical limb sounding measurements. The transmissions are calculated for the six emission lines individually.

Theoretical spectra can be obtained after applying the radiative transfer equation. To simulate the actual spectra, the effect of instrumental broadening has to be taken into account. For the instrument considered in this work, the instrumental line shape (ILS) is assumed to be:

$$B(x) = \frac{2}{\gamma}\sqrt{(\frac{\ln 2}{\pi})}\exp\left(-\ln 2\left(\frac{2x}{\gamma}\right)^2\right) \tag{2.32}$$

where γ is instrumental resolution.

2.3 Ray tracing of line-of-sight (LOS)

Integrating the line intensity along the LOS (Eq. 2.27) requires information about the path length through each segment of the atmosphere, which is affected by both the dimension and sampling of the atmospheric grid. According to the requirement in the temperature retrieval, the atmosphere can be sampled in 1-, 2-, and 3-D, respectively.

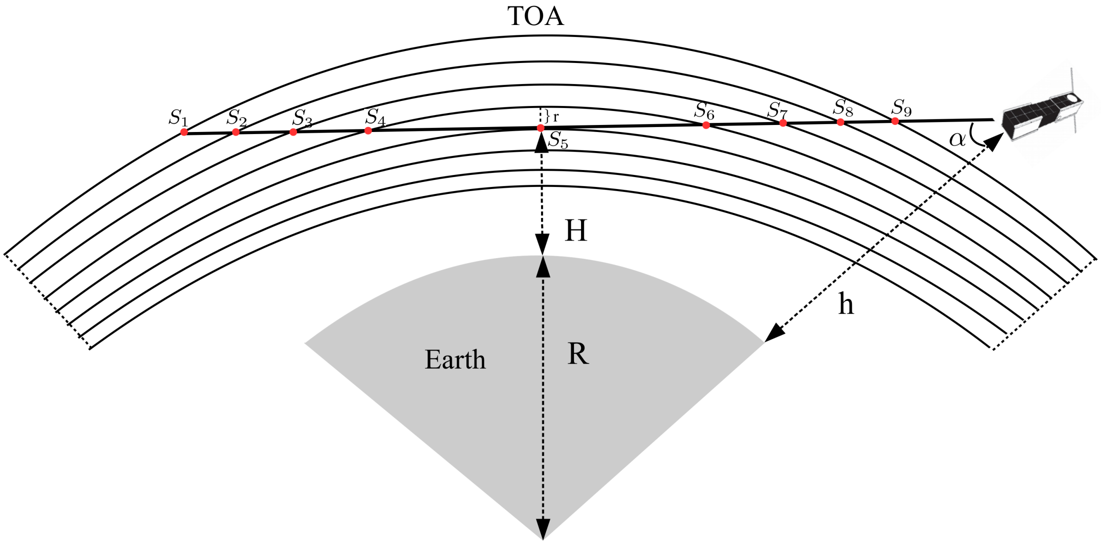

Figure 2.14: Schematic of the LOS ray tracing in a 1-D atmosphere. The satellite instrument is above the top of the atmosphere (TOA). The LOS intersects the atmospheric shells at the red points, from S_1 to S_9. The vertical spacing of the shells is r. H, h, R represent the tangent altitude, orbit height of the satellite and Earth's radius, respectively. α is the viewing angle of the satellite that is looking at the tangent point S_5.

Figure 2.14 illustrates the ray tracing geometry in an 1-D atmosphere for a typical limb sounding measurement. In the 1-D simulation, the atmosphere is assumed to be vertically stratified but horizontally homogeneous. As shown in the figure, the atmosphere is divided into a series of shells, and the atmospheric temperature and various constituents in each shell are assumed to be homogeneous. Since the satellite instrument is above the atmosphere, this geometrical calculation starts at the point where the ray enters the top of the atmosphere (TOA), and ends where it leaves the TOA. The LOS intersects the grid shells at the red circles from S_1 to S_9. The vertical spacing of the shells (r) is defined as the vertical sampling of this 1-D atmosphere. In addition, this Fig. 2.14 illustrates the relation between the tangent altitude and the satellite viewing angle. Assuming a tangent altitude of H, Earth's radius of R and satellite altitude of h, the satellite viewing angle in this case can be calculated as

$$\alpha = \arcsin(\frac{R+H}{R+h}) \tag{2.33}$$

Similar with the ray tracing in an 1-D atmosphere, a ray tracing in a 2-D atmosphere can be done as shown in Fig. 2.15. Since horizontal inhomogeneity of the atmosphere is considered in this ray tracing, more intersection points between the instrument's LOS and the atmospheric grid are captured. Between two neighboring points (S_1 and S_2), the temperature and number densities of various constituents are approximated as the linearly interpolated values in the center (the blue circle) of this grid. In a similar way, this ray tracing approach can be extended to a 3-D atmosphere. However, the computational cost also increases exponentially with the dimension of the atmosphere.

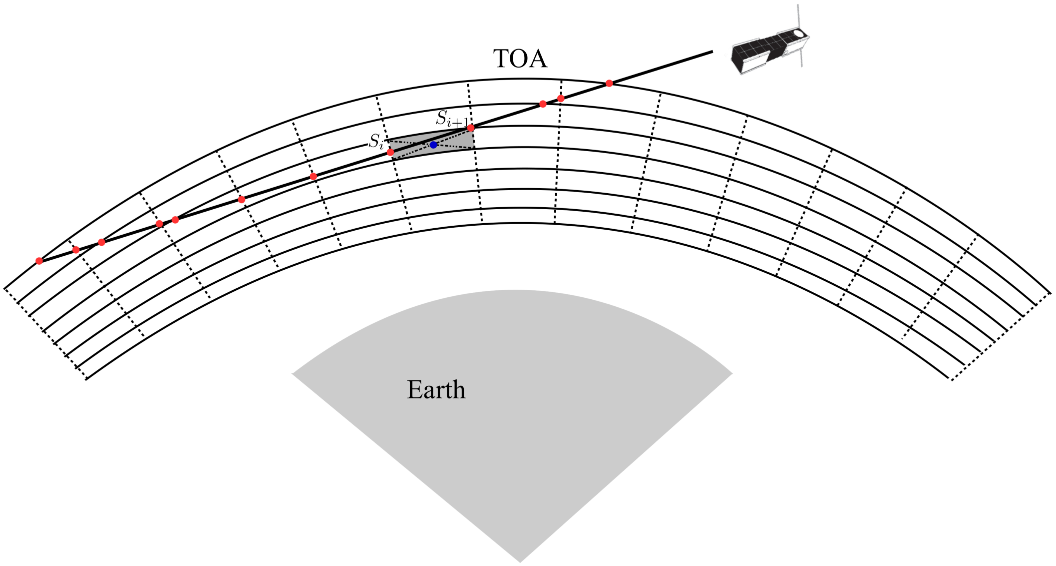

Figure 2.15: Schematic of LOS ray tracing in a 2-D atmosphere. The symbols and markers are defined the same as in Fig. 2.14. The blue circle is the center point of the shadowed grid cell.

In this study, the Atmospheric Radiative Transfer Simulator (ARTS) (*Buehler et al.*, 2005) is used to trace the instrument's LOS. ARTS is a free open-source software program that simulates atmospheric radiative transfer. It focuses on thermal radiation from the microwave to the infrared spectral range. The second version of ARTS (*Eriksson et al.*, 2011) allows simulations for 1-, 2- or 3-D atmosphere.

2.4 Observational spectra modelling

In this section, the O_2 A-band spectra are simulated based on the calculated airglow emission, rotational structure distribution, LOS ray tracing, radiative transfer, as well as the instrumental function. The background atmosphere is taken from the HAMMONIA model and the viewing geometry is simulated for typical limb sounding measurements.

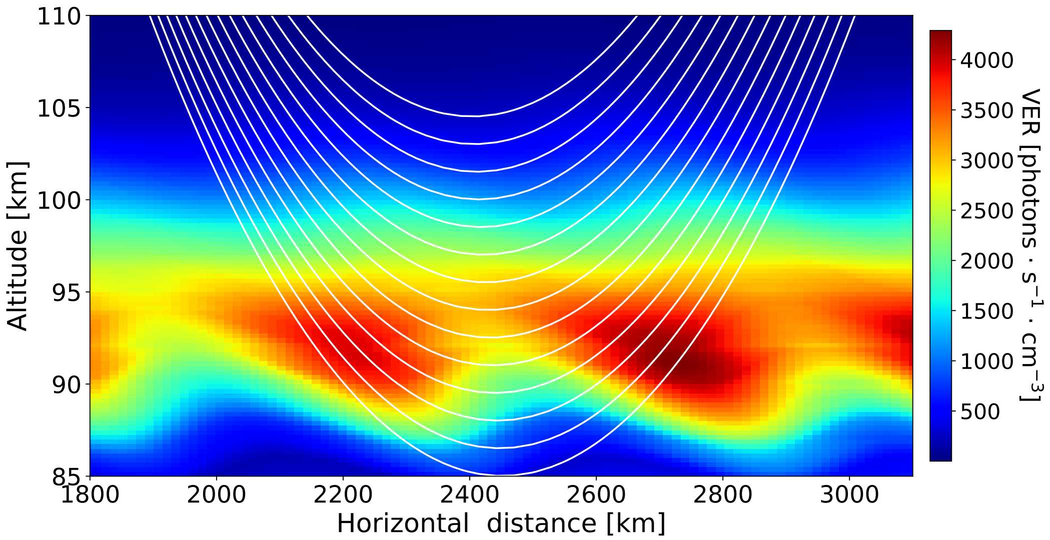

Figure 2.16: Simulated 2-D O_2 A-band nightglow emissions in the altitude range between 85 and 110 km. The background atmosphere is taken from the HAMMONIA model, run at 30° N and 30° E for 2:00 local solar time. The nightglow emission is perturbed by a wave with a vertical wavelength of 20 km and a horizontal wavelength of 500 km, and an amplitude of 10 K. The LOSs of different limb sounding measurements are plotted in white curves.

Figure 2.16 shows the simulated 2-D O_2 A-band nightglow emissions at altitudes between 85 and 110 km. The background atmosphere is perturbed by a GW with a vertical wavelength of 20 km and a horizontal wavelength of 500 km. The GW induced temperature perturbation has an amplitude of 10 K in this altitude range.

A series of limb sounding measurements at tangent altitudes from 86 to 105.5 km with an interval of 1.5 km are traced in this region. The modelled spectra for these limb sounding measurements are shown in Fig. 2.17. The considered spectral range (13082-13103 cm $^{-1}$) covers the six emission lines mentioned before.

2.5 Retrieval algorithm

In this section, the inverse problem in terms of retrieving atmospheric temperature from satellite-borne measurements is presented. A retrieval scheme based on optimal estimation theory was presented by *Rodgers* (2000) to solve a 1-D inverse problem, and is applied in this work to higher dimensions.

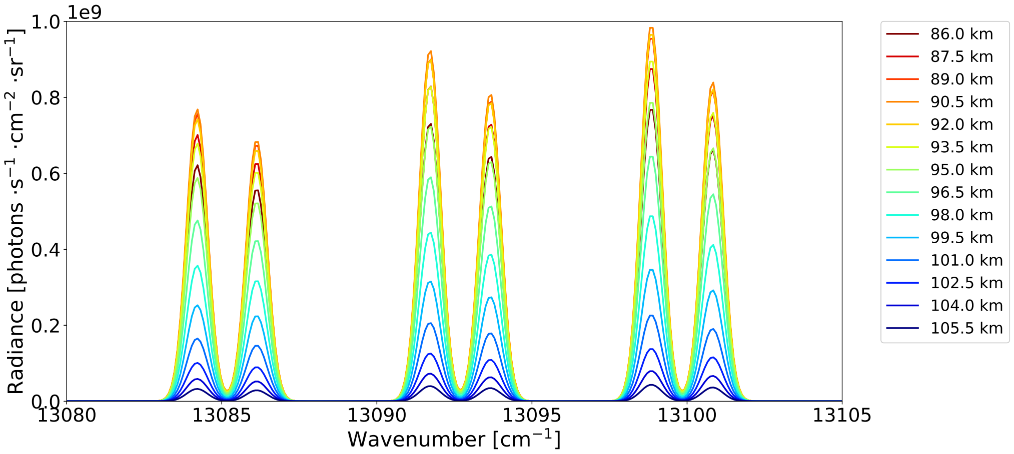

Figure 2.17: Modelled spectra for limb sounding measurements at different altitudes.

2.5.1 Inverse problem

In the setup of the inverse problem, the forward model described in Sect. 2.1 - Sect. 2.3 is abstracted as function $\boldsymbol{f}$ and the atmospheric state (containing constituent number densities, temperature, etc.) as variable $\boldsymbol{x}$. The observational spectra are given by the vector $\boldsymbol{y}$, which can be described as the sum of the forward model applied to an atmospheric state and the measurement errors $\boldsymbol{\varepsilon}$,

$$\boldsymbol{y} = \boldsymbol{f}(\boldsymbol{x}) + \boldsymbol{\varepsilon} \tag{2.34}$$

Finding the atmospheric state $\boldsymbol{x}$ from the known measurements $\boldsymbol{y}$ is called the inverse problem. Ideally, the solution of this inverse problem can be found analytically by solving the equation,

$$\boldsymbol{x} = \boldsymbol{f}^{-1}(\boldsymbol{y}') \tag{2.35}$$

where $\boldsymbol{y}'$ denotes the observational vector contaminated by measurement errors, which can not be excluded from the measurements in practice. Solving Eq. 2.34 requires the inverse problem to be well-posed (*Hadamard*, 1902), for which the following conditions should be met,

1. A solution of this inverse problem must exist.
2. This solution must be unique.
3. Small changes in the input data should not cause large changes in the solution.

However, these conditions can hardly be met in the retrieval of high-spatial-resolution atmospheric state from satellite-borne measurements. Because the number of measurements are often limited compared with the unknowns of the atmospheric state, multiple solutions are possible. This ill-posed problem can sometimes result in unphysical and therefore meaningless results. However, the inverse problem of Eq. 2.34 can be transformed into a minimization problem instead of requiring an exact solution,

$$\min_{x} ||\boldsymbol{f}(\boldsymbol{x}) - \boldsymbol{y}||^2 \tag{2.36}$$

This minimization problem ensures at least one solution can be obtained for an ill-posed problem of Eq. 2.34. The true atmospheric state $\boldsymbol{x}$ is one of the multiple solutions, while some physically meaningless solutions may also exist. Therefore, extra efforts should be made to ensure the uniqueness of the solution. To constrain the solution, the minimization problem of Eq. 2.36 is modified by adding an additional term at the end (*Tikhonov and Arsenin*, 1977; *Rodgers*, 2000),

$$\boldsymbol{J}(\boldsymbol{x}) = (\boldsymbol{f}(\boldsymbol{x}) - \boldsymbol{y})^T \mathbf{S}_\varepsilon^{-1} (\boldsymbol{f}(\boldsymbol{x}) - \boldsymbol{y}) + (\boldsymbol{x} - \boldsymbol{x_a})^T \mathbf{S}_a^{-1} (\boldsymbol{x} - \boldsymbol{x_a}) \tag{2.37}$$

where matrix $\mathbf{S}_a^{-1}$ is the inverse covariance in optimal estimation inversion theory or any other regularization matrix, $\mathbf{S}_\varepsilon$ is the covariance matrix of the measurement error, and $\boldsymbol{x_a}$ represents the a priori data. The first term in Eq. 2.37 calculates the difference between the computed and real observations, while the second terms calculates the difference between the estimated and a priori atmospheric state. The a priori data is often taken as the climatological mean of the retrieved quantities. The usage and setup of the regularization matrix $\mathbf{S}_a^{-1}$ will be discussed in the next section. The minimization of the cost function $\boldsymbol{J}$ in Eq. 2.37 ensures the derived solution is physically meaningful. A Gaussian-Newton iteration scheme is usually used to to solve this nonlinear minimization problem,

$$\begin{aligned} \boldsymbol{x}_{i+1} = \boldsymbol{x}_i + \Big(\boldsymbol{f}'(\boldsymbol{x}_i)^T \mathbf{S}_\varepsilon^{-1} \boldsymbol{f}'(\boldsymbol{x}_i) + \mathbf{S}_a^{-1} \Big)^{-1} \\ \cdot \Big(\boldsymbol{f}'(\boldsymbol{x}_i)^T \mathbf{S}_\varepsilon^{-1} (\boldsymbol{y} - \boldsymbol{f}(\boldsymbol{x}_i)) + \mathbf{S}_a^{-1} (\boldsymbol{x}_a - \boldsymbol{x}_i) \Big) \end{aligned} \tag{2.38}$$

where $\boldsymbol{f}'(\boldsymbol{x}_i)$ is the Jacobian matrix of the forward model $\boldsymbol{f}$ at atmospheric state $\boldsymbol{x}_i$. It contains the partial derivative of all simulated measurements $\boldsymbol{y}$ with respect to all unknown parameters in vector $\boldsymbol{x}$. However, the convergence of the Gauss-Newton iteration scheme is not guaranteed since it sometimes only converges to a local optimum.

If the forward model $\boldsymbol{f}$ is significantly nonlinear, following the iteration scheme of Eq. 2.38 can result in an increase rather than a decrease of the cost function $\boldsymbol{J}$. The Levenberg-Marquardt (*Levenberg*, 1944; *Marquardt*, 1963; *Ceccherini and Ridolfi*, 2010) algorithm is modified based on the Gauss-Newton iteration and can be efficiently used to solve the minimization problem even if the forward model is significantly non-linear. The iterative solution of the Levenberg-Marquardt iteration is,

$$\begin{aligned} \boldsymbol{x}_{i+1} = \boldsymbol{x}_i + \Big(\boldsymbol{f}'(\boldsymbol{x}_i)^T \mathbf{S}_\varepsilon^{-1} \boldsymbol{f}'(\boldsymbol{x}_i) + \mathbf{S}_a^{-1} + \lambda_i \mathbf{I}\Big)^{-1} \\ \cdot \Big(\boldsymbol{f}'(\boldsymbol{x}_i)^T \mathbf{S}_\varepsilon^{-1} \big(\boldsymbol{y} - \boldsymbol{f}(\boldsymbol{x}_i)\big) + \mathbf{S}_a^{-1}(\boldsymbol{x}_a - \boldsymbol{x}_i)\Big) \end{aligned} \tag{2.39}$$

where the added term consists of an identity matrix $\mathbf{I}$ multiplied by a scalar parameter λ_i. By damping the step width $(\boldsymbol{x}_{i+1} - \boldsymbol{x}_i)$, the term $\lambda_i \mathbf{I}$ bends the searching direction towards the direction with steepest descent of the cost function $\boldsymbol{J}$. In practice, the iteration of Eq. 2.39 starts with an initial estimation of the scalar parameter λ_0. At each iteration, if the corrected $\boldsymbol{x}_i$ could reduce the value of the cost function (i.e. $\boldsymbol{J}_{i+1} < \boldsymbol{J}_i$), then the new state $\boldsymbol{x}_i$ is accepted and the scalar parameter needs to be reduced for the next iteration. If the cost function is not reduced, a larger value of the scalar parameter is chosen to repeat the iteration at step i.

2.5.2 Regularization

The regularization matrix $\mathbf{S}_a^{-1}$ constrains the solutions of the minimization problem to lie in a physically meaningful range. Tikhonov regularization is a common method to regularize ill-posed inverse problems (*Phillips*, 1962; *Twomey*, 1963; *Tikhonov and Arsenin*, 1977). In this study, a combination of two operators, zeroth and first order Tikhonov regularization matrix, is used to assemble $\mathbf{S}_a^{-1}$.

The zeroth order Tikhonov regularization $\mathbf{L}_0$ is a simple identity matrix $\mathbf{I}$. It minimizes the difference between $\boldsymbol{x}$ and $\boldsymbol{x}_a$ such that the solution is constrained towards the absolute value of $\boldsymbol{x}_a$. The first order Tikhonov regularization matrix $\mathbf{L}_1$ gives a constraint on the first derivative. It constrains the derivative of the solution to the derivative of the a priori profile, which is a smooth profile in most cases. For 1-D atmospheric inverse problems that aim to retrieve a series of vertical profiles, $\mathbf{L}_1$ maps $\boldsymbol{x}$ onto its first order derivative with respect to altitude,

$$\mathbf{L}_1(i,j) = \begin{cases} 1 & \text{if } j = i+1 \\ -1 & \text{if } j = i \\ 0 & \text{otherwise} \end{cases} \tag{2.40}$$

where $\mathbf{L}_1$ is a $(m-1) \times m$ matrix with m to be the number of elements in $\boldsymbol{x}$. Then, the combined Tikhonov regularization can be written as the sum of the two operators,

$$\mathbf{S}_a^{-1} = \alpha_0 \mathbf{I} + \alpha_1 \mathbf{L}_1{}^T \mathbf{L}_1 \tag{2.41}$$

where α_0 and α_1 are weighting parameters used to balance the contributions of the zeroth and first order regularization terms. The overall strength of the regularization matrix $\mathbf{S}_a^{-1}$ is controlled by the weighting parameters. If the weighting parameters are too small, the cost function $\boldsymbol{J}$ in Eq. 2.37 will be dominated by the measurement term. In this case, the regularization term has very few effects in constraining the results towards physically meaningful ones. If the weighting factors are set too large, the results will be highly regularized by the a priori information. Therefore, moderate values of weighting factors should be selected in practical applications.

Modifications should be made on Eq. 2.41 if $\mathbf{S}_a^{-1}$ is employed to regularize 3-D inverse problems. Assuming a $m \times n \times l$ matrix $\mathbf{X}$ that represents a 3-D atmospheric state in a corresponding ZXY's Cartesian Coordinate. The 3-D matrix should be first converted into an 1-D vector $\boldsymbol{x}$. One may encounter that the neighboring elements in matrix $\mathbf{X}$ are dispersed away from each other in the vector $\boldsymbol{x}$. Therefore, special focus should be given to the construction of the 3-D first order regularization matrix, ensuring the elements in $\mathbf{X}$ are not oscillating along each axis. Here in this study, the elements in $\mathbf{X}$ are transferred into $\boldsymbol{x}$ in a order with the first index (in Z axis) changing fastest and the last index (in Y axis) changing slowest. Since the Z axis is searched first, the vertical structure of $\mathbf{X}$ can still be retained even after being reshaped into $\boldsymbol{x}$. Therefore, the first order regularization matrix in the Z direction $\mathbf{L}_1^z$ can be set the same as in Eq. 2.40. $\mathbf{L}_1^x$ and $\mathbf{L}_1^y$ are set in a different way,

$$\mathbf{L}_1^x(i,j) = \begin{cases} 1 & \text{if } j = i+n \\ -1 & \text{if } j = i \\ 0 & \text{otherwise} \end{cases}, \qquad \mathbf{L}_1^y(i,j) = \begin{cases} 1 & \text{if } j = i+(m\times n) \\ -1 & \text{if } j = i \\ 0 & \text{otherwise} \end{cases} \tag{2.42}$$

where $\mathbf{L}_1^z$, $\mathbf{L}_1^x$ and $\mathbf{L}_1^y$ are all $(k-1)\times k$ matrices with k to be the total number of elements ($k = m \times n \times l$) in $\mathbf{X}$. After adding the first order regularization term in the x and y directions, the total regularization matrix can be reassembled for 3-D inverse problems,

$$\mathbf{S}_a^{-1} = \alpha_0\mathbf{I} + \alpha_1^z\mathbf{L}_1^{zT}\mathbf{L}_1^z + \alpha_1^x\mathbf{L}_1^{xT}\mathbf{L}_1^x + \alpha_1^y\mathbf{L}_1^{yT}\mathbf{L}_1^y \tag{2.43}$$

where α_0, α_1^z, α_1^x and α_1^y are the weighting factors for corresponding regularization terms.

2.5.3 Diagnostics

Due to the regularization, the retrieved result $\hat{\boldsymbol{x}}$ is smoothed over the true atmospheric state $\boldsymbol{x}_r$. In order to study the spatial resolution and sensitivities of $\hat{\boldsymbol{x}}$, the effect of smoothing on the retrieval results should be characterized. Following *Rodgers* (2000), a so-called averaging kernel matrix is defined,

$$\mathbf{A} = \frac{d\hat{\boldsymbol{x}}}{d\boldsymbol{x}_r} \tag{2.44}$$

The averaging kernel matrix **A** describes the sensitivity of the retrieval result $\hat{\boldsymbol{x}}$ to the true atmospheric state $\boldsymbol{x}_r$, and can be written as explicit algebraic expressions in the form,

$$\mathbf{A} = \mathbf{G}\boldsymbol{f}'(\hat{\boldsymbol{x}}) \tag{2.45}$$

with **G** being the gain matrix,

$$\mathbf{G} = \left(\mathbf{S}_a^{-1} + \boldsymbol{f}'(\hat{\boldsymbol{x}})^T \mathbf{S}_\varepsilon^{-1} \boldsymbol{f}'(\hat{\boldsymbol{x}})\right)^{-1} \boldsymbol{f}'(\hat{\boldsymbol{x}})^T \mathbf{S}_\varepsilon^{-1} \tag{2.46}$$

where the averaging kernel **A** is a $k \times k$ matrix with k being the number of elements in $\hat{\boldsymbol{x}}$. The measurement contribution and smoothing effect on each retrieved element can be obtained by analyzing the corresponding row of **A**.

The measurement contribution for the ith element in $\hat{\boldsymbol{x}}$ is calculated by summing over the ith row of the matrix **A**. If the measurement contribution has a value close to 1, that means the solution for this point is mostly determined by real measurements. If this value is as small as 0, that means the solution is highly regularized and a priori data plays a major role in determining its value. For an ideal observation strategy, the measurement contribution should be 1 for all the retrieved points. But in practice, there is a greater measurement contribution to some retrieved points than others. The lower measurement contribution often occurs near the boundaries of the retrieval region, where the number of actual available measurements is limited or the signal-to-noise ratio (SNR) is low.

Spatial resolution is a measure of the dispersion of the signal, usually calculated via the rows of matrix **A**. Here we use a 3-D inverse problem to illustrate how the spatial resolution is calculated, and the same method can be applied to 1-D and 2-D inverse problems. Before the spatial resolution is calculated, the given row of the averaging kernel matrix **A** should be reshaped back to a 3-D matrix first. This process should follow the same index changing order that is used before, ensuring all the elements are stored in the right positions in the matrix. Then, the spatial resolution of a data point is estimated by calculating its FWHM in the three directions (Z, X and Y). In each direction, a linear interpolation is used to identify the half maximum points in both sides. The spatial resolution in this direction is the distance between the two interpolated points.

The gain matrix **G** and the averaging kernel matrix **A** can be viewed as operators to produce the retrieval results by a linear combination of the form,

$$\hat{\boldsymbol{x}} = \mathbf{A}\boldsymbol{x}_r + (\mathbf{I}-\mathbf{A})\boldsymbol{x}_a + \mathbf{G}\boldsymbol{\varepsilon} \tag{2.47}$$

where $\mathbf{G}\boldsymbol{\varepsilon}$ represents the errors on the retrieved quantities caused by measurement errors. The first term $\mathbf{A}\boldsymbol{x}_r$ in Eq. 2.47 is determined by the measurements and it reveals how the averaging kernel constrains the atmospheric state. The second term $(\mathbf{I}-\mathbf{A})\boldsymbol{x}_a$ introduces the contribution of regularization errors to the retrieval. If $\mathbf{A}$ is an identity matrix, the second term is omitted from Eq. 2.47 and the retrieval results will be unbiased.

For 3-D inversion problems with a large number of unknowns, the calculation of averaging kernel matrix is very computationally expensive since full matrix inversion is involved in Eq. 2.45. In this case, much more computational time will be spent in calculating the averaging kernel matrix than solving the inversion problem itself. However, in practice it is not necessary to calculate the full averaging kernel matrix. The diagnostics for a single point can be derived by extracting the corresponding row of the averaging kernel matrix. Following Eq. 2.45 and Eq. 2.46, only a row of

$$\mathbf{D}^{-1} = \left(\mathbf{S}_a^{-1} + \boldsymbol{f}'(\hat{\boldsymbol{x}})^T \mathbf{S}_\varepsilon^{-1} \boldsymbol{f}'(\hat{\boldsymbol{x}})\right)^{-1} \tag{2.48}$$

is used to derive the same row of $\mathbf{A}$. Since $\mathbf{D}^{-1}$ is a symmetrical matrix, a row of $\mathbf{D}^{-1}$ equals to the corresponding column of $\mathbf{D}^{-1}$. A single column of $\mathbf{D}^{-1}$ can be easily derived by using iterative algorithms for solving a liner equation (e.g. conjugate gradient method). This linear equation is built as

$$\mathbf{D}_n \boldsymbol{l} = \mathbf{v} \tag{2.49}$$

where $\mathbf{v}$ is a unit vector with the nth element to be 1. The solution of this linear equation $\boldsymbol{l}$ represents the nth column of $\mathbf{D}^{-1}$. Then the calculation of the averaging kernel matrix is simplified as

$$\mathbf{A} = \boldsymbol{l}^T \boldsymbol{f}'(\hat{\boldsymbol{x}})^T \mathbf{S}_\varepsilon^{-1} \boldsymbol{f}'(\hat{\boldsymbol{x}}) \tag{2.50}$$

This can be easily calculated via three vector-matrix multiplications from the left to the right. For 3-D tomographic retrieval problems, several points at different locations can be selected to check the diagnostics of the retrieval results using this method.

2.6 Chapter summary

This chapter presented the forward modelling of satellite-borne O_2 A-band airglow observations. It includes the simulation of O_2 A-band airglow emissions, the GW induced perturbation in emission intensities, the instrument's LOS ray tracing, and the radiative transfer. A group of spectra were simulated under limb sounding geometries using this forward model. Then, the inverse problem in the field of atmospheric remote sensing was presented accompanied with its mathematical representations. Typical iterative methods for solving this inverse problem and regularization schemes for constraining the solution were discussed. Special focus was given to the application of such retrieval algorithms in large-scale problems (e.g. 3-D tomographic reconstruction). In the end, it was shown how diagnostic information can be derived for 3-D tomographic retrievals.

Chapter 3

‘Target mode’ 2-D tomographic reconstruction of small-scale GWs

In this chapter, the temperature retrieval scheme described in Sect. 2 is applied to an envisaged satellite mission measuring the O_2 A-band airglow emission in the MLT. A new observation strategy, called ‘target mode’, is proposed for GWs in the mesopause region by combining limb and sub-limb measurements for improving the spatial resolution that conventional limb sounders can achieve. This ‘target mode’ works only for the layered emissions with high optical thickness in the lower atmosphere.

Before introducing the observation geometry and retrieval scheme of this ‘target mode’, the conventional methods for the retrieval of 1-D and 2-D GW parameters from limb sounding measurements are presented. Their ability in resolving small-scale GWs are compared with the ‘target mode’ in numerical simulations. A sensitivity study is conducted to show how this ‘target mode’ outperforms the conventional limb measurements in deriving small-scale GW parameters.

3.1 1-D GW retrieval

For a 1-D atmospheric retrieval, the atmosphere is assumed to be horizontally homogeneous and only vertical variations are considered. The vertical structure of the retrieved quantities is obtained from a series of limb soundings measuring different altitude layers of the atmosphere. In this section, the forward model and retrieval algorithm presented in Chapter 2 are applied to derive the vertical structures of GWs with simulated O_2 A-band nightglow observations.

Fig. 3.1 shows the vertical profile of the simulated atmospheric temperature in a

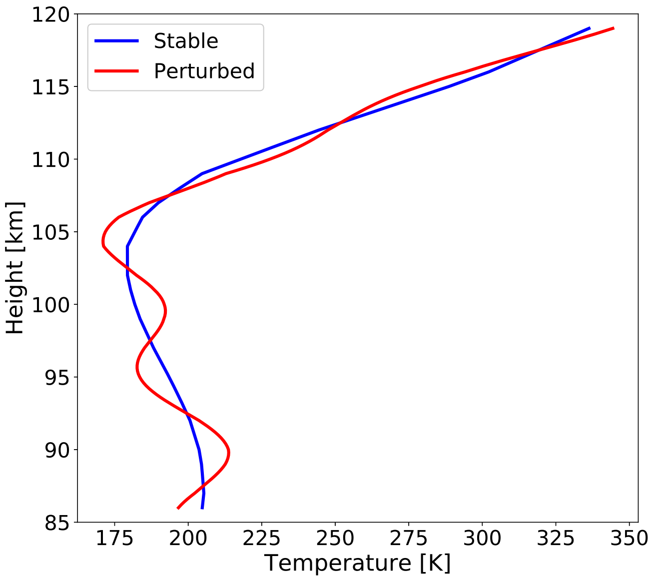

Figure 3.1: Simulated vertical profile of the atmospheric temperature in a stable state (blue curve) and perturbed by a GW (red curve). The background temperature is taken from the HAMMONIA model run at 30° N and 50° E, for 03:30 local solar time (night condition). The simulated GW has a vertical wavelength of 10 km and an amplitude of 10 K.

stable state (blue curve) and perturbed by a vertically propagating GW (red curve). This simulated wave is generated in the lower atmosphere and propagates upwards with a vertical wavelength of 10 km. In the mesopause region, it produces a 10 K oscillation on the background temperature. The perturbation model introduced in Sect. 2.1.5 was used to calculate the induced displacement of the airparcel and the subsequent perturbation on the emission layer.

We assume the satellite is operated in a ~600 km sun-synchronous orbit with an inclination angle of 98°. The instrument will employ a 2-D detector array consisting of about 1000 pixels in the spectral direction and 600 pixels in the spatial direction. It is capable to measure infrared emissions between 13082 and 13103 cm^{-1}, which covers the six emission lines within O_2 A-band for temperature derivation. The limb images cover a vertical field of view from a lower tangent altitude of 60 km to an upper tangent altitude of 120 km, with a vertical resolution of ~100 m for each pixel. To increase the signal-to-noise ratio, individual array pixels can be binned to obtain sampling patterns of specific measurement modes. For instance, the tangent points are sampled with an altitude step of 1.5 km for simulated limb measurements. In this thesis, all the relevant simulations and sensitivity studies for the envisaged satellite mission use the same platform and instrument setup presented here.

In this section, a group of limb sounding measurements were simulated to observe this O_2 A-band nightglow emission. These limb measurements start at the lowest altitude of 86 km and cap at the altitude of 110 km, with an interval of 1.5 km. The transmission of A-band emission through the atmosphere was given in Sect. 2.2 by Fig. 2.12. For altitudes above 87 km, the atmosphere is assumed to be optically thin and the self-absorption term in Eq. 2.27 can be omitted. After applying this radiative transfer under optically thin condition, the modelled spectra similar with Fig. 2.17 can be obtained and therefore are not shown here.

In this simulation, the forward model is run for a highly resolved atmosphere with a vertical spacing of 50 m. The simulated limb measurements are generated at a vertical interval of 1.5 km, with 1% measurement errors added. In the end, the atmospheric temperature is retrieved in a grid with a vertical spacing of 1 km. The aim of this study is to demonstrate how GW parameters can be deduced from the temperature measurements. The retrieval algorithm described in Sect. 2.5 was applied to retrieve the temperature profile from modelled spectra. A combination of zeroth and first order Tikhonov regularization was used to constrain the retrieval results. The zeroth order regularization constrains the solution towards the absolute value of a priori, while the first regularization reduces vertical oscillations caused by the measurement errors. In this case, the a priori information is set the same as the background temperature, i.e. atmospheric temperature without wave perturbations. Fig. 3.2 shows the retrieval results at altitudes between 87 and 110 km for this 1-D simulation. Fig. 3.2 (a) shows the a priori data, ‘real temperature’ (temperature perturbed by the simulated wave) and the retrieved temperature profile. By subtracting the background atmosphere from the retrieved temperature profile, the wave induced temperature perturbation can be obtained as shown in Fig. 3.2 (b). A vertical wavelength of 10 km can be clearly seen in the resolved wave structure, and an amplitude of $\sim$10 K can be roughly captured.

The difference between the ‘real temperature’ and the retrieved temperature profile is shown in Fig. 3.3. The retrieved temperature errors at all altitudes lie within the range of ±2.5 K. The averaging kernel matrix is used to determine the vertical resolution and measurement contribution of the retrieval results as shown in Fig. 3.4. The colored lines are individual rows of the averaging kernel matrix, representing averaging kernels at different altitudes. The corresponding altitude for each row of the averaging kernel is the height at which it peaks. The vertical resolution is derived from the FWHM by linear interpolation. In this experiment, the vertical resolution for the studied altitude range (88-108 km, with lower and upper boundary removed) is $\sim$1 km. The measurement contribution is calculated by summing up each row of the averaging kernel, indicated as solid black line in Fig. 3.4. A typical value greater than $\sim$0.8 can be achieved for this altitude range.

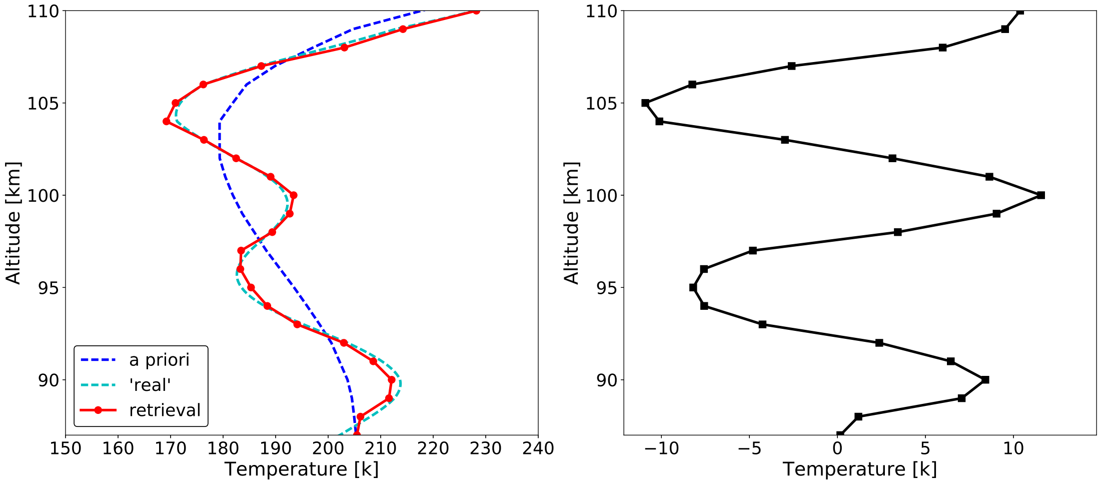

Figure 3.2: 1-D retrieval results for simulted limb sounding observations. Figure (a) shows the a priori data (dashed dark blue curve), the 'real temperature' (dashed light blue curve) and the retrieved temperature profile (solid red curve). The temperature perturbation after subtracting the background temperature (dashed dark blue curve) is plotted as black line in Figure (b). The dots in both figures represent the retrieved data points.

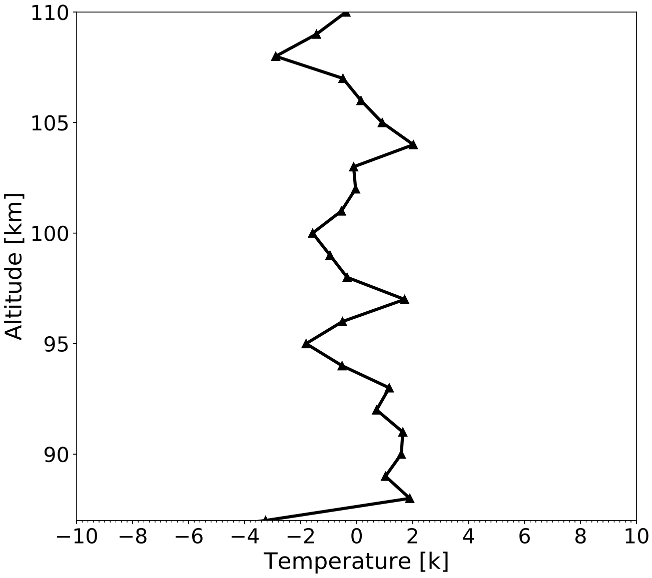

Figure 3.3: The error budget for the 1-D retrieval experiment.

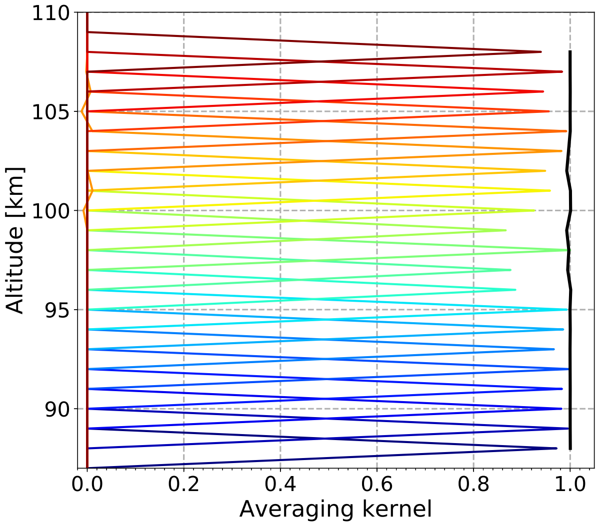

Figure 3.4: Averaging kernels for the retrieval results. Individual rows of the averaging kernel are represented by different colors. The measurement contribution is represented by the black line.

3.2 2-D GW retrieval

In the previous section, the derivation of the vertical structure of a GW from limb sounding measurements is presented. However, the horizontal structure of a wave is difficult to be identified from such a single measurement track. To derive the vertical as well as horizontal structures of a wave, data acquired from consecutive limb scanning sequences are required. *Ern et al.* (2004) proposed to combine the phases provided by the wave analysis of adjacent temperature vertical profiles to estimate the horizontal wavelength of GWs. This approach is based on 1-D retrieval, and was successfully used to retrieve 2-D GWs with CRISTA-2 measurements, as well as several other datasets (*Alexander et al.*, 2008; *Wright et al.*, 2010; *Ern et al.*, 2011). Horizontal structures of a GW can be also obtained from 2-D retrievals. But it has specific requirement on the viewing geometry of the instrument: that the direction of the LOS needs to be along or at least close to the orbital track. In this case, horizontal inhomogeneities of the atmosphere are considered by oversampling along the LOS. This 2-D retrieval has been used in Michelson Interferometer for Passive Atmospheric Sounding (MIPAS) (*Carlotti et al.*, 2001) and Microwave Limb Sounder (MLS) (*Livesey and Read*, 2000). The advantage of 2-D retrievals over 1-D retrievals is that GW structures (e.g. amplitude, phase) are better represented and GWs with smaller horizontal wavelengths can be observed in 2-D retrievals. In this section, the aforementioned methods are applied in the retrieval model to derive 2-D wave structures from temperature measurements in the MLT.

3.2.1 Horizontal wavelength derivation from phase analysis

The basic idea of retrieving horizontal wavelength of a GW from limb measurements is to deduce the phase difference from adjacent profiles. Assuming only one GW exists in the observed area, the wave induced temperature perturbation can be written as

$$T'(x_h,z,t) = \hat{T}(x_h,z,t)\cos\left(\frac{2\pi x_h}{\lambda_{x_h}} + \frac{2\pi z}{\lambda_z} - \hat{\omega} t\right) \tag{3.1}$$

where $\hat{T}$ represents the temperature amplitude, $\hat{\omega}$ is the ground-relative frequency, λ_z is the vertical wavelength and λ_{x_h} is the horizontal wavelength. In this case, the atmospheric variations are considered in a 2-D plane, with the horizontal coordinate being parallel to the orbital track.

At a fixed altitude z, the wave induced temperature perturbations at two adjacent profiles i and j are $T'(x_i,z,t_i)$ and $T'(x_j,z,t_j)$, respectively. The phase difference for the two points can be derived from Eq. 3.1, and written as $\Delta\phi_{i,j}$ here. Therefore, the horizontal wavelength of the wave can be deduced from this phase difference $\Delta\phi_{i,j}$, along with the horizontal distance between the two points $\Delta x_{i,j}$,

$$\lambda_{x_h} = \frac{2\pi}{\Delta\phi_{i,j} + 2n\pi}\Delta x_{i,j}, \quad n = 0,1,2,3... \tag{3.2}$$

where the phase difference $\Delta\phi_{i,j}$ is within the range $[0,2\pi]$. The term $2n\pi$ represents the wrapped phase information since the real phase difference can be larger than 2π.

Equation 3.2 provides a straightforward method to define the horizontal wavelength of a wave. However, this estimation method is limited in two ways. First, the phase difference $\Delta\phi$ defined in this method is based on single wave assumption. It is not possible to derive a constant phase difference if the observed region is perturbed by two or more waves. Second, the minimum horizontal wavelength that can be observed from this method is limited by the Nyquist wavelength, which is twice the sampling distance of the satellite, $\lambda_{x_h,\mathrm{min}} = 2 \cdot \Delta x$. Given a horizontal sampling distance of 100 km, only GW with a horizontal wavelength larger that 200 km can be observed using this method. Otherwise aliasing effects will arise since the discretely sampled profiles are insufficient to capture the wave difference. For this reason, the Nyquist wavelength should be taken into account when unwrapping the real horizontal wavelength from Eq. 3.2.

Here, this phase analysis method is adopted in the temperature retrieval model as an example to show how the horizontal wavelength of a GW can be derived. A simulated

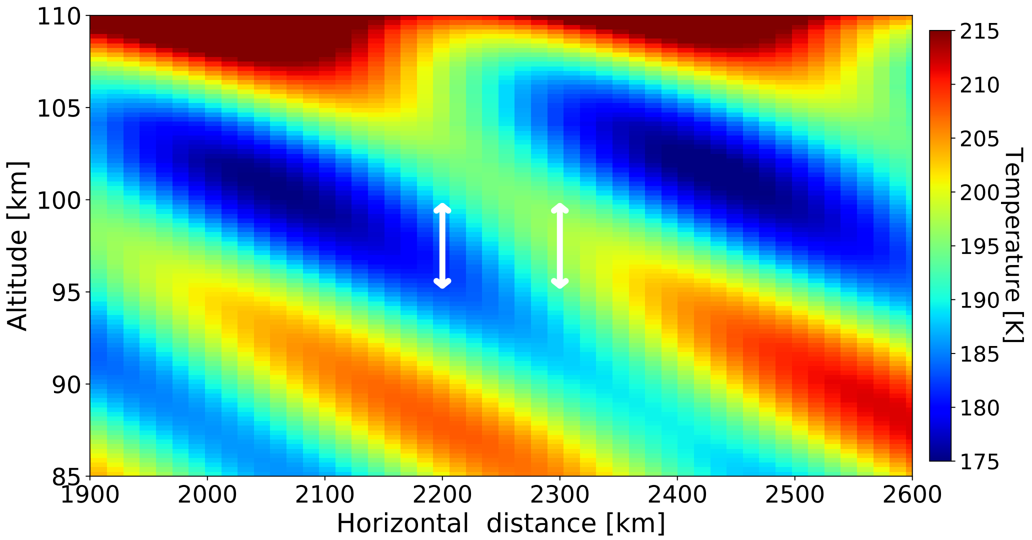

Figure 3.5: 2-D atmospheric temperature at altitude range between 85 and 100 km. The temperature fields are perturbed by a GW with a vertical wavelength of 15 km, horizontal wavelength of 400 km and an amplitude of 10 K. The two white double-head arrows indicate two vertical profiles sampled at a horizontal distance of 100 km.

GW with a vertical wavelength of 15 km, horizontal wavelength of 400 km and an amplitude of 10 K is superimposed on the background temperature fields, as shown in Fig. 3.5. Two limb imaging profiles are acquired with a horizontal sampling distance of 100 km: at 2200 and 2300 km with respect to the position of the satellite along the horizontal axes, respectively. The tangent point distributions for each limb imaging are set the same as in Sect. 3.1, for O_2 A-band nightglow observations. The temperature profile is retrieved at the altitude range between 87 and 100 km. The vertical profiles that reveal the 1-D retrieval results at 2200 km and 2300 km are shown in Fig. 3.6 (a) and (b), respectively.

The wave induced temperature perturbation can be extracted by subtracting the background temperature from the retrieved temperature profile. Fig. 3.7 illustrates the extracted wave perturbations at 2200 km (T_1) and 2300 km (T_2) along the horizontal axes, and a vertical wavelength of 15 km can be clearly seen in both vertical profiles. Since the perturbation profiles (T_1 and T_2) have a phase difference of $\pi/2$ ($\Delta\phi \approx \pi/2$), a horizontal wavelength of ~400 km can be derived from Eq. 3.2 as the longest wavelength. Theoretically, a GW with the same vertical wavelength and amplitude but smaller in horizontal wavelength (i.e. $\lambda_{x_h} = 80$ km) can also generate similar perturbations and phase structures as shown in Fig. 3.7. However, any GWs with a

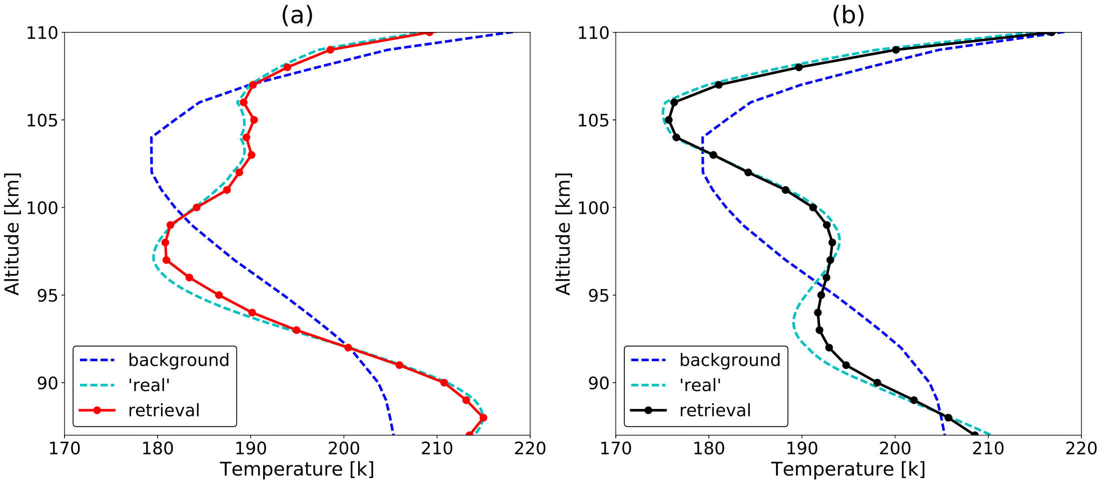

Figure 3.6: 1-D temperature retrieval results at 2200 km (a) and 2300 km (b) along the horizontal axes, corresponding to the positions marked as white double-head arrows in Fig. 3.5. The background temperature and ‘real temperature’ are represented by the dashed dark blue line and dashed light blue line, respectively. The retrieved temperature profiles are represented by the solid red and solid black line in (a) and (b), respectively. The grid points for the retrieved profiles are indicated by dots.

horizontal wavelength below 200 km can not be detected due to the limit of Nyquist sampling distance, and are therefore not considered.

3.2.2 Horizontal wavelength derivation from 2-D tomography

In the previous section, the way of deducing the horizontal wavelength of a GW from the phase difference derived from adjacent vertical profiles was discussed. It provides a straightforward method to resolve 2-D wave structures without extra efforts on modifying the retrieval scheme. However, this method is limited by the sampling distance of the satellite-borne instrument: The shortest horizontal wavelength that can be observed is twice the sampling distance. New observation strategy or retrieval scheme is needed in order to improve the horizontal resolution that current limb sounding measurements can achieve.

From the point of view of the retrieval scheme, a few existing limb sounders try to mitigate this general limitation by considering the horizontal variability of the atmosphere in the retrieval. This includes the Michelson Interferometer for Passive Atmospheric Sounding (MIPAS) (*Carlotti et al.*, 2001) and the SCanning Imaging Absorption SpectroMeter for Atmospheric CHartographY (SCIAMACHY) (*Puķīte et al.*,

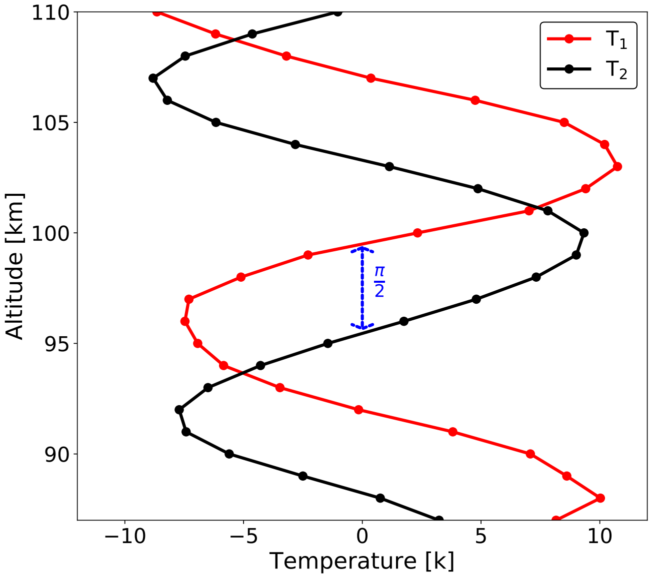

Figure 3.7: Vertical temperature perturbations extracted from the retrieval results at 2200 km (the red curve) and 2300 km (the black curve) in the horizontal direction. The blue double-head arrow indicates the phase difference of $\pi/2$ between the two perturbation profiles.

2010) aboard the ENVISAT satellite; the Optical Spectrograph and InfraRed Imager System (OSIRIS) (*Strong et al.*, 2002) on the Odin satellite; the High Resolution Dynamics Limb Sounder (HIRDLS) (*Gille et al.*, 2003), the Microwave Limb Sounder (MLS) (*Waters et al.*, 1999), and the Tropospheric Emission Spectrometer (TES) (*Beer et al.*, 2001) on the Aura satellite. A common feature of all these instruments is that their LOS is perfectly along or at least close to the orbital plane of the satellite. In this way, the LOSs of adjacent limb measurements overlap with each other in the orbital plane, which means the same atmospheric volume can be observed multiple times from different limb geometries. Therefore, a tomographic retrieval scheme can be applied to resolve 2-D wave structures in the orbital plane. The aim of adopting this tomographic retrieval scheme is to improve the horizontal resolution of limb sounders such that GWs with smaller horizontal wavelength can be observed. In this section, this 2-D limb tomographic retrieval is implemented in the temperature retrieval model by simulating observations for this viewing geometry.

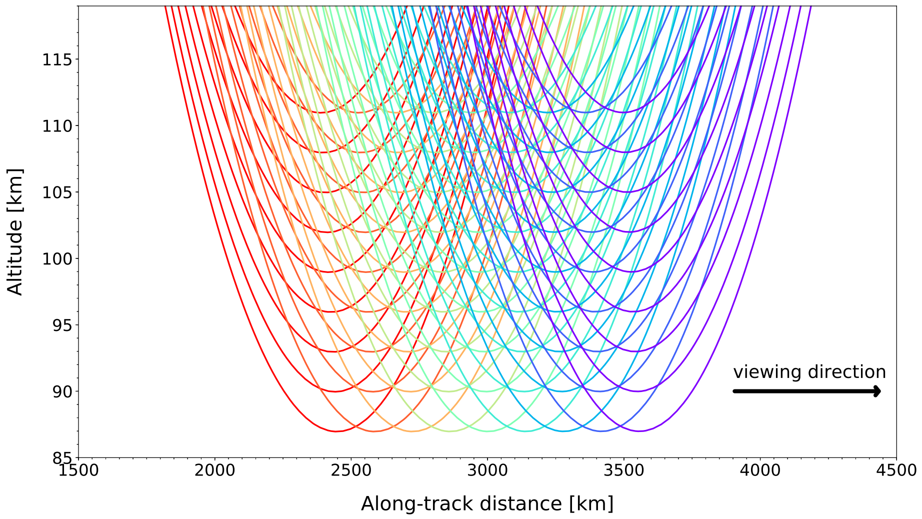

Figure 3.8: Line-of-sights (LOSs) for limb-rays that are sampled 140 km along-track and 3 km vertically. Different colours show measurements from different limb sequences. The viewing direction, which is the same as the flight direction of the satellite, is from the left to the right as indicated by the black arrow. Note that the envisaged instrument has a denser sampling rate, i.e. 70 km along-track and 1.5 km vertically.

3.2.2.1 Case study of a 2-D GW retrieval

In this simulation for limb tomographic retrieval, the instrument is assumed to be perfectly forward-looking, with an integration time of 10 s for O_2 A-band nightglow observations. Limb measurements in the altitude range between 87 and 110 km are used for the tomographic retrieval of 2-D temperature fields. Fig. 3.8 uses an example to show how multiple limb-rays overlap with each other in the atmosphere. The group of nine successive limb profiles with their corresponding limb rays plotted in this figure have a large region ($\sim$2300-3700 km along track) in which the LOSs intersect with each other, leading to the concept of tomographic retrieval. Since the LOSs at lower tangent altitudes can intersect with adjacent LOSs at higher tangent altitudes, the air parcels at higher altitudes are sounded under more geometries than those in the lower altitudes. Fig. 3.9 shows the distribution of tangent points for the simulated limb scans. The tangent points are overplotted on a 2-D temperature field that is perturbed by a GW propagating along the orbital track.

The atmospheric conditions and observation geometries described here are incorporated into the forward model to simulate the observed spectra. The temperature field is then retrieved from the simulated spectra by solving the nonlinear inverse problem, in

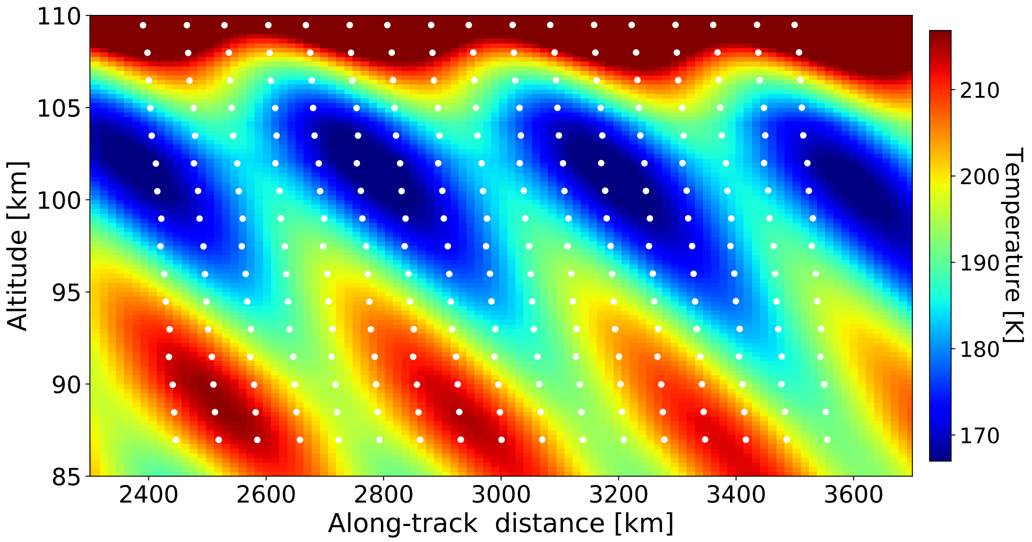

Figure 3.9: A 2-D temperature field perturbed by a GW with a vertical wavelength of 15 km, horizontal wavelength of 400 km and an amplitude of 10 K. White circles represent the tangent points sampled 70 km along-track and 1.5 km vertically.

order to demonstrate the feasibility of this observation strategy in detecting 2-D atmospheric structures. In this study, the spacing of the atmospheric grids is very important for both the forward and the retrieval model. To reduce the impact of the discretization on the synthetic measurements, the atmospheric grid in the forward model should be finely sampled. In this experiment, the atmospheric grid used in the forward model has a vertical spacing of 250 m and a horizontal spacing of 6.25 km. In the inverse procedure, the sampling can be coarser: 500 m vertical spacing and 12.5 km horizontal spacing in this case.

Figure 3.10 shows the retrieval results for the limb tomographic observations with 1% measurement errors added. Fig. 3.10 (a) represents the a priori atmosphere, which is also used as the background atmosphere in this simulation. Fig. 3.10 (b) depicts the simulated GW which is superimposed on the background atmosphere. Instead of showing the retrieved temperature fields, Fig. 3.10 (c) shows the resolved waves by subtracting the background atmosphere from the retrieval results. It is clearly seen that the resolved wave structures are consistent with the simulated wave perturbations, especially in the higher altitudes. In the lower altitudes, insufficient intersections of limb rays can cause a phase shift in the resolved waves. Fig. 3.10 (d) shows the difference between the retrieval results and the simulated ‘real atmosphere’. The temperature differences are below 3 K in most regions, whereas larger differences occur in the lower boundary.

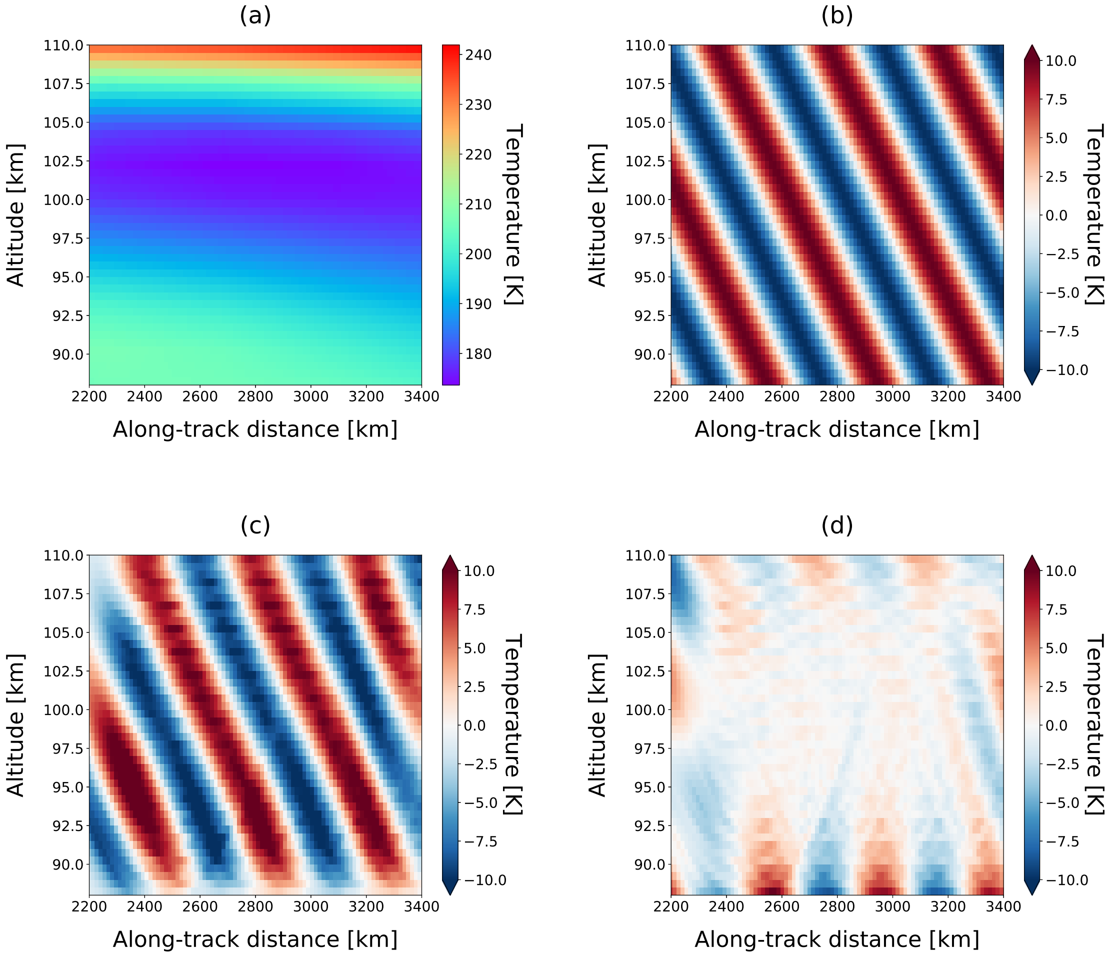

Figure 3.10: Limb tomographic retrieval results using simulated data. The atmospheric conditions and observation geometries are set the same as in Fig. 3.9. The GW has a vertical wavelength of 15 km, a horizontal wavelength of 400 km and an amplitude of 10 K. The a priori atmosphere is depicted in panel (a). The difference between the perturbed atmosphere and the a priori is shown in panel (b). The resolved wave perturbation, which is obtained by subtracting the a priori from the retrieval results, is given in panel (c). The difference between the retrieval results and the true state of atmosphere is shown in panel (d).

The difference map exhibits a specific pattern which is close to the wave induced temperature perturbation. This is caused by the smoothing in the vertical and horizontal direction.

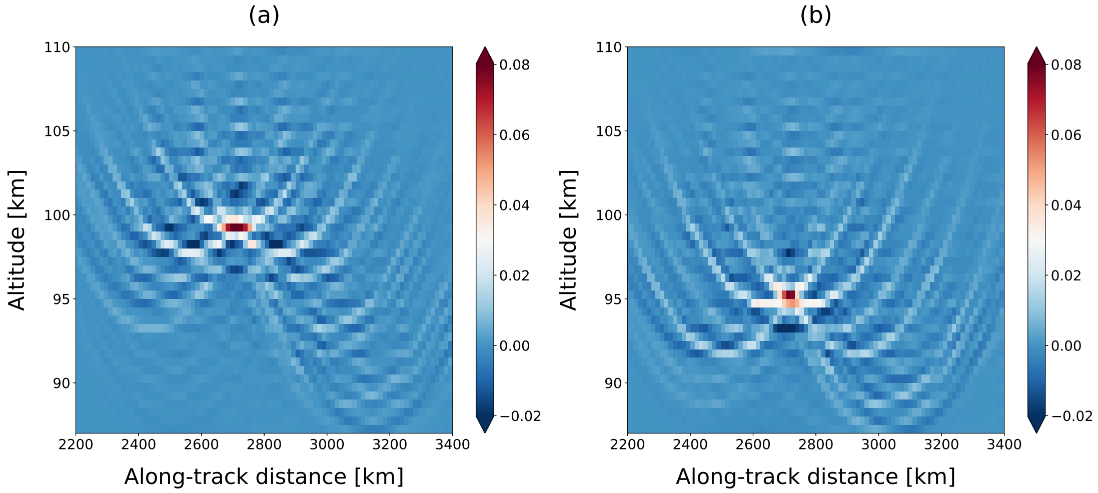

Figure 3.11: Averaging kernel matrix for grid points at 2710 km along track and 99 km altitude (a), and at 2710 km along track and 95 km altitude (b).

The spatial resolution of the retrieved data is described by the rows of the averaging kernel matrix **A**. By reordering a single row of **A** according to the specified vertical and horizontal coordinates, the influence of each point on the retrieval results can be revealed on a 2-D plane. Fig. 3.11 (a) shows the averaging kernel matrix for a point at 2710 km along track with respect to the position of the satellite and 99 km altitude. This point is located at one tangent altitude of the simulated limb measurements. The 2-D averaging kernel indicates that the measurement contribution is sharply centred around this point. A minor part of information, which appears as parabola shaped tracks, comes from limb rays at lower tangent altitudes from adjacent measurements. Fig. 3.11 (b) shows the averaging kernel matrix for a point at 2710 km along track and 95 km altitude. Since this point is placed between the tangent altitudes of 94.5 km and 96 km, main contributions to the retrieved value come from measurements of adjacent grid points. The spatial resolution of the results is derived from the averaging kernel matrix using the FWHM method in the corresponding coordinate. In this experiment, the vertical and horizontal resolution of the retrieval results are within the range of 1.0-1.3 km and 80-110 km, respectively.

3.2.2.2 Systematic investigation of the sensitivity to reconstruct GW parameters

The quality of a GW amplitude-, wavelength- and phase- retrieval depends on the wavelength of the wave. The long LOS of limb observations is ideal for the reconstruction of long horizontal wavelengths, whereas GWs with short horizontal wavelengths are likely underestimated or cannot be measured at all. A measure to assess the sensitivity of an observation system to retrieve GW parameters is the so called GW sensitivity function (*Preusse et al.*, 2002). It defines how a wave perturbation of a given horizontal and vertical wavelength is reproduced by a retrieval. One option to determine this GW sensitivity function is to perform the retrieval for the wavelength of interest. However, for a tomographic retrieval this is computationally very expensive. Alternatively, one can derive the GW sensitivity function more efficiently by using the averaging kernel matrix method (*Rodgers*, 2000). The basic idea of this method is to assume that the forward model can be approximated linearly for a small perturbation as induced by a GW. In this case, the averaging kernel matrix **A** would be identical for the unperturbed atmosphere and the perturbed atmosphere. If the unperturbed atmosphere $\boldsymbol{x}_b$ is assumed to be the same as the a priori data $\boldsymbol{x}_a$, the retrieval result $\boldsymbol{x}_f$ and the a priori vector $\boldsymbol{x}_a$ are related as follows:

$$\boldsymbol{x}_f - \boldsymbol{x}_a = (\mathbf{A}(\boldsymbol{x}_a + \boldsymbol{x}_\delta) + (\mathbf{I} - \mathbf{A})\boldsymbol{x}_a) - \boldsymbol{x}_a = \mathbf{A}\boldsymbol{x}_\delta \tag{3.3}$$

with **I** being the identity matrix and $\boldsymbol{x}_\delta$ being the modulated wave structure. Following this equation, the averaging kernel matrix **A** maps the true wave perturbations $\boldsymbol{x}_\delta$ onto the retrieved wave structure $\boldsymbol{x}_f - \boldsymbol{x}_a$. The ratio between $\boldsymbol{x}_f - \boldsymbol{x}_a$ and $\boldsymbol{x}_\delta$ quantifies the sensitivity to reconstruct the GW. If the ratio is close to 1, it means that the amplitude as well as the wavelength can be perfectly reproduced for the given wave. Conversely, a ratio close to 0 means that the wave parameters cannot be resolved using the current observations or retrieval setup.

Fig. 3.12 shows the sensitivity map of this experiment for limb tomographic retrieval. The sensitivity is calculated at horizontal wavelengths of 20-500 km and vertical wavelengths of 2-60 km with a 0.5 km step. The finest resolvable horizontal wavelength, which is assumed to have a sensitivity value larger than 0.5, is 150 km for a vertical wavelength of 7 km. The retrieval is more sensitive to waves with longer horizontal wavelengths. For all examined GWs with horizontal wavelength larger than 400 km, a sensitivity greater than 0.8 can be achieved, therefore not shown in this figure. In the vertical direction, the sensitivity value drops with increasing vertical wavelength. For example, for a GW with a horizontal wavelength of 300 km, the sensitivity decreases below 0.5 for a vertical wavelength of 30 km. At all examined waves, the sensitivity drops quickly at vertical wavelength below 5 km, due to insufficient vertical sampling of the measurements.

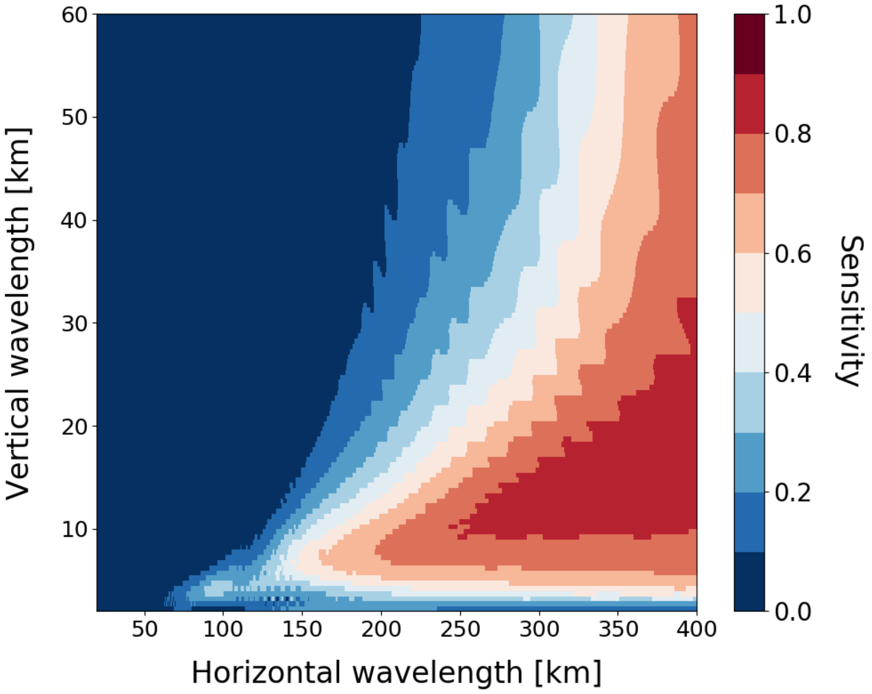

Figure 3.12: GW sensitivity function for a sequence of limb observations analyzed by a 2-D tomographic retrieval. The sensitivity value depicts the ratio of retrieved wave amplitude to true wave amplitude as a function of horizontal and vertical wavelength.

3.3 'Target mode' observation

In Sect. 3.2, the methods for the retrieval of 2-D GW structures were presented. Retrieval experiments and sensitivity analysis from simulated measurements demonstrate the feasibility of resolving 2-D wave structures using the envisaged satellite-borne airglow observations. 2-D GW structures can be obtained from 1-D retrievals by analyzing the phase difference derived from adjacent vertical profiles. 2-D GW structures can be also obtained from 2-D tomographic retrievals. However, this requires the LOSs of limb measurements to be along the orbital track. The main difference between 1-D and 2-D retrievals is that 2-D retrievals improve the sensitivity for shorter horizontal wavelengths. It is also worth noting that 2-D retrievals can produce wave structures with less distortions than 1-D retrievals (*Ungermann et al.*, 2010). Although 1-D and 2-D retrievals are both capable of deducing 2-D wave structures, the observable horizontal wavelength is highly dependent on the horizontal sampling distance of the instrument. However, for a layered airglow emission with optically thick condition below the emission layer, there exists another method for resolving 2-D wave structures. This method is called ‘target mode’, which is a combination of limb and sub-limb observations.

3.3.1 Observational geometry of ‘target mode’

In this section, the viewing geometry of the proposed ‘target mode’ is introduced. It describes how the satellite allows switching between the limb viewing and sub-limb viewing using simulated measurement tracks. Before this ‘target mode’ is presented, an introduction about the viewing geometry of sub-limb soundings is given at the beginning of this section.

3.3.1.1 Limb and sub-limb measurements

Figure 3.13 shows a schematic drawing of the viewing geometries for limb sounding, nadir sounding and sub-limb sounding. In limb geometry, the instrument looks tangentially towards the edge of the Earth’s atmosphere. Along the ray path, the point closest to the Earth’s surface is called the tangent point. The tangent altitude is then defined as the distance between the tangent point and the surface. Utilizing a 2-D detector, the limb sounder can take measurements at different tangent altitudes in one image, thus providing simultaneous information about the vertical structure of the local atmosphere.

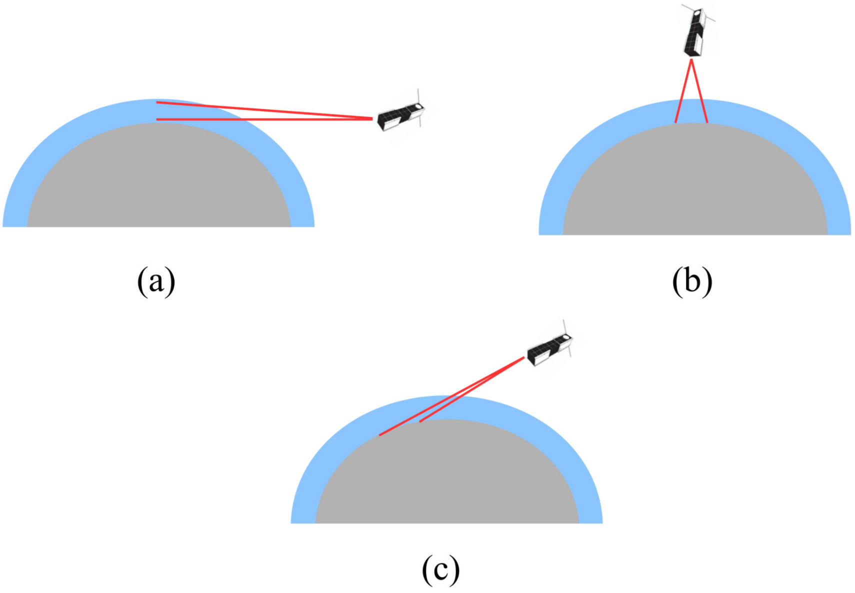
(a)

(b)

(c)

Figure 3.13: Schematic of the observation geometry for the limb sounding (a), nadir sounding (b) sub-limb sounding (c). The blue layer represents the Earth’s atmosphere. The red lines indicate the LOSs of the instrument.

In nadir measurement mode, the instrument looks perpendicularly to the Earth's surface and the atmospheric volume beneath the instrument is probed directly. Nadir sounding gives higher horizontal resolution at the expense of coarse vertical resolution. The horizontal resolution is often determined by the extent of field-of-view with which the atmospheric volume is observed.

The sub-limb sounding has a similar geometry as limb sounding, but the tangent points are near or below the Earth's surface. For a layered airglow emission with optically thick condition below the emission layer, sub-limb sounding can provide measurements on the emission layer without being influenced by the radiance from the lower atmosphere or the ground. Compared with limb sounding, sub-limb sounding can improve the horizontal resolution in the measured emission layer, without losing too much vertical resolution. In this study, the limb and sub-limb soundings are combined to perform the 'target mode' observation.

3.3.1.2 Simulation of observational geometry for 'target mode'

In this section, a schematic drawing is used to illustrate the viewing geometry of the 'target mode', as shown in Fig. 3.14. When the satellite is operated in 'target mode', the instrument will start to observe the target atmospheric volume by forward limb imaging first. The instrument will continue to measure under limb geometry for a period of time, and multiple consecutive vertical radiance profiles will be taken during this time. Then, the instrument will switch to a forward sub-limb view with a viewing angle of 114°. This viewing angle is also constant during the sub-limb observations. In this way, the volume will be scanned twice by the limb and sub-limb observations. Depending on the flexibility and possible speed of satellite operations more viewing angles could be used. After the satellite overpasses the target volume, the same measurement sequence will be applied by back-looking at the target volume.

The backward looking depicted in Fig. 3.14 could increase the SNR of the measurements, but it is not necessarily essential for this 'target mode' observation. If the required horizontal resolution can be achieved solely based on forward measurements, the instrument need not look backward to collect additional information on the same atmospheric volume. In this study, we aim to investigate how much spatial sensitivity can be improved by merely incorporating sub-limb soundings. Therefore, geometries of backward limb are not considered in the subsequent simulations and sensitivity studies.

Figure 3.15 shows the time-dependent variation of the viewing zenith angle for this observation mode. The valid range of the viewing zenith angle is [0°, 180°], with 0° looking upwards and 180° doing nadir measurements. In the first 65 seconds, the instrument is measuring the atmosphere in a limb geometry with a viewing zenith angle of 112°. The followed sub-limb measurements with a viewing zenith angle of 114° start

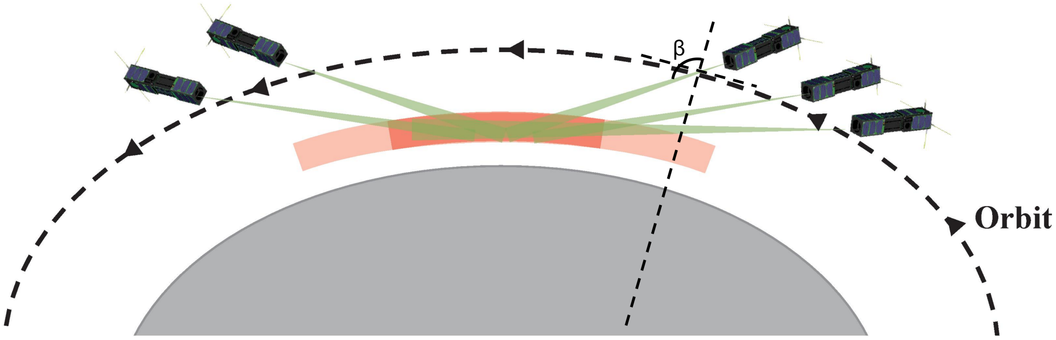

Figure 3.14: Viewing geometry of 'target mode' observations for a region in a mesospheric emission layer. This observation mode consists of forward limb, forward sub-limb and backward sub-limb measurements. The limb sounding measurements are taken with a constant viewing angle of 112°. The sub-limb measurements are taken with two different viewing angles, 114° when the satellite is far from the target region and 125° when it is relatively closer. The viewing angle is defined as the angle between the local zenith and the viewing direction, marked as β in the figure.

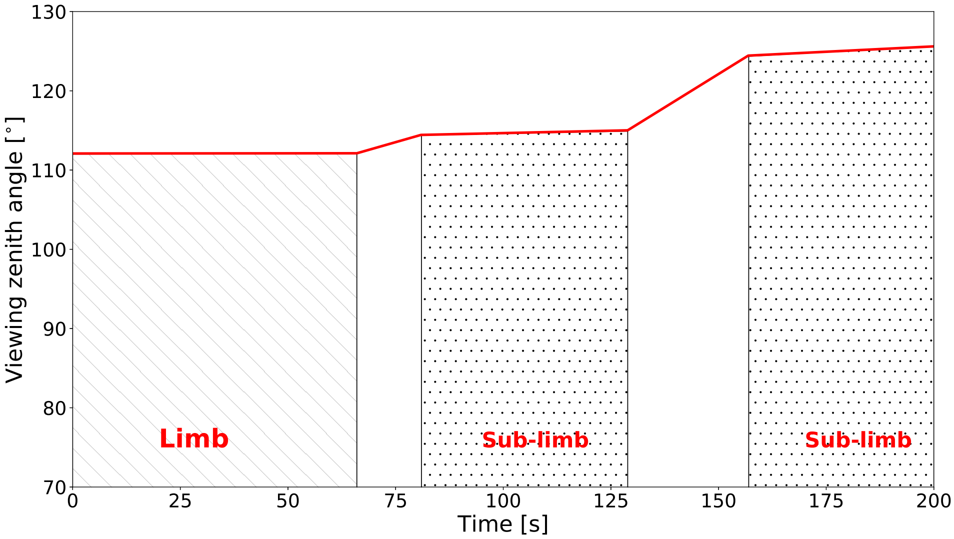

Figure 3.15: Viewing zenith angle dependent on time for the instrument operated in 'target mode'. The limb measurement adopts a constant viewing zenith angle of 112°, while sub-limb measurements have a viewing zenith angle of 114° or even larger.

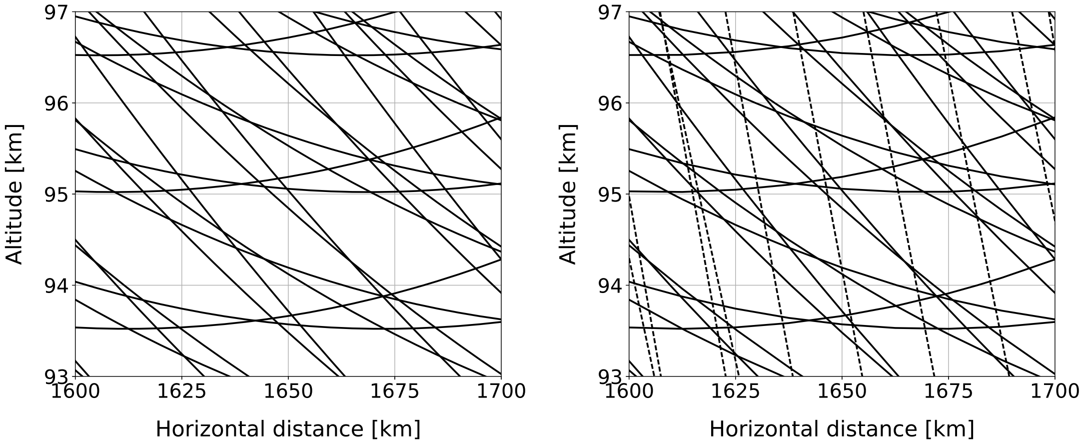

Figure 3.16: LOSs for conventional limb sounding (a) and 'target mode' observation (b). The solid lines represent limb measurements and dashed lines represent sub-limb measurements. Satellite viewing geometry of Fig. 3.16 (b) is the same as in Fig. 3.15.

at t = 84 s and last for 45 seconds. Then the instrument adjusts the viewing zenith angle to 125° in the last 40 seconds. The gap between the different viewing geometries is attributed to the attitude change of the instrument, and ensures that the same atmospheric volume is measured within each observation sequence.

Figure 3.16 shows how the LOSs of the measurements overlap with each other in the orbital plane. The measurement frequency for conventional limb sounding is assumed to be 10 s per vertical profile. As can be seen in Fig. 3.16 (a), for the limb sounding mode the LOSs of consecutive limb profiles overlap in the orbital plane. In 'target mode', the same measurement frequency of 10 s per profile is used for the included limb soundings, and a lower measurement frequency of 15 s per scan for additional sub-limb soundings. To achieve a SNR comparable with limb soundings, the measurement frequency of sub-limb soundings is reduced and individual array pixels are co-added. As shown in Fig. 3.16 (b), the atmospheric volume of the same size as for (a) has more intersection regions due to the introduction of sub-limb measurements.

3.3.1.3 Temperature weighting functions

The weighting function plays an important role in atmospheric soundings. It determines how much one atmospheric volume (the temperature of this volume in this study here) contributes to the measured signal (measured photon radiance here). In this section, the temperature weighting functions for limb and sub-limb soundings, which are the two indispensable components of the 'target mode', are calculated numerically.

Figure 3.17 shows the weighting functions for the selected limb soundings at a wavenumber of 13086.13 cm^{-1}. At altitudes between 87 and 110 km, the maximum sensitivities for individual limb rays are reached at the tangent points. The weighting functions have a global maximum of $\sim 3.16 \times 10^5$ $(\mathrm{photons} \cdot \mathrm{s}^{-1} \cdot \mathrm{cm}^{-2} \cdot \mathrm{sr}^{-1})/\mathrm{K}$ at the specified fine atmospheric grid (4.5 km horizontally and 100 m vertically).

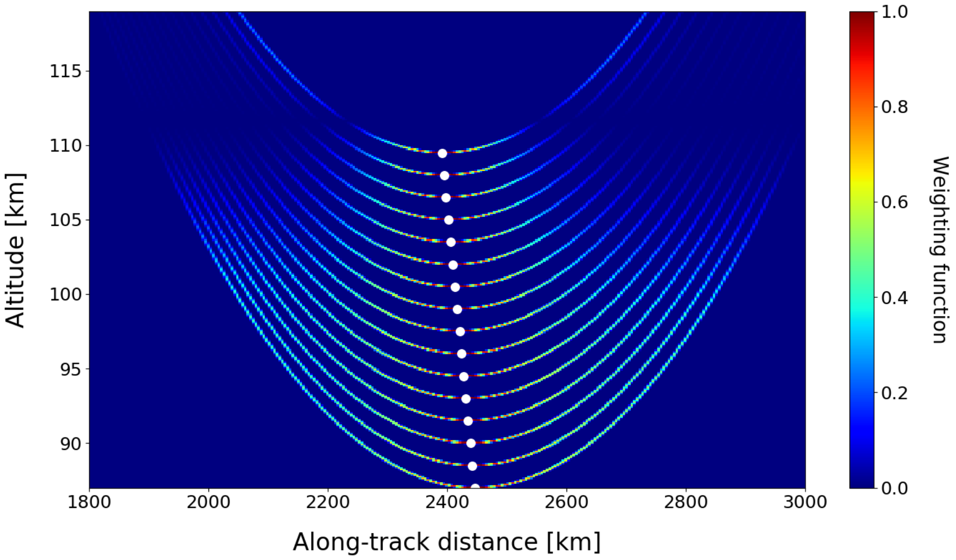

Figure 3.17: The temperature weighting functions for limb soundings at a wavenumber of 13086.13 cm^{-1}. For each limb ray, the weighting functions are normalized to the maximum sensitivity at tangent altitudes. The tangent points, which are placed at altitude between 87 and 110 km with an interval of 1.5 km, are marked by white circles. The weighting functions have a global maximum of $\sim 3.16 \times 10^5$ $(\mathrm{photons} \cdot \mathrm{s}^{-1} \cdot \mathrm{cm}^{-2} \cdot \mathrm{sr}^{-1})/\mathrm{K}$.

In comparison, Fig. 3.18 shows the weighting functions for the sub-limb soundings. The selected sub-limb measurements have their tangent points placed very close to the Earth's surface, approximately 500-600 m beneath the surface. The calculated sensitivity for sub-limb soundings have a maximum value of $\sim 3.54 \times 10^4$ $(\mathrm{photons} \cdot \mathrm{s}^{-1} \cdot \mathrm{cm}^{-2} \cdot \mathrm{sr}^{-1})/\mathrm{K}$, which is a magnitude lower than limb soundings. Therefore, multiple rows of the array pixels are co-added to increase the sensitivity in sub-limb mode. As we can see in the figure, only ten rays are simulated within a total field-of-view of 1.3° from the instrument.

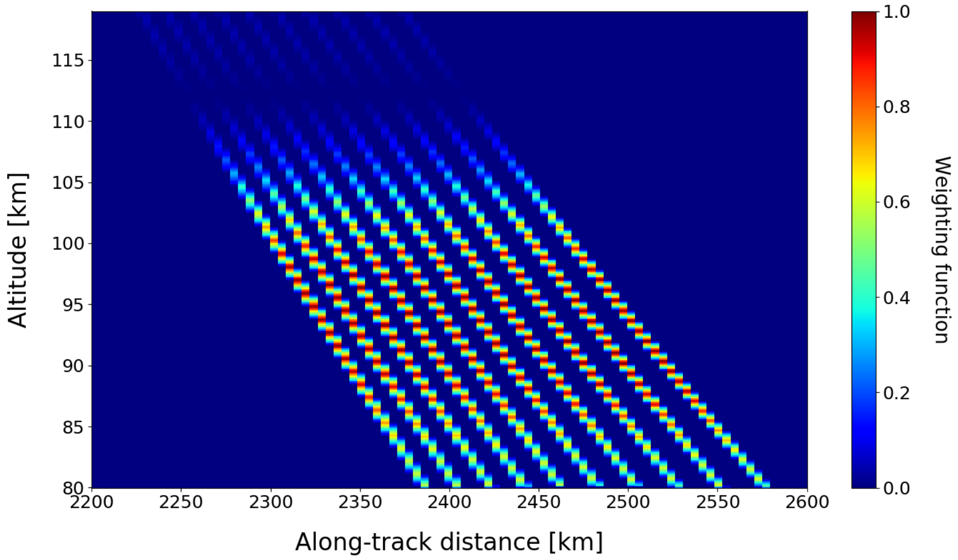

Figure 3.18: The normalized temperature weighting functions for sub-limb soundings at a wavenumber of 13086.13 cm^{-1}. The ten sub-limb rays are within a total field-of-view of 1.3° from the instrument. The corresponding ‘tangent points’ are between 500 and 600 m beneath the Earth’s surface. The weighting functions have a global maximum of $\sim 3.54 \times 10^4$ $(\mathrm{photons} \cdot \mathrm{s}^{-1} \cdot \mathrm{cm}^{-2} \cdot \mathrm{sr}^{-1})/\mathrm{K}$.

3.3.2 Numerical simulations

In this section, the experimental results of tomographic temperature retrievals using simulated ‘target mode’ measurements are presented. Synthetic measurements are generated by imprinting a GW structure onto a smooth atmosphere. The temperature, atmospheric density and concentrations of various constituents are perturbed by the wave as well. It is assumed that the wave vector is along the direction of LOS. For the calculation of simulated satellite measurements, the atmosphere is finely gridded with linear interpolation in the forward model. This finely gridded atmosphere has a vertical spacing of 250 m and a horizontal spacing of 5 km. In the retrieval model, a coarser grid with a vertical spacing of 500 m and horizontal spacing of 12.5 km is used.

Figure 3.19 shows the 2-D temperature fields retrieved from simulated ‘target mode’ observations with 1% noise added. The a priori atmosphere (Fig. 3.19 (a)) and the superimposed GW (Fig. 3.19 (b)) are identical with the simulation shown in Fig. 3.10 for the limb tomographic retrieval. The wave structures obtained from the retrieval results are depicted in Fig. 3.19 (c). The horizontal and vertical wavelength, as well as the amplitude of the wave are well reproduced in this simulation. The difference between the retrieval results and the ‘real atmosphere’ is depicted in Fig. 3.19 (d). Compared

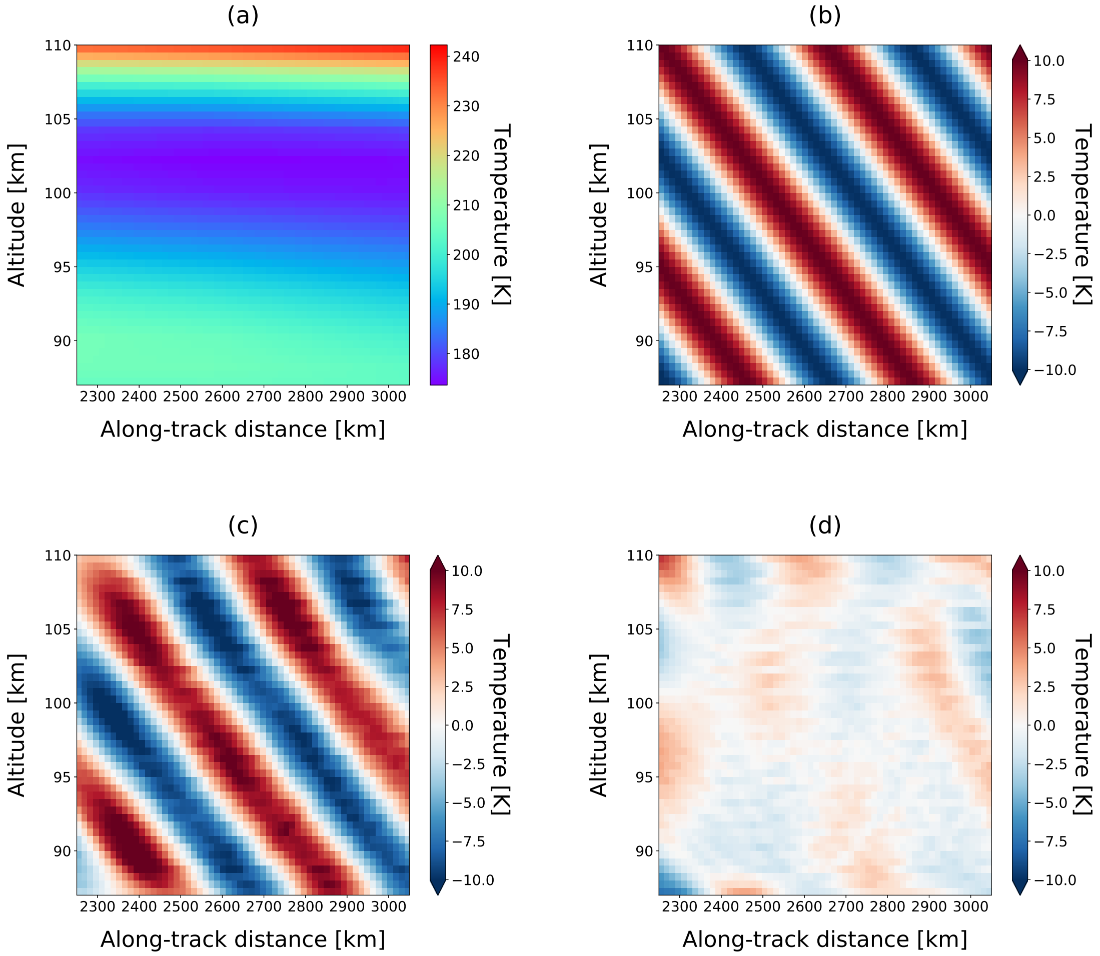

Figure 3.19: ‘Target mode’ retrieval results using simulated data. The atmospheric conditions and GW parameters are set the same as for Fig. 3.10. The GW has a vertical wavelength of 15 km, a horizontal wavelength of 400 km and an amplitude of 10 K. The observation geometries are described in Sect. 3.3.1.2. The a priori atmosphere is depicted in panel (a). The difference between the perturbed atmosphere and the a priori is shown in panel (b). The resolved wave perturbation, which is obtained by subtracting the a priori from the retrieval results, is given in panel (c). The difference between the retrieval results and the true state of the atmosphere is shown in panel (d).

with the difference map of the limb tomographic retrieval (Fig. 3.10 (d)), it is notable that the ‘target mode’ has lower magnitude of errors remained in the retrieval region, which are 0.5 K less on average. Especially at the lower boundary of the retrieval region, a significant improvement in the temperature retrieval accuracy is achieved with the ‘target mode’ observations. In the altitude range between 87 and 90 km, the limb tomographic retrieval has a high temperature uncertainty of 5 K, but can be reduced to less than 1 K in ‘target mode’ retrieval.

Fig. 3.20 shows the averaging kernel matrix for this ‘target mode’ retrieval at 2615 km along track and 97.5 km vertically (a), and 2685 km along track and 100.5 km vertically (b). In addition to parabola shaped tracks contributed by the limb measurements, slanted tracks contributed by the sub-limb measurements can be clearly seen in the averaging kernel. This increases the contribution from the lower atmosphere to the retrieved data points. Utilizing the FWHM method, the calculated vertical resolution of the retrieval result locates between 1.0 and 1.3 km and the horizontal resolution can reach 38 km. This horizontal resolution is an improvement of about 60 km with respect to the limb tomographic retrieval. To better illustrate the performance of the proposed observational strategy for waves with other horizontal and vertical wavelengths, further sensitivity studies are performed.

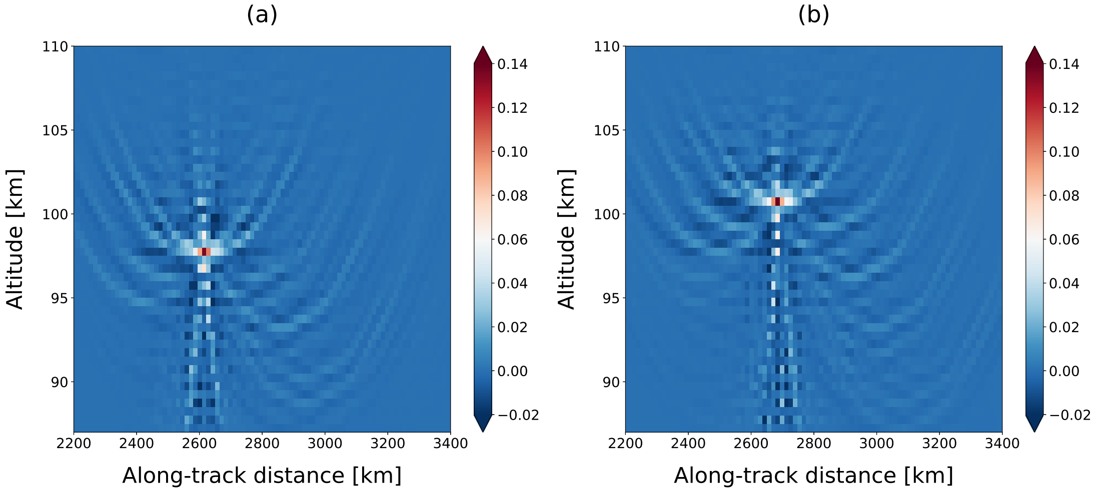

Figure 3.20: Averaging kernel matrix for grid points at 2615 km along track and 97.5 km altitude (a), and at 2685 km along track and 100.5 km altitude (b).

3.3.2.1 Sensitivity analysis for ‘target mode’

To investigate the performance of ‘target mode’ observation to detect the different scales of GWs, a similar approach as presented in Sect. 3.2.2.2 is used. It derives the sensitivity

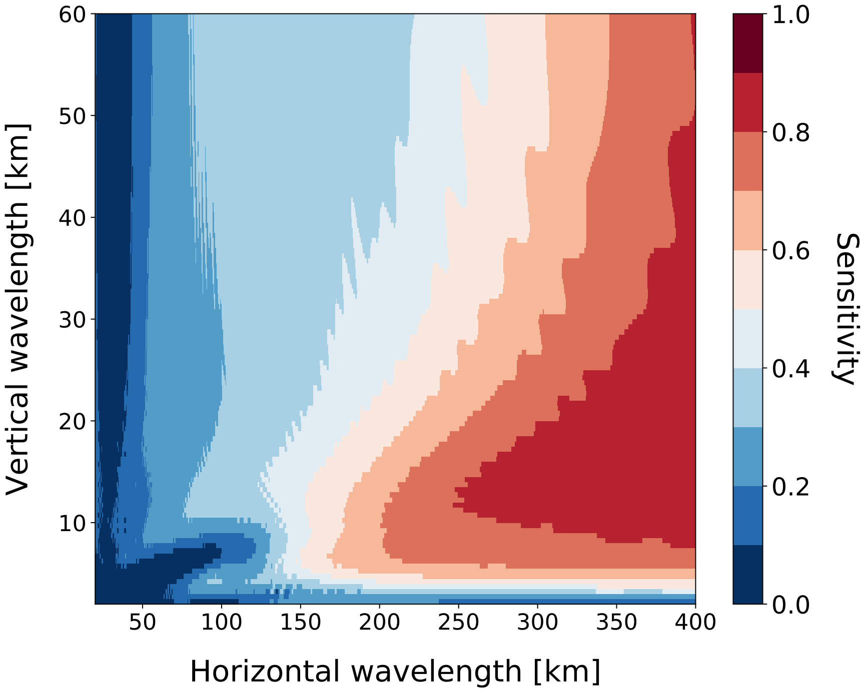

Figure 3.21: GW sensitivity function for ‘target mode’ tomographic retrieval. The sensitivity value depicts the ratio of retrieved wave amplitude to true wave amplitude as a function of horizontal and vertical wavelength.

function of the ‘target mode’ to GWs at vertical wavelength between 2 and 60 km, and horizontal wavelength between 20 and 500 km, as shown in Fig. 3.21. Compared to conventional limb measurements, the GW sensitivity function does not change much for short vertical wavelength, but GWs with large vertical wavelength and short horizontal wavelength become much more visible. For GWs with vertical wavelengths larger than 15 km, the sensitivity of ‘target mode’ to horizontal wavelength is typically 50-100 km shifted towards smaller horizontal wavelengths compared to the sensitivity range of conventional limb measurements.

The sensitivity function shown in Fig. 3.21 is based on the linearity assumption of the forward model. This assumes the Jacobian matrix to be constant for any unperturbed and perturbed atmosphere, and therefore the calculated averaging kernel matrix **A** will be identical for all wave perturbations. However, this linear approximation can not be used to examine the convergence properties of the nonlinear retrievals for different atmospheric states. Therefore, three groups of retrieval results are depicted in Fig. 3.22 to further analyze the performance of limb mode and ‘target mode’ in reconstructing GWs.

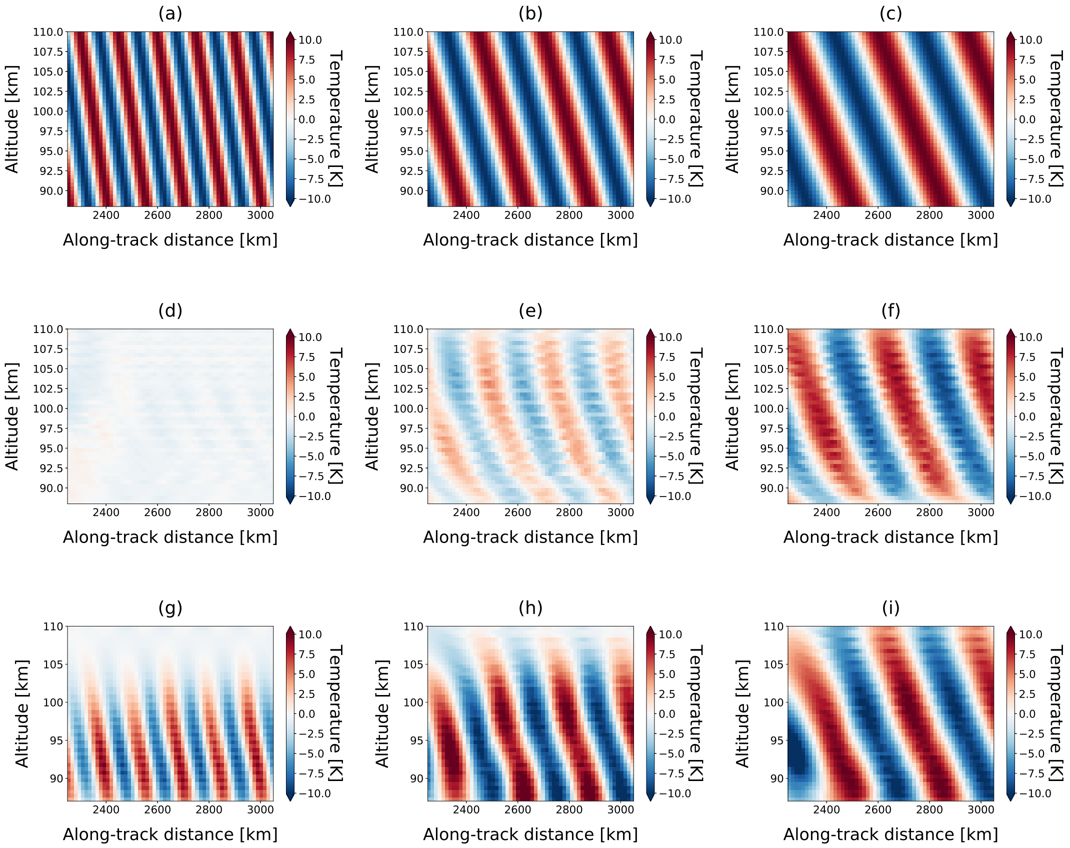

Figure 3.22: Performance of limb mode and ‘target mode’ retrievals depending on the horizontal wavelength of the wave. In the first row, simulated GW perturbations with a vertical wavelength of 30 km and a horizontal wavelength of 150 km, 250km and 350 km are shown in (a), (b) and (c), respectively. The subplots in the second row represent the corresponding wave structures reconstructed from tomographic retrievals using conventional limb measurements. In the third row, wave structures derived from ‘target mode’ tomographic retrievals are depicted.

In this simulation, the vertical wavelength for all the examined waves has a constant scale of 30 km, whereas the horizontal wavelength increases from 150 to 250 and 350 km. When the horizontal wavelength is 150 km, the sensitivity value illustrated in the sensitivity map for limb tomography and ‘target mode’ tomography is close to 0 and 0.3, respectively. In this case, the wave structures derived from limb tomography are barely to see as shown in Fig. 3.22 (d). The 'target mode' could reconstruct the wave structures to some extent, but with lower amplitudes than those of real waves, as shown in Fig. 3.22 (g). Since the weighting functions for both limb and sub-limb measurements decrease significantly above 105 km due to the drop of signal, the wave patterns become less visible at higher altitudes. When the horizontal wavelength of the simulated wave increases to 250 km, the advantage of 'target mode' over limb mode in the amplitude accuracy becomes more obvious, as shown Fig. 3.22 (e) and (h). In addition, the limb retrieval results have a strong phase shift in the lower boundary of the altitude range considered due to insufficient horizontal samplings. In the last column of results showing a GW with a horizontal wavelength of 350 km, both methods can obtain well reproduced wave structures without obvious amplitude suppression and phase shift.

Considering the intensity of the A-band signal for the nightglow layer maximum and the detector performance, an integration time of 60 s is required to derive temperature with a noise error of 1.5 K for limb measurements. The simulated 'target mode' observation is, however, based on an assumed integration time of 10 s for limb measurements and 15 s for sub-limb measurements. To investigate the realistic performance of 'target mode' in reconstructing waves, a group of retrievals based on the measurements with different sampling rates are performed.

Figure 3.23 shows the waves structures resolved from limb mode (a, c and e) and 'target mode' (b, d and f) observations. The simulated GW has a vertical wavelength of 30 km, a horizontal wavelength of 250 km and an amplitude of 10 K. For conventional limb mode, the integration time of (a), (c) and (e) are 10 s, 30 s and 60 s, respectively. For 'target mode', the integration time of (b), (d) and (f) are 10 s, 30 s and 60 s for the included limb measurements, and 15 s to 45 s and 90 s for the included sub-limb measurements, respectively.

As shown in Fig. 3.23 (a), (c) and (e), the wave structures resolved from conventional limb mode become less invisible with increasing integration time. When the integration time reaches 60 s in (e), the measurements sampled with a horizontal sampling distance of 400 km fail to reconstruct the examined GW with a horizontal wavelength of 300 km. In comparison, the wave structures resolved from 'target mode' also become blurred with increasing integration time, but are more clear than those derived from limb mode in all cases. In (f), the resolved intensity peak and trough are contributed by the sub-limb measurements sampled at a horizontal distance of 650 km.

3.3.3 Horizontal wavelength analysis

The results presented so far are based on 2-D radiative transfer calculations. This kind of observation can only quantify the projection of a wave onto the LOS. Since the in-

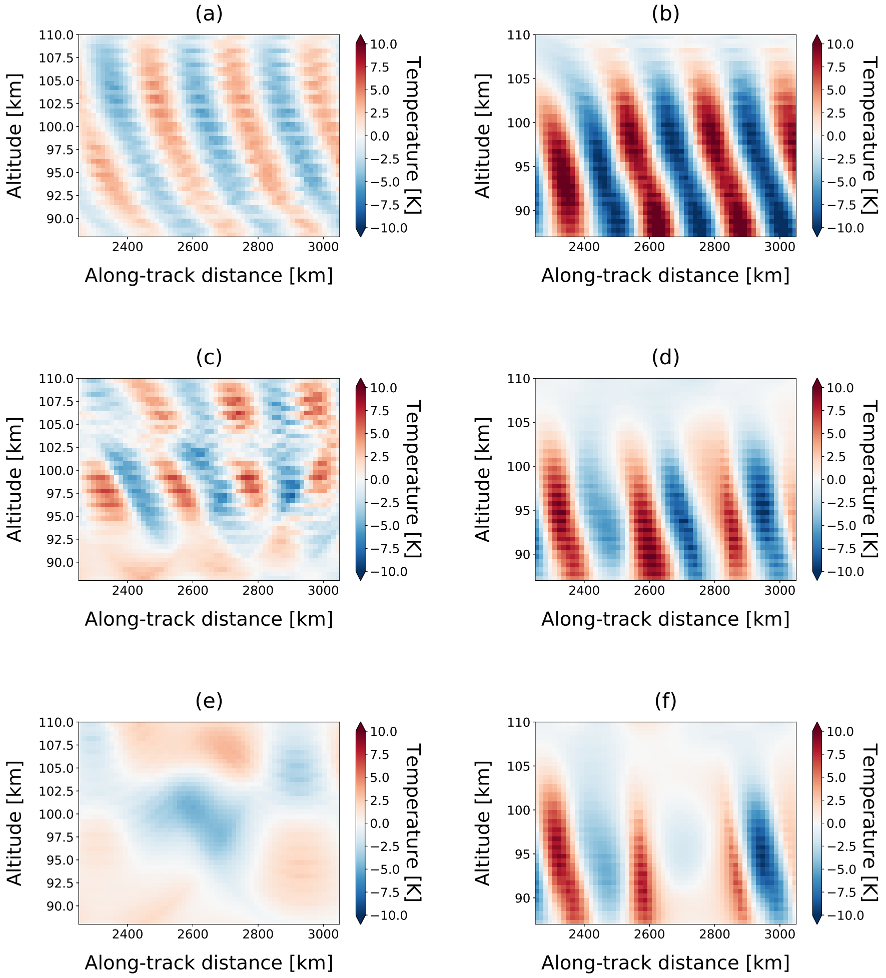

Figure 3.23: Performance of limb mode (a, c and e) and ‘target mode’ (b, d and f) retrievals depending on different integration time of the instrument. The simulated GW has a vertical wavelength of 30 km, a horizontal wavelength of 250 km and an amplitude of 10 K for all retrievals. For limb mode, the integration time of (a), (c) and (e) are 10 s, 30 s and 60 s, respectively. For ‘target mode’, the integration time of (b), (d) and (f) are 10 s, 30 s and 60 s for the included limb measurements, and 15 s to 45 s and 90 s for the included sub-limb measurements, respectively.

strument is likely to view the real 3-D waves at various directions, there is generally an angle α between the LOS and the real horizontal wave vector, as illustrated in Fig. 3.24. Therefore, the observed horizontal wavelength λ_x is generally larger than the real horizontal wavelength λ_real:

$$\lambda_\mathrm{x} = \frac{1}{\cos\alpha}\,\lambda_\mathrm{real} \tag{3.4}$$

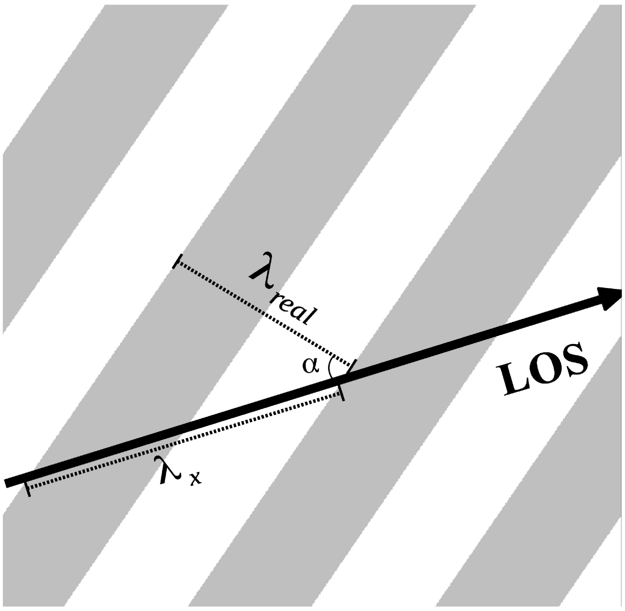

Figure 3.24: Viewing geometry between the satellite LOS and the horizontal wave vector. The wave fronts are represented by the gray shading. The observed horizontal wavelength λ_x and the real horizontal wavelength λ_real are related by an angle α.

For example, if the instrument operated in 'target mode' views waves with vertical wavelength of 30 km at an angle α of 60°, the shortest horizontal wavelength that can be resolved is then improved from 220 km to 110 km. It implies that the limb and 'target mode' tomographic retrievals have better performance in capturing small-scale GWs than that revealed from the 2-D sensitivity functions.

3.4 Chapter summary

The method of temperature retrieval using O_2 A-band nightglow observations was examined using simulated limb measurements by assuming a horizontally homogeneous atmosphere. The temperature perturbations obtained from the retrieval results allow the derivation of the vertical structure of GWs in the mesopause region.

The approach of estimating the horizontal wavelength of GWs from adjacent vertical profiles was applied in this observation model. This method avoids the reconstruction of a 2-D wave field, but instead estimates the horizontal wavelength from the phase difference of adjacent vertical profiles.

The conventional limb tomographic observations were also simulated in this model, in order to investigate its ability in resolving real 2-D GWs. Experiment results show that 2-D GW structures can be well reproduced from the retrieved temperature fields. A sensitivity function determined by the ratio between the resolved and simulated wave perturbations was used to analyze the performance in reconstructing various waves. Assuming an integration time of 10 s for nightglow observations, it was shown that GWs with vertical and horizontal wavelength down to 7 km and 150 km can be resolved. The sensitivity to detect short horizontal wavelengths decreases for larger vertical wavelengths, e.g. 250 km at 20 km vertical wavelength, or 325 km at 60 km vertical wavelength, respectively.

A new observation strategy, called ‘target mode’, for GWs in the mesopause region was proposed. It combines limb and sub-limb measurements for improving the spatial resolution that conventional limb sounders can achieve. This ‘target mode’ works only for the observation of layered airglow emissions with optically thick condition below the emission layer. It shows that one major advantage of this observation mode is that GWs can be observed on much smaller scale than conventional limb measurements. The derived sensitivity function implies that the ‘target mode’ observations are able to capture GWs with horizontal wavelengths as short as $\sim$50 km for a large range of vertical wavelengths. This is far better than the horizontal wavelength limit of 100-200 km obtained from conventional limb measurements. To investigate the realistic performance of this ‘target mode’ in reconstructing waves, a group of retrievals based on the measurements with different sampling rates were performed.

Chapter 4

‘Sweep mode’ 3-D tomographic reconstruction of GW parameters

A major limitation of the observation mode presented before is that only the projection of the wave vector onto the instrument’s LOS can be determined. If the GW propagates 90° perpendicularly to the orbital track, the horizontal structure of the wave is virtually invisible from the retrieval results. In other words, the real horizontal wavelength is inaccessible without the knowledge of the propagation direction of the wave. This limits the ‘target mode’ in practical application where GWs can propagate in any direction. To solve this problem, another observation strategy, called ‘sweep mode’, is presented in this chapter. This observation strategy consists of two different modes, namely the ‘sweep mode A’ and ‘sweep mode B’. They are capable of reproducing 3-D atmospheric structures using tomographic reconstruction techniques. GWs resolved from this observation strategy are more realistic in terms of wavelength, amplitude and even propagation direction. A sensitivity study is conducted to analyze how well this observation strategy performs in resolving small-scale GWs that propagate at various directions in the horizontal plane. The observation strategy presented in this chapter is applicable to any kind of emissions, including layered and non-layered.

4.1 ‘Sweep mode A’ observation strategy

The basic idea of 3-D tomography is to sound a target volume from multiple viewing directions. It differs from 2-D tomographic observations where the instrument’s LOSs stay along the orbital plane. In the case of an airborne platform, a 3-D tomographic observation can be realized either by performing closed flight patterns that enclose the volume of interest, or by panning the instrument’s LOS during flight. Such an observation scenario was suggested by *Ungermann et al.* (2011) and applied by *Kaufmann et al.* (2015) and *Krisch et al.* (2017) for an airborne infrared limb sounder. Fig. 4.1 shows the concept for this 3-D tomographic observation by flying around the volume of interest. The flight track of the aircraft gives 360° viewing angles in the central area, and the tangents points of consecutive measurements form a 3-D volume therein. As a result, a large number of tangent points are densely placed in the volume of interest, such that a 3-D tomographic retrieval scheme can be performed.

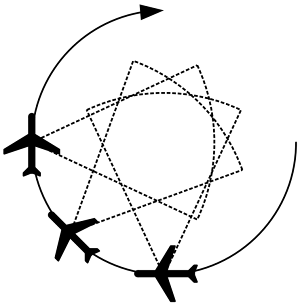

Figure 4.1: Schematic drawing of 3-D tomographic circular flight path for GLORIA (*Ungermann et al.*, 2011).

4.1.1 Observation geometry of 'sweep mode A'

To implement a similar observation strategy from space, multiple satellites or a single satellite being capable of sweeping its LOS would be necessary. For a single satellite, the same atmospheric volume can be measured from multiple angles if the instrument sweeps its LOS in the horizontal plane under a specific slew rate. The high-performance attitude control system provides the instrument with the ability to sweep the LOS accurately. Fig. 4.2 illustrates the concept of this 3-D tomographic viewing geometry for a satellite-borne instrument. This observation mode is called 'sweep mode A', in order to distinguish it from another sweep mode which will be introduced in the next section.

By switching the satellite from forward looking to backward looking, the atmospheric volume, which is depicted as a transparent dark blue box in Fig. 4.2, is viewed multiple times at different positions. Because a satellite-borne instrument moves very fast, performing an observation depicted in Fig. 4.2 takes $\sim$10 minutes at most, whereas an airborne instrument would require hours of flight time to take the measurements. However, only a limited number of measurements can be collected from a satellite-borne instrument in this mode. So the problem lies in how to use the limited number of measurements efficiently for the 3-D tomographic retrieval.

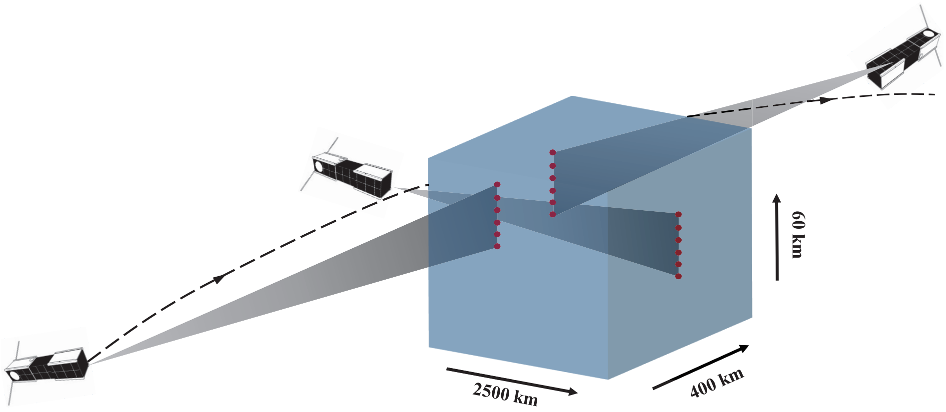

Figure 4.2: Schematic drawing of the 3-D tomographic observation geometry for a satellite-borne instrument. Red circles represent the positions of tangent points from individual images. The three measurements represent a forward looking, a backward looking, and a looking direction perpendicular to the orbital track. In practice, the sampling rate of the instrument is much higher than depicted here.

Figure 4.3 illustrates the measurement tracks and tangent point distribution for the ‘sweep mode A’ and conventional limb mode in (a) and (b), respectively. Since sub-limb measurements are not considered, this observation strategy can be also used for non-layered, arbitrary emissions. In this simulation, a sampling rate of 6 s per vertical profile is used for measuring the O_2 A-band dayglow emission. The coloured lines in Fig. 4.3 represent the LOS segments, i.e. the LOSs within a 1 km vertical layer above the tangent point, projected on the horizontal plane. The locations of corresponding tangent points are marked as coloured circles. In ‘sweep mode A’, to perform a group of limb measurements by switching the instrument from froward to backward looking, a flight time of 10 minutes is needed. As shown in Fig. 4.3 (a), the tangent points of consecutive limb scans concentrate between 2200 and 2400 km along the orbital track, while extending to a distance of 2400 km away in the direction across the orbital track. For comparison, the measurement tracks for conventional limb scans with a constant viewing azimuth angle of 0° and 90° are shown in Fig. 4.3 (b). The viewing azimuth angle is here defined as the angle between the flight direction and the LOS.

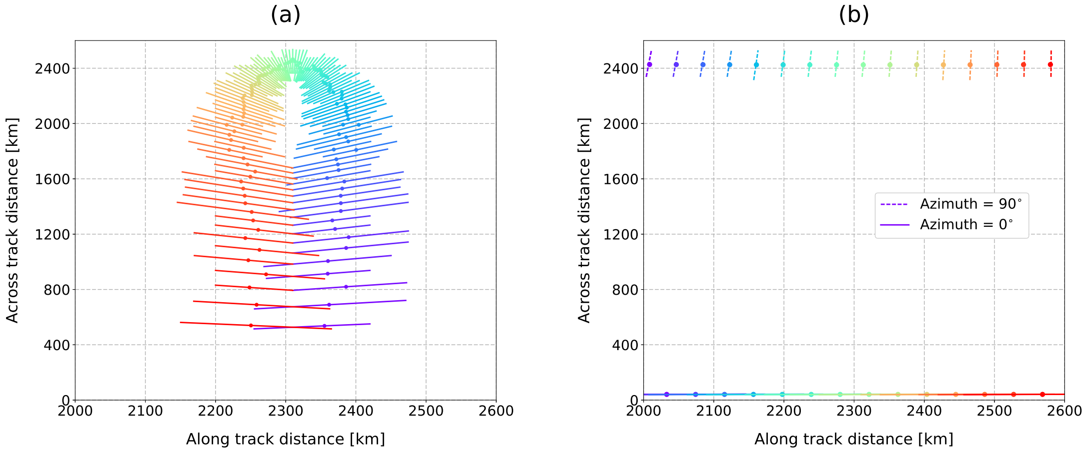

Figure 4.3: Illustration of the central measurement track for the 'sweep mode A' (a), and conventional limb mode (b). The flight direction of the satellite is to the right. For a single measurement, the LOS that targets at 90 km tangent altitude is traced. The coloured solid lines indicate the LOSs within a 1 km vertical layer above the tangent point. The locations of corresponding tangent points are represented by the coloured circles. In (b), two limb observation modes with different viewing azimuth angles, 0° (solid line) and 90° (dashed line), are traced. The along track distance describes the movement of tangent point in time with respect to the satellite position.

4.1.2 Case study of a GW retrieval

To undertake a comprehensive investigation of the 'sweep mode A', quantitative evaluation of its performance in temperature retrieval and sensitivity to reconstruct GWs is needed. In this section, a case study is conducted for the aim of examining how well 3-D wave structures can be extracted from this 3-D tomographic retrieval. In the 'sweep mode A', the instrument has a field-of-view extending from 60 to 120 km vertically, where O_2 A-band dayglow can be properly observed. In this altitude range, each measurement profile contains 40 spectra with a vertical sampling of 1.5 km. The background atmosphere information is taken from the HAMMONIA model run from 5° N to 5° S and 130° W to 155° W.

The performance of this 'sweep mode A' to reconstruct the orientation of a GW is illustrated in Fig. 4.4. The simulation shown in this figure is for a GW with an amplitude of 5 K, a vertical wavelength of 15 km and a horizontal wavelength of 425 km that propagates with an angle of 45° to the flight direction. Fig. 4.4 shows a horizontal slice of the resolved 3-D wave structures at an altitude of 90 km. The same retrieval is able to reconstruct the vertical structure of the wave (not shown) as well. Similarly,

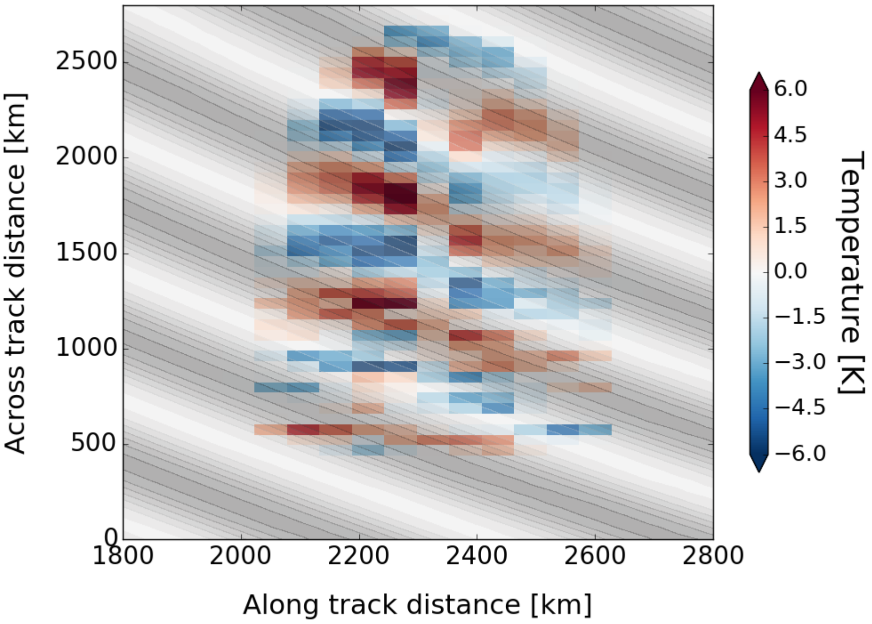

Figure 4.4: A horizontal slice of GW structures extracted from the ‘sweep mode A’ retrieval results for an altitude of 90 km. The grey shading in the background indicates the wave fronts of the simulated GW. In the horizontal plane, the simulated GW has a wavelength of 425 km with an angle of 45° to the flight direction. This wave induces a small perturbation of 5 K on the background atmospheric temperature. The red-blue phase patterns indicate the GW extracted from the temperature retrieval results.

GW structures extracted from the retrieval results of conventional limb modes with a viewing azimuth angle 0° and 90° are depicted in Fig. 4.5.

The retrieval results from Fig. 4.4 and Fig. 4.5 give a visual clue of how the ‘sweep mode A’ can be used to resolve the orientation of a GW. As shown in Fig. 4.4, a wave pattern consistent with the simulated GW can be clearly seen in the temperature perturbations extracted from the retrieval results, especially between 2100 km and 2500 km along-track, and 600 km and 2500 km across-track. At some data points, the slightly amplified temperature amplitudes are caused by the uncertainty of the retrieval process. Fig. 4.5 contains the wave structures derived from conventional limb modes with two different viewing azimuth angles. When the viewing azimuth angle equals to 0°, the results (shown in the bottom of Fig. 4.5) are similar to those obtained from 2-D limb tomography (cf. Sect. 3.2.2). Since the atmospheric temperature is retrieved in a 2-D vertical plane along the orbital track, the across-track information cannot be obtained in

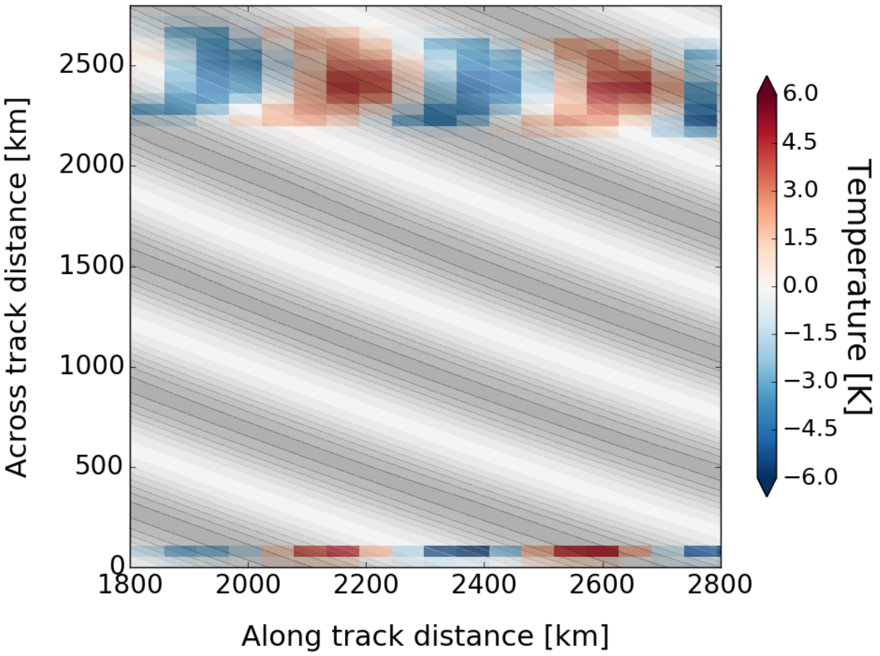

Figure 4.5: A horizontal slice of GW structures extracted from conventional limb modes with a viewing azimuth angle of 0° (in the bottom region) and 90° (in the top region). The atmospheric conditions and simulated GW are set the same as in Fig. 4.4.

this case. Therefore, only a thin layer of data that represents the projection of a wave can be found along orbital track. When the instrument's LOS is oriented perpendicular to the satellite flight direction, the results are shown in the top of Fig. 4.5, with resolved temperature perturbations being broadened by $\sim$300 km in the across-track direction. However, wave structures across the orbital track can still hardly be seen since the atmospheric variations in this direction are smoothed within individual limb measurements.

The result of the 'sweep mode A' shown in Fig. 4.4 indicates that the resolved wave structures in the across-track direction are somewhat smoother than those in the along-track direction. The smoother wave structures across the orbital track can be explained by the densely placed tangent points in this direction, as shown in Fig. 4.3 (a). However, only a limited number of measurements can be used to derive atmospheric variations in the along-track direction. In this 'sweep mode A', the tangent points are placed at a distance of $\sim$100 km along the orbital track. This means in the along-track direction only GWs with a projected horizontal wavelength larger than 200 km can be observed by 'sweep mode A'. Furthermore, there exists an asymmetry between the across- and along-track extent in the resolved wave structures, as shown in Fig. 4.4. The resolved waves have a much larger spatial coverage in the across-track direction ($\sim$ 2000 km) than in the along-track direction ($\sim$ 500 km).

In general, ‘sweep mode A’ is capable to provide observations of 3-D atmospheric structures. However, the improvement of this observation mode in resolving across-track atmospheric variations is enhanced at the cost of spatial resolution and extent in the along-track direction. In other words, this ‘sweep mode A’ is more sensitive to GWs propagating perpendicularly to the orbital track than to GWs propagating along the orbital track.

4.2 ‘Sweep mode B’ observation strategy

In this section, we propose another sweeping strategy, called ‘sweep mode B’, for satellite-borne limb sounders to capture 3-D GW structures in the MLT. The aim of this ‘sweep mode B’ is to enhance the across-track resolution that typical limb sounders can achieve, while at the same time retaining the good along-track resolution they have. Ideally, GWs with various propagation directions can be captured by this proposed observation mode.

The idea of ‘sweep mode B’ is to sweep the instrument’s LOS horizontally across the orbital track during the flight, as shown in Fig. 4.6. The instrument will stop sweeping at some point, and keep on measuring the emission with a constant viewing azimuth angle. Under this circumstance, vertical slices that reveal the projections of GWs can be observed in the direction along- and across the orbital track, separately. The 3-D wave vector is then able to be reproduced by combining the 2-D wave projections in the two directions. The observation geometry of this mode is introduced in Sect. 4.2.1 in more detail. In Sect. 4.2.2, a case study for ‘sweep mode B’ using simulated measurements is presented. The achievable horizontal resolution and extent, as well as the unbiased estimation of the real horizontal wavelength of a wave from this observation mode is analyzed in Sect. 4.2.3.

4.2.1 Observation geometry of ‘sweep mode B’

For ‘sweep mode B’, a slew rate of $\sim$10 deg/sec provided by the envisaged attitude control system is sufficient for the purpose of sampling the vertical atmospheric profiles across the orbital track. Fig. 4.7 illustrates the orbital track, flight direction, satellite positions and corresponding tangent points for the conventional limb mode and ‘sweep mode B’, respectively. The satellite positions are represented by green dots, and corres-

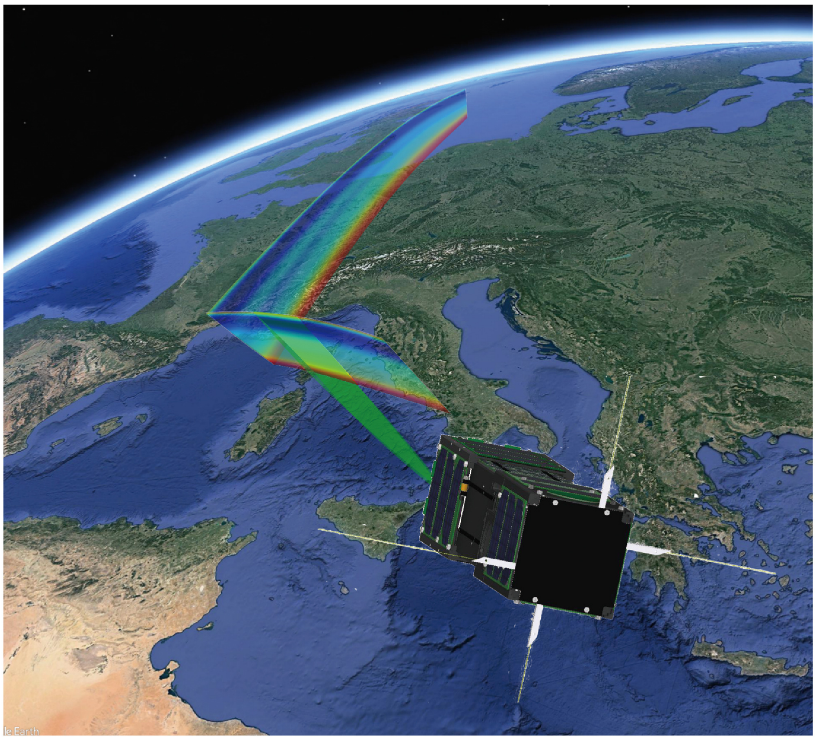

Figure 4.6: Concept of a satellite operated in 'sweep mode B'. The two slices represent the atmospheric temperature structures in the along- and across-track directions.

ponding tangent points are represented by red triangles. The flight direction is indicated by the blue arrows along the orbital track, and an example of the LOS is indicated by the black arrow. The viewing azimuth angle is a constant value for the conventional limb mode, e.g. 90° as shown in Fig. 4.7 (a). The viewing azimuth angle for 'sweep mode B' needs to be adjusted in a way such that the two vertical slices are exactly perpendicular to each other. Fig. 4.7 (b) shows an example of 'sweep mode B' with the viewing azimuth angle of the instrument increasing from 10° to 90° in the region marked by the purple-dashed rectangular box. Instead of forming a 3-D volume, the tangent points in this region are dispersed in two orthogonal planes. This makes it different from 'sweep mode A', where tangent points have a centralized distribution and a 3-D tomographic retrieval can be applied. To solve this problem, a 2-D retrieval scheme is used in 'sweep mode B' to resolve small-scale atmospheric structures in the direction along- and across the orbital track separately. Consequently, 3-D wave structures can be reproduced by combining the 2-D wave vectors obtained in the two directions mentioned above.

Figure 4.8 shows an example of the 3-D ray tracing for the 'sweep mode B' observa-

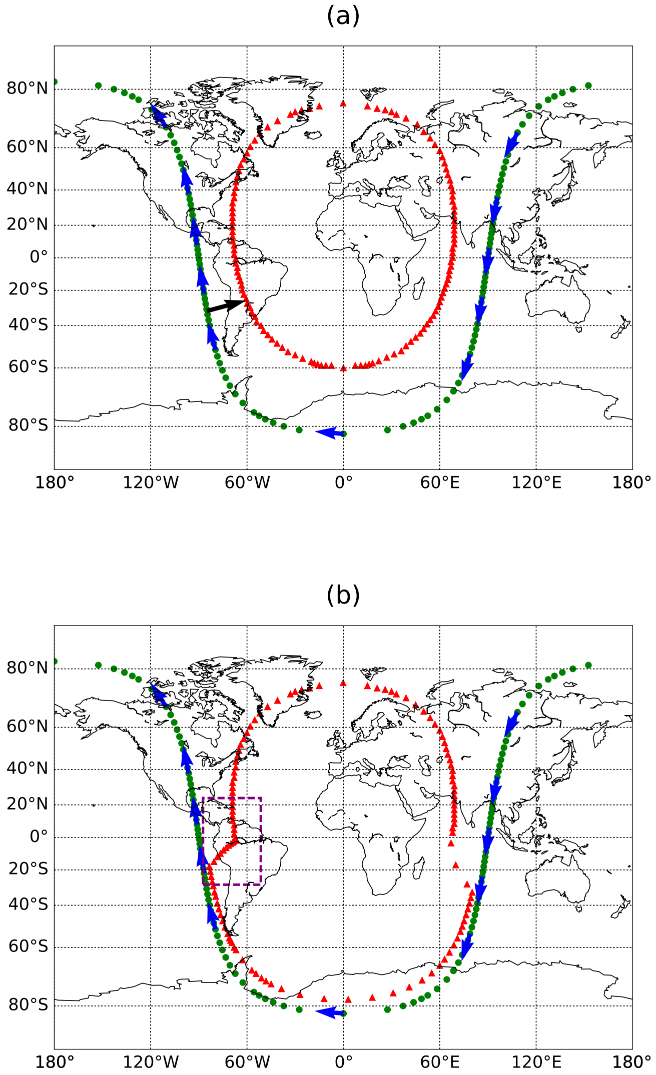

Figure 4.7: Global observation geometry of an exemplary orbit of (a) conventional limb sounding and (b) ‘sweep mode’ limb sounding. The satellite is operated in an orbit at an altitude of 600 km and inclination of 98°. Satellite positions are sampled by green dots and corresponding tangent points by red triangles. The flight direction of the satellite is shown by blue arrows. The viewing angle in panel (a) is perpendicular to the flight direction, shown as the black arrow. In panel (b), the viewing angle changes from 10° to 90° in the ascending orbit, and decreases back to 10° in the descending orbit.

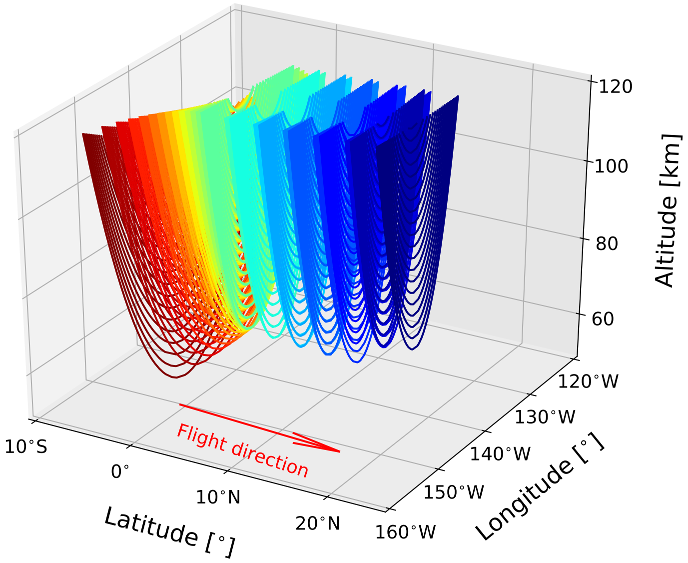

Figure 4.8: Example of 3-D ray tracing for the ‘sweep mode’ observations. The red arrow indicates the flight direction of the satellite. Note that the envisaged instrument has a much denser sampling rate, i.e. a horizontal sampling rate of 6 s per profile and a vertical sampling interval of 1.5 km.

tions at the altitude between 60 and 120 km. The actual sampling rate of the instrument, which is 6 s per profile and 1.5 km vertically, is much denser than that depicted in Fig. 4.8. This ‘sweep mode’ starts with a LOS nearly parallel to the flight direction (shown as dark-red curves) and switches to a LOS perpendicular to the flight direction (shown as dark-blue curves) by gradually adjusting the viewing direction of the instrument during the flight.

4.2.2 Case study of a GW retrieval

In this section, we use an example to show an end-to-end simulation of the ‘sweep mode B’ tomographic observations. The capability of resolving 3-D wave structures by combining the projected 2-D wave slices are explored. In this case study, we only use limb measurements above 87 km for the examination of this observation strategy. Above this altitude, the O_2 A-band emission is assumed to be optically thin, and this significantly reduces the computational cost of this simulation. The parameters relevant for the observation geometry and atmospheric conditions are introduced in Sect. 4.2.2.1 and Sect. 4.2.2.2, respectively.

4.2.2.1 Observation geometry setup

The instrument’s LOS operated in the ‘sweep mode B’ is illustrated in Fig. 4.9. In this example, the instrument increases its viewing azimuth angle from 0° towards a turning angle of 45°. It is initiated with a viewing angle of $\alpha_0 = 0^\circ$ and a slew rate of $\omega = \omega_0$ at $t_0 = 0$ sec. This slew rate slows down gradually such that the tangent points for each imaging are arranged perpendicular to the orbital track. The viewing azimuth angle yielding to this pattern is plotted in Fig. 4.10 and can be described by the following expression:

$$\alpha_t = \arccos\left(\frac{L - \upsilon t}{L}\right) \tag{4.1}$$

where L is the distance between the tangent point and the satellite position, υ is the speed of the satellite, and α_t is the viewing azimuth angle at time t.

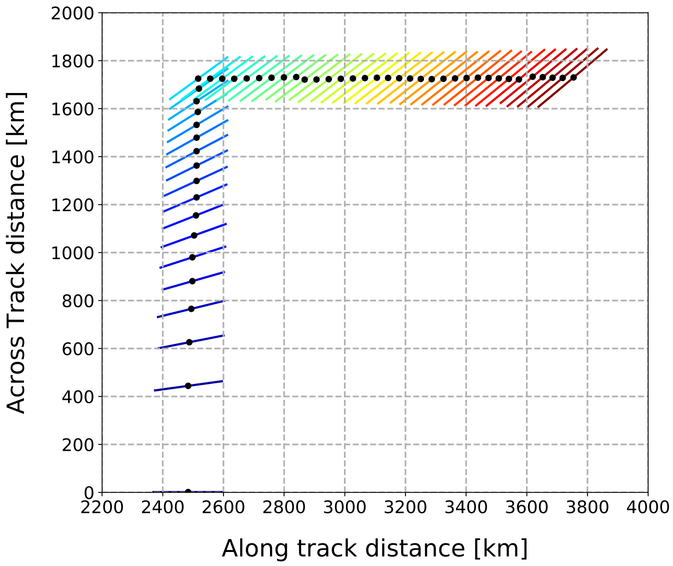

Figure 4.9: Illustration of the ‘sweep mode B’ central measurement track. Flight direction is to the right, 0° viewing direction is to the right as well. For a single measurement, the LOS that targets at 90 km tangent altitude is traced. The solid lines indicate the LOSs within a 1 km vertical layer above the tangent point. The locations of corresponding tangent points are represented by black circles.

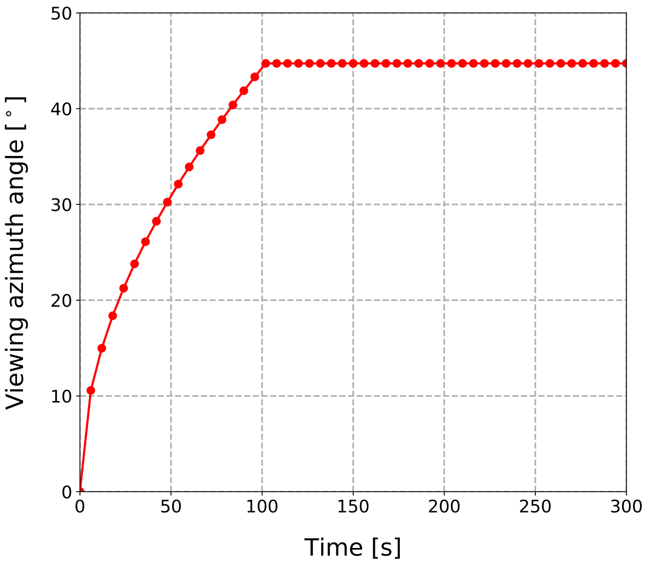

Figure 4.10: Viewing azimuth angle variations of simulated 'sweep mode B' measurements.

4.2.2.2 Setup of atmospheric conditions

In this simulation, the forward model calculates the limb radiance in a 3-D volume at tangent altitudes between 87 and 110 km on a 250 m vertical grid. The vertical sampling for individual limb measurements is 1.5 km. In the horizontal direction, the spacing of the along- and across-track grid is 5 km. In the retrieval model, the temperature fields are estimated on two 2-D planes: one in the across-track direction and another in the along-track direction. In each 2-D retrieval plane, the vertical spacing is 500 m and the horizontal spacing is 12.5 km.

Figure 4.11 shows the simulated 'real atmosphere' for the region of interest at altitudes between 85 and 110 km. The 3-D atmospheric volume in the region between 2000 and 4300 km along the orbital track and between 200 and 2200 km across the orbital track is taken from the HAMMONIA model run for 4° S to 19° N and 134° W to 154° W. This background atmosphere is perturbed by a simulated GW with a vertical wavelength of 15 km and a horizontal wavelength of 310 km tilted at an angle of 38.6° with respect to the orbital track. This propagating geometry results in a projected horizontal wavelength of 400 km and 500 km in the along- and across-track direction, respectively. The wave induces a temperature perturbation of 10 K on the background atmosphere, as shown in Fig. 4.11.

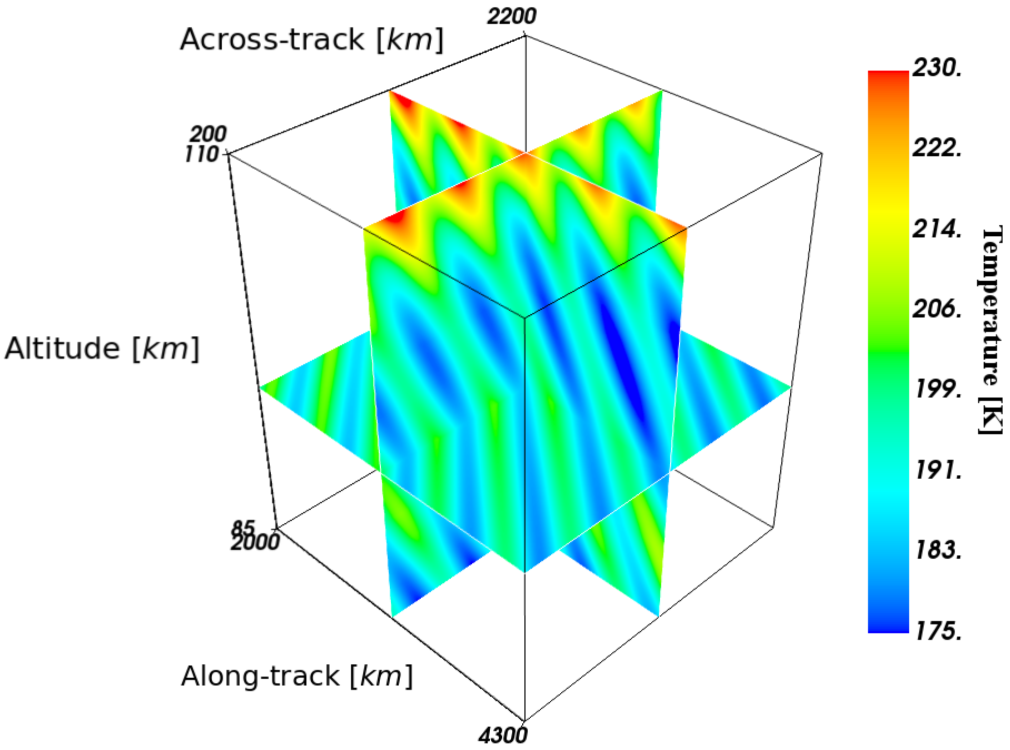

Figure 4.11: 3-D atmospheric temperature fields perturbed by a simulated GW. The background atmosphere is taken from the HAMMONIA model run for 4° S to 19° N and 134° W to 154° W. This simulated wave has a vertical wavelength of 15 km and a horizontal wavelength of 310 km while inducing a 10 K perturbation on the background atmosphere. This wave propagates at a tilting angle of 38.6 ° with respect to the orbital track.

4.2.2.3 Retrieval simulations

This section describes the implementation of the presented principles of ‘sweep mode B’ tomographic reconstruction in the numerical model. In this simulation, we examined the retrieval results by analyzing the extracted wave amplitude and wavelengths, with special attention paid to how well the horizontal wavelengths can be reproduced along the given directions.

To illustrate the performance of the new observation mode, we perturbed a background atmosphere with a GW, as shown in Fig. 4.11. The left panels in Fig. 4.12 represent the corresponding 2-D slices extracted from the 3-D atmosphere in the across-track direction. The a priori data, which is assumed to be the same as the background data, is depicted Fig. 4.12 (a). A GW induced temperature perturbation with an amp-

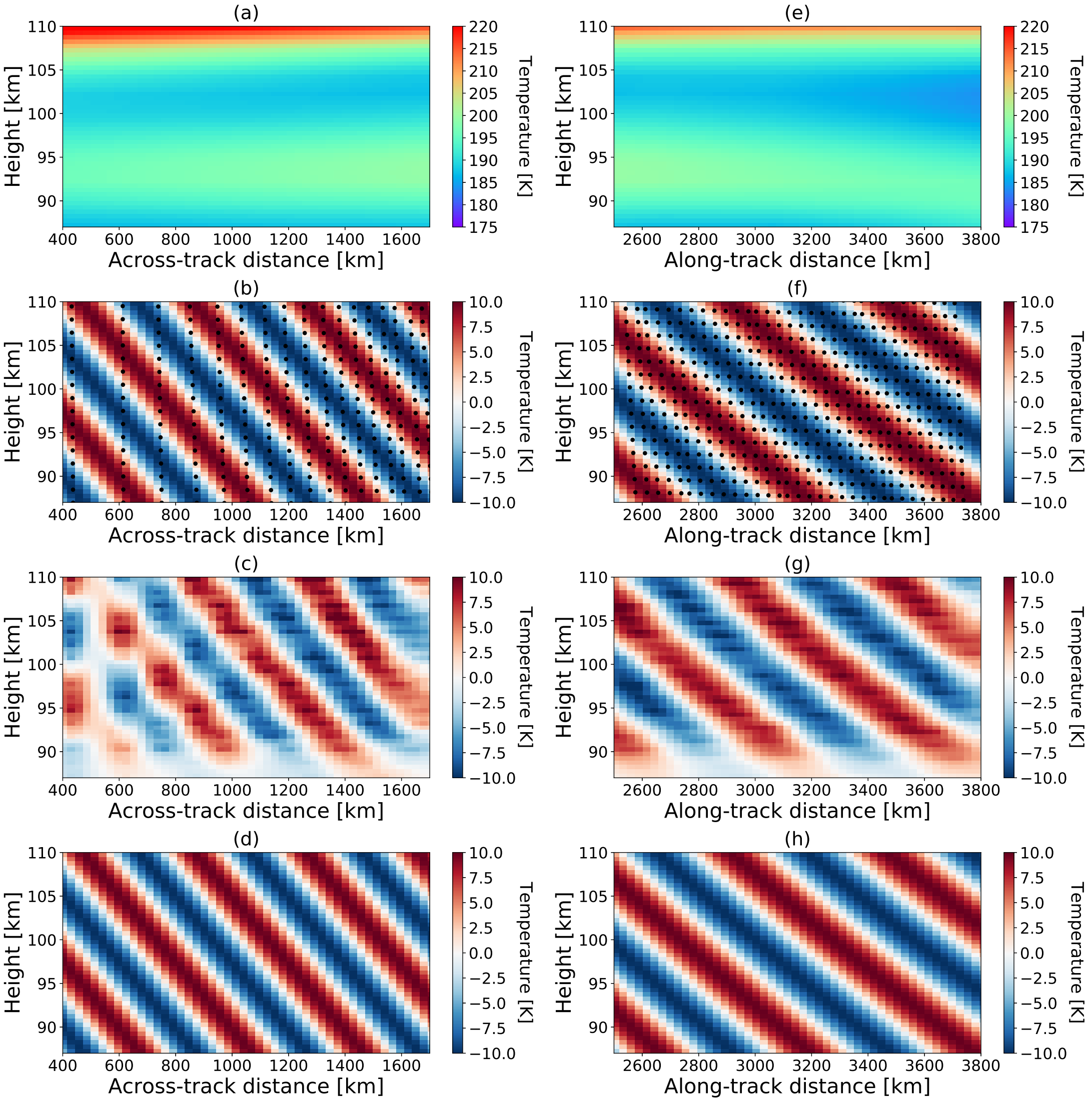

Figure 4.12: Example of 'sweep mode' tomographic retrieval results using simulated data. The panels in the left hand side (a-d) are 2-D slices extracted from the 3-D atmospheric volume in the across-track direction, while those in the right hand side (e-h) are extracted from the along-track direction. The panels in the first row (a and e) depict the a priori atmosphere. The panels in the second row (b and f) show the simulated wave structures from the perturbed 3-D atmospheric temperature field, along with the tangent points from individual measurements marked as black dots. The panels in the third row (c and g) show the wave structures obtained from the retrieval results. The panels in the last row (d and h) depict the optimized wave structures after best-fit processing.

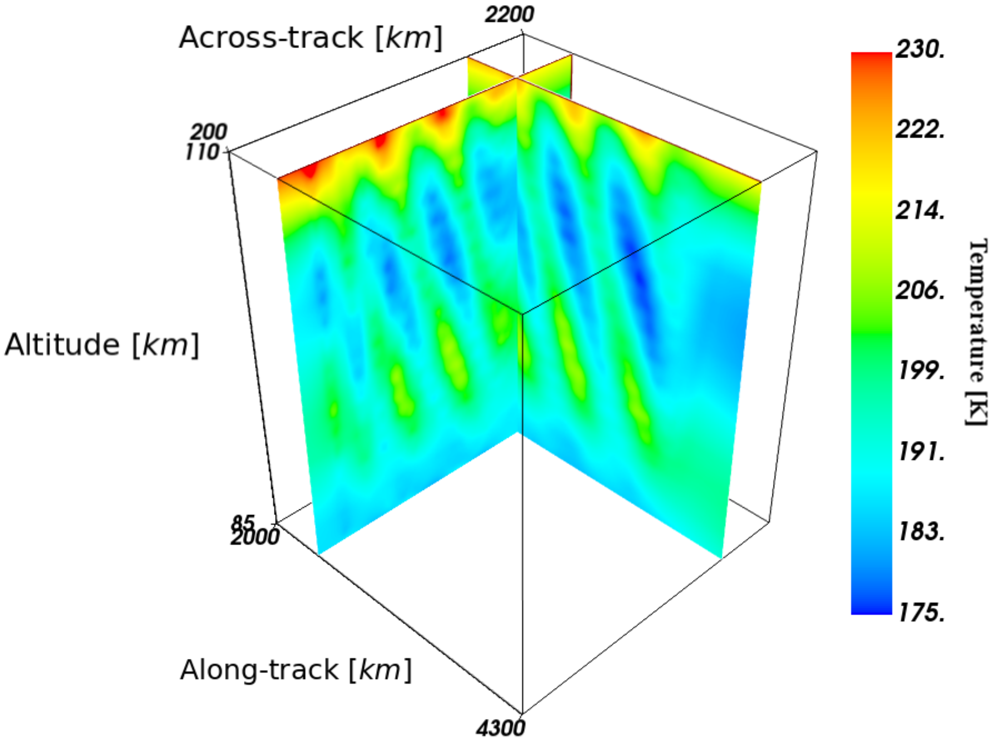

Figure 4.13: 3-D atmospheric temperature fields reconstructed from the along- and across-track retrieval results.

litude of 10 K is depicted in Fig. 4.12 (b). The locations of the tangent points from corresponding measurements are marked as black dots. As we can see, the tangent points have a smaller horizontal sampling distance in the region further apart from the orbital track. The temperature perturbation obtained from the retrieval result is shown in Fig. 4.12 (c). It is obvious that the retrieved wave has a smoother-looking wave pattern in the part with longer across-track distance, due to a denser horizontal sampling rate in this direction. To deduce the wavelength and amplitude of the retrieved GW, all atmospheric points are fitted against the modulated waves using a least-square best fit. In order to obtain optimal values, the vertical and horizontal wavelengths of the fitted sine wave are sampled at an interval of 0.1 km, and the amplitude is set as a free parameter for the best-fit calculating. After this best-fit processing, an optimized wave with a vertical wavelength of 15.2 km, an across-track wavelength of 396.6 km and an amplitude of 8.2 K is obtained, as shown in Fig. 4.12 (d). In contrast, the panels in the right side show the 2-D along-track slices of the background atmosphere, simulated, retrieved and fitted wave structures, respectively. From Fig. 4.12 (f), one can clearly see consecutive measurements with a constant horizontal sampling rate in that direction.

This results in a smooth retrieved wave structure over the entire region of interest, as shown in Fig. 4.12 (g). The optimized wave has a vertical wavelength of 15.1 km, an along-track wavelength of 498.2 km and an amplitude of 8.3 K. Fig. 4.13 shows the 3-D temperature fields reconstructed from the along- and across-track retrieval results.

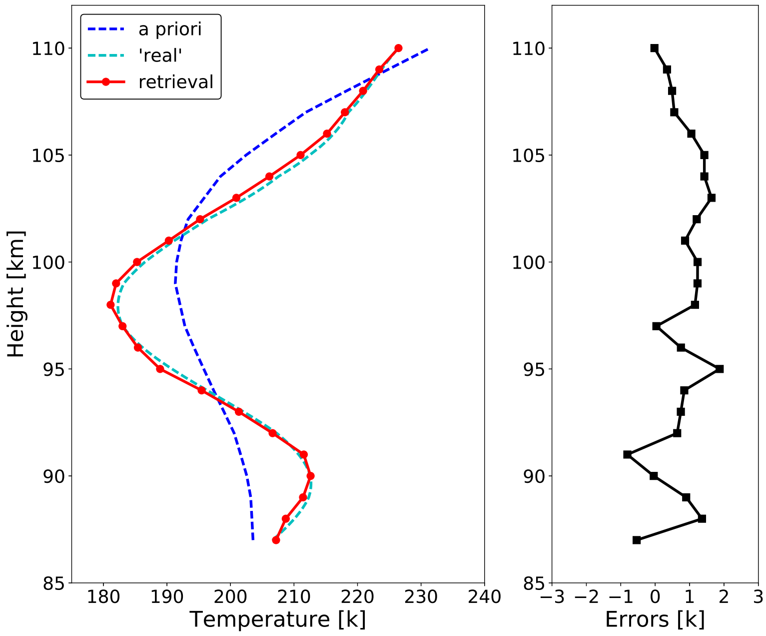

Figure 4.14: Vertical profile of retrieved temperature (left) and total deviation from the expected profile including all error sources (right).

Figure 4.14 shows a vertical profile of retrieved temperature and total deviation from the expected profile including the following error sources: the gridding error, the smoothing error, and, as the largest contribution, the measurement noise. The temperature is retrieved with a precision better than 2 K within this altitude range.

The spatial response of the retrieval result is characterized by the averaging kernel matrix **A**. Fig. 4.15 shows a row of the averaging kernel matrix after mapped into a 2-D space according to the vertical and horizontal coordinates. The spatial resolution of the retrieved data point is estimated by calculating the FWHM of the row of the averaging kernel matrix along the vertical and horizontal directions, respectively. In Fig. 4.15, panel (a) shows the averaging kernel of the retrieval in across-track direction for a tangent point located at 96 km vertically and 1600 km across track. The estimated resolution is about 1.2 km in the vertical and 95 km in the horizontal direction. The averaging kernel for a tangent point in the along-tack direction is shown in panel (b) at the position of 96 km vertically and 3200 km along track. The estimated resolution is about 1.2 km in the vertical and 80 km in the horizontal direction.

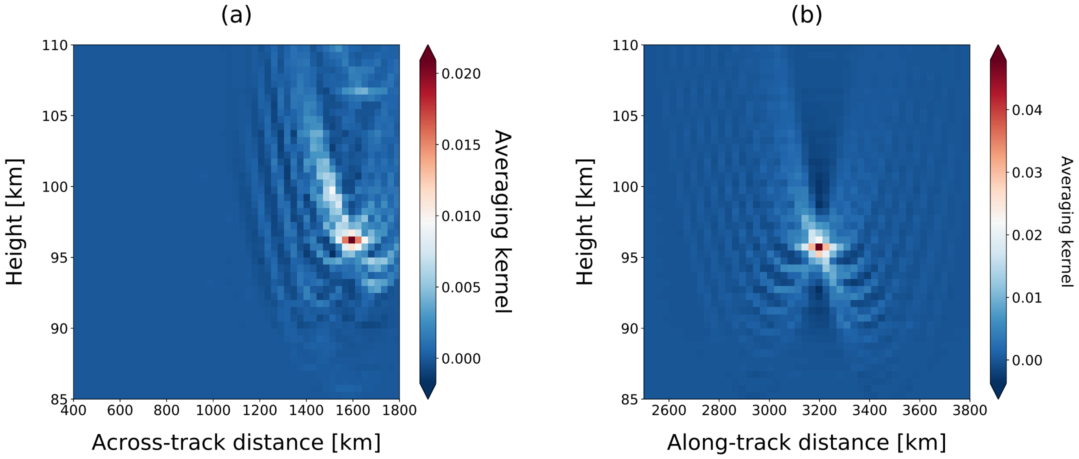

Figure 4.15: Averaging kernel matrix for retrieval points in the across-track slice (a) and along-track slice (b). Figure (a) is for the point located at 96 km vertically and 1600 km across track, and Figure (b) is for the points locating 96 km vertically and 3200 km along track.

4.2.3 Horizontal wavelength analysis

GW momentum flux can be estimated from temperature measurements. Based on GW polarization relations, *Ern et al.* (2004) relate the momentum flux of GW to the retrieved temperature amplitude and vertical and horizontal wavelengths. Considering a medium-frequency wave ($N' \gg \hat{\omega} \gg f$), the GW momentum flux is given by

$$F = \frac{1}{2}\,\bar{\rho}\,\frac{k}{m}\left(\frac{g}{N}\right)^2\left(\frac{\hat{T}}{T}\right)^2 \tag{4.2}$$

where g is the gravitational acceleration, N is the buoyancy frequency, $\hat{T}$ and T are the temperature amplitude and background temperature, respectively. $k = 2\pi/\lambda_h$ is the horizontal wavenumber and $m = 2\pi/\lambda_v$ is the vertical wavenumber of the wave. Therefore, the momentum flux of a GW can be determined if the full wave vector and temperature amplitude are able to be retrieved from the measurements. The retrieval approach for deriving the vertical wavelength and amplitude of a GW is well-established, and is therefore not discussed here. In this section, we focus on the assessment of how well the horizontal wave vector can be reproduced from the ‘sweep mode B’ measurements.

4.2.3.1 Along-track horizontal wavelength

In Sect. 4.2.2.3, numerical simulations for the 'sweep mode B' measurements with a specific turning angle of 45° were performed. In practical application, this turning angle α is flexible and can be adjusted between 0° and 90° according to the target area. Here, the performance of the along-track wavelength retrieval in two extreme cases of $\alpha = 0^\circ$ and $\alpha = 90^\circ$ is discussed.

When $\alpha = 90^\circ$, the tangent points for along-track wavelength analysis extend to $\sim$2500 km apart from the orbital plane. For individual measurements, the LOS is perpendicular to the along-track direction in this case. This means all the radiation received by the instrument comes from the atmosphere in the across-track direction. For this viewing geometry, 1-D vertical temperature profiles are retrieved from individual measurements independently. The horizontal wavelength is then estimated by analyzing the phases of adjacent vertical temperature profiles (*Ern et al.*, 2004). In this case, the along-track horizontal wavelength that can be detected is limited by the Nyquist wavelength, which is twice the sampling distance: $\lambda_{h,N} = 2\Delta x_h$. Considering the integration time of $\sim$6 s in this simulation, GWs with horizontal wavelength longer than $\sim$ 85 km in the along-track direction can be detected.

If the turning angle α is smaller than 90°, more information from neighboring atmospheric volume in the along-track direction will contribute to the total radiation received by the instrument. When $\alpha = 0^\circ$, the LOSs of measurements will overlap with each other in the orbital plane. Such an observation strategy allows for the retrieval of GWs in a real 2-D space as described in Sect. 3.2.2. Assuming the same atmospheric condition and viewing geometry, Fig. 3.12 demonstrated that a GW with a horizontal wavelength longer than 150 km can be retrieved if the horizontal sampling distance is assumed to be 70 km. The actual horizontal sampling distance is 40 km in this case, and therefore the shortest horizontal wavelength that can be detected is expected to be $\sim$85 km. Note that the detectable along-track horizontal wavelength in the two cases ($\alpha = 0^\circ$ and $\alpha = 90^\circ$) has a similar limit of $\sim$85 km, but is derived from different approaches. When $\alpha = 90^\circ$, the horizontal wavelength is indirectly deduced from 1-D vertical profiles. However, 2-D wave structures can be better resolved from tomographic retrievals while $\alpha = 0^\circ$. In Fig. 4.16, an example of retrieving a GW with a vertical wavelength of 10 km and horizontal wavelength of 150 km is given. In this example, the atmospheric temperature is retrieved in a finer grid: 500 m in the vertical and 7 km in the along-track direction. The 2-D wave structures along the orbital plane can be observed clearly.

Additionally, the influence of the across-track variations should also be taken into account when the wave is resolved in the along-track direction. As in this case the retrieval assumes a homogeneous atmosphere in the across-track direction, the resolved temperature fields in the along-track direction will be affected by ignoring the across-

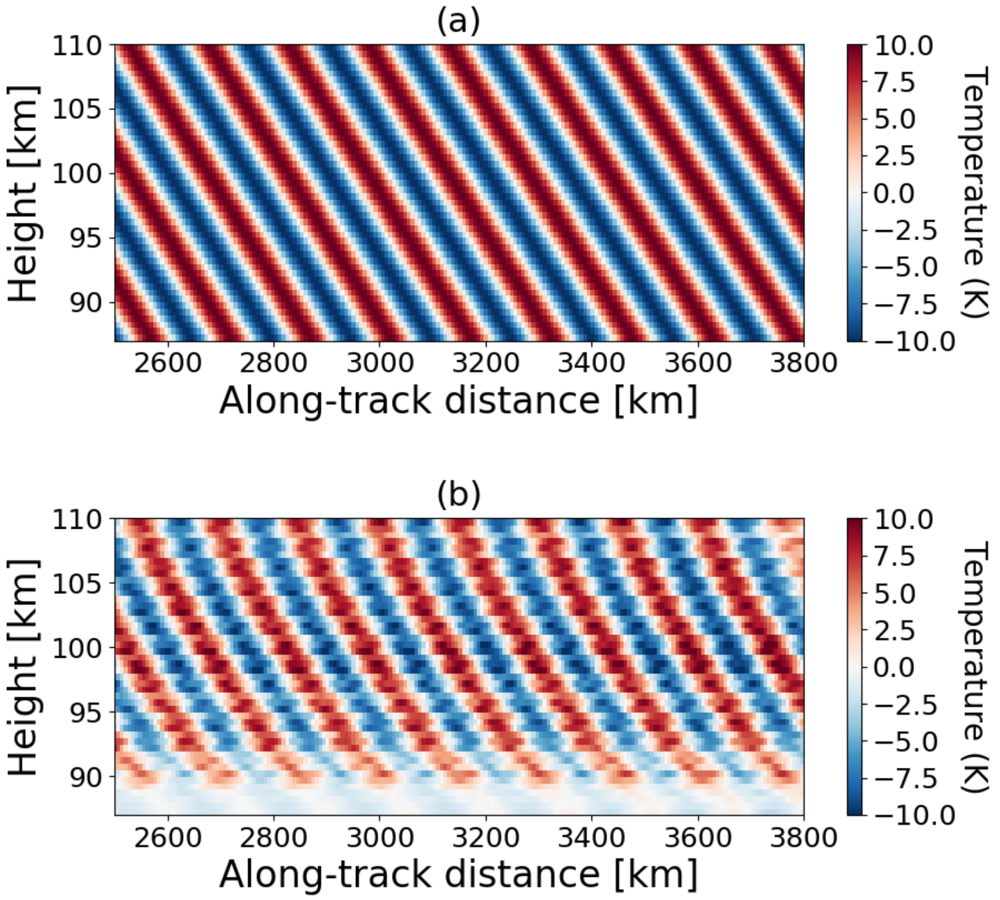

Figure 4.16: Simulated GW (a) with a vertical wavelength of 10 km and horizontal wavelength of 150 km, and retrieved wave structure (b) assuming a turning angle α of 0°.

track variations. For example, a turning angle of 45° and 90° have different weighting functions in the across-track direction. Thus, the reconstructed temperature fields in the along-track direction will differ from each other. In Fig. 4.17, a GW is simulated with a vertical wavelength of 15 km and a horizontal wavelength of 425 km. The wave vector is tilted at an angle of 32° away from the flight direction. Fig. 4.17 (a) and (b) show the reconstructed wave structures in the along-track direction when a turning angle of 45° and 90° are used, respectively. It is obvious that a turning angle of 45° causes a stronger phase shift compared with a turning angle of 90°. Meanwhile, the wave amplitude in Fig. 4.17 (b) is closer to the simulated wave amplitude, which is 10 K. Since in this simulation the wave vector is 32° away from the orbit, a turning angle closer to this wave vector will be affected more by the variations along the LOS. Thus, the wave patterns reconstructed from Fig. 4.17 (b) fits better with the simulated wave.

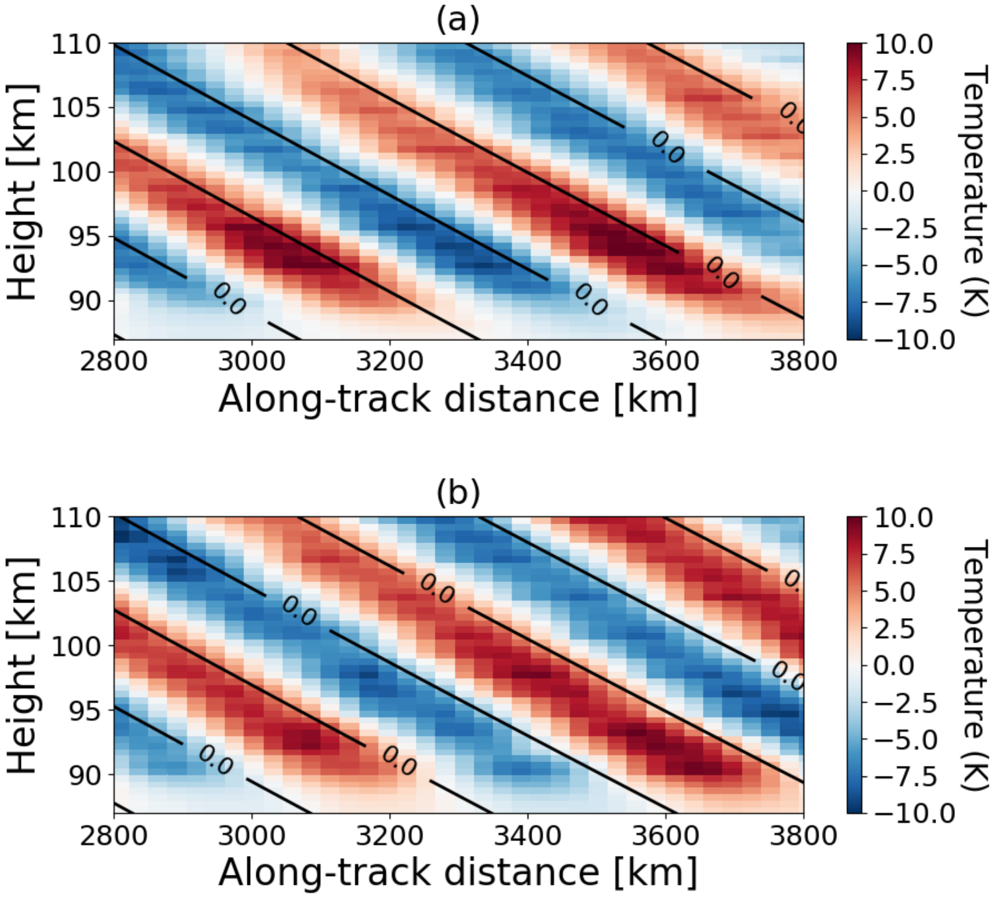

Figure 4.17: Comparison of wave structures retrieved in the along-track direction using a turning angle of 45° (a) and 90° (b). The wave is simulated with a vertical wavelength of 15 km and a horizontal wavelength of 425 km. The wave vector is tilted at an angle of 32° away from the flight direction. The simulated wave amplitude is 10 K. The phase fronts with zero value of the simulated wave are indicated by the black lines.

4.2.3.2 Across-track horizontal wavelength

From the retrieval results in Sect. 4.2.2.3, we can see that the across-track horizontal wavelength retrieval is affected by the turning angle of ‘sweep mode B’ in two aspects. First, the horizontal coverage in the across-track direction is limited by this turning angle. When $\alpha = 45°$, the tangent points from individual limb sounding measurements could extend to ~1700 km apart from the orbital plane. A larger value of this turning angle will increase the across-track distance that the tangent points are able to reach. Second, the across-track horizontal resolution which determines the smallest detectable

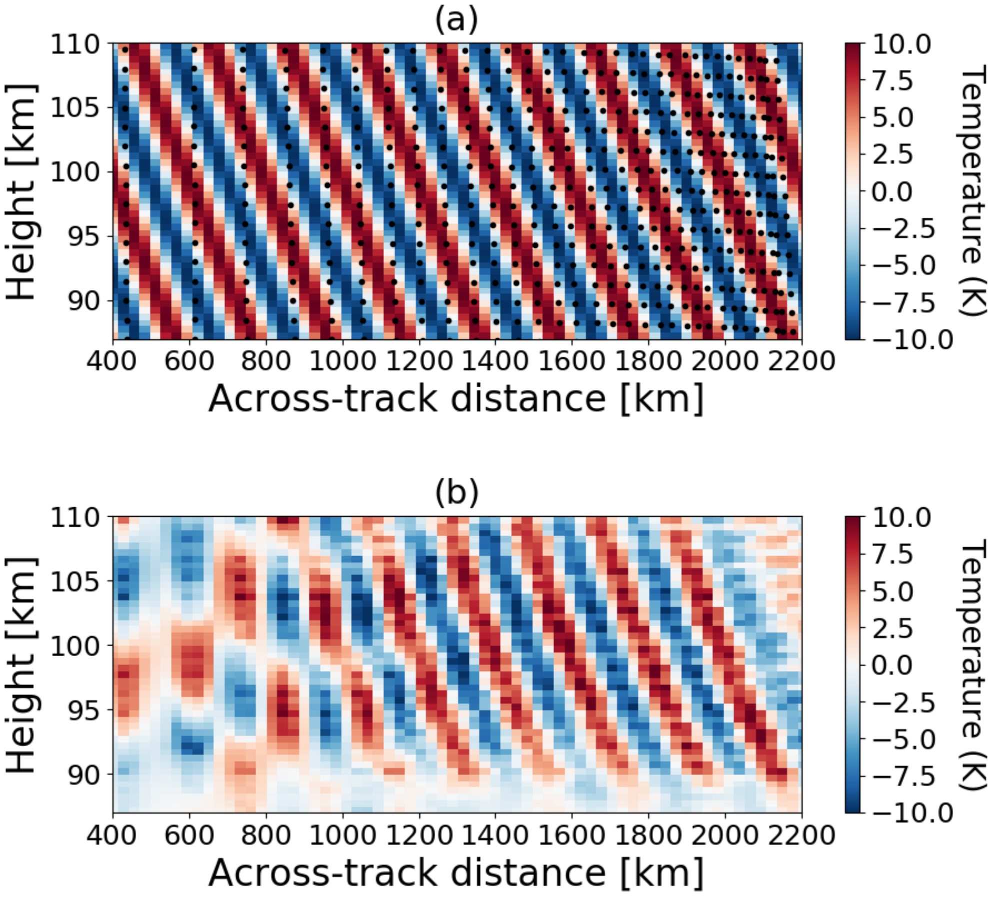

Figure 4.18: Simulated GW (a) with a vertical wavelength of 10 km and horizontal wavelength of 250 km, and retrieved wave structure (b) assuming a turning angle α of 90°. The tangent points from individual measurements are marked as black dots in (a).

wavelength of a wave, is also affected by this turning angle. As the across-track horizontal resolution increases with distance, smaller waves can be observed better in the region further away from the orbit. This means GWs with smaller horizontal wavelengths in the across-track direction can be observed if the satellite is operated in the ‘sweep mode B’ with a larger turning angle.

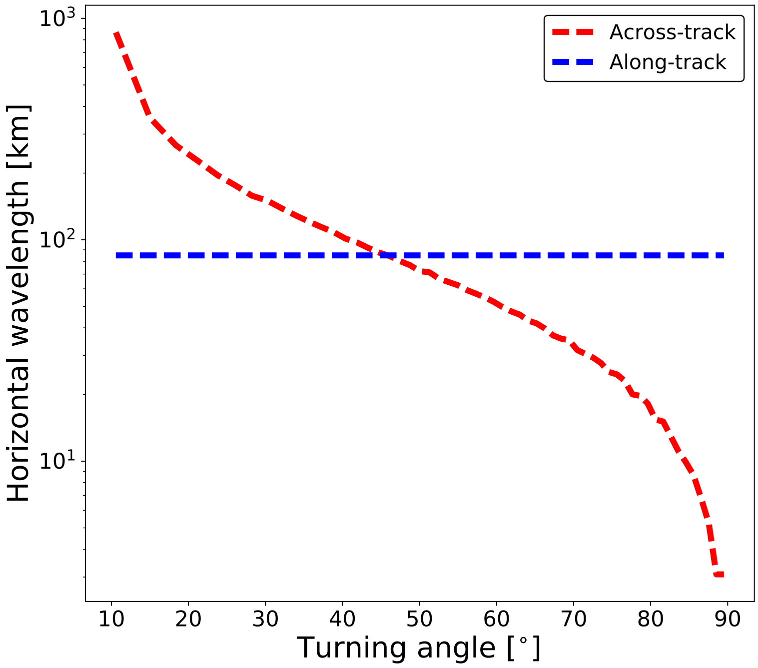

Figure 4.19: Comparison of the ability in resolving horizontal wavelength along the two directions under different turning angles. The blue line represents the minimal detectable horizontal wavelength in the along-track direction, and the red line represents that in the across-track direction.

Figure 4.18 shows an example of retrieving a GW in the across-track direction with a turning angle α of 90°. In this example, the horizontal coverage in the across-track direction extends to 2200 km because a large value of α is selected. Between ∼400-1000 km in the across-track direction, the wave structure can barely be seen as the sampling distance is relatively coarse (∼200 km). In the region close to ∼2200 km the tangent points are densely distributed in the across-track direction, and therefore GWs with a small horizontal wavelength can be resolved.

Based on the discussion above, Fig. 4.19 shows the ability of ‘sweep mode B’ to resolve horizontal wavelengths for different turning angles. In the along-track direction, the smallest horizontal wavelength that can be resolved is constant (∼85 km) because the sampling distance in this direction is independent of the turning angle. In the across-track direction, the resolvable horizontal wavelength is ∼850 km at a turning angle of 10°. GWs with a smaller across-track horizontal wavelength can be resolved if a larger turning angle is adopted. When the turning angle is 45°, the resolvable horizontal wavelength in both directions reaches the same limit of ∼85 km. This sensitivity curve is obtained based on the simulation of idealized atmosphere and observation. In practical application, it will be limited by measurement noise and other inaccuracies.

4.2.3.3 Estimation of real horizontal wavelength

From conventional limb sounding measurements, the resolved horizontal wavelength is the apparent wavelength projected along the orbital track. This projected horizontal wavelength is generally larger than the real wavelength of a wave, details see in Sect. 3.3.3. Utilizing this ‘sweep mode B’ observation strategy, projected wavelengths can be retrieved along- and across the orbital track in two independent slices. This re-

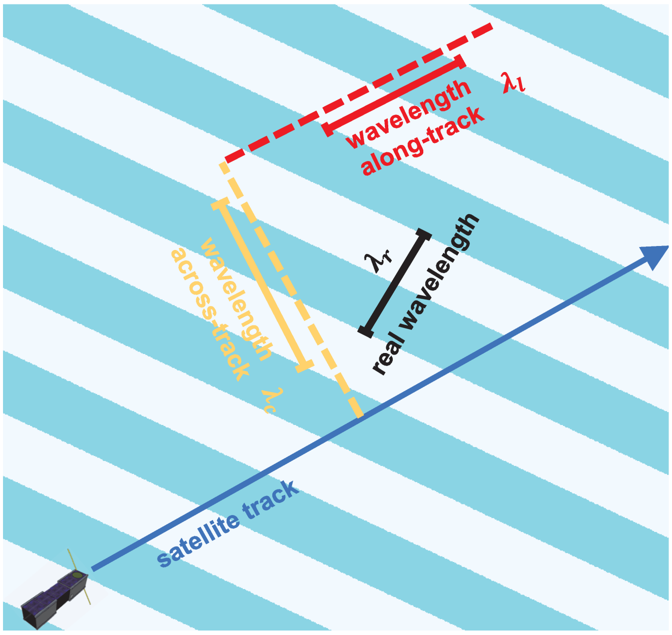

Figure 4.20: Schematic drawing of observed horizontal wavelength in the ‘sweep mode B’ observation. The wave fronts of the GW are indicated by the light-blue shading. The satellite track is represented by the dark-blue arrow. The retrieved horizontal wavelengths in the along- and across-track directions are represented by yellow and red bars, respectively. The real horizontal wavelength is represented by the black bar.

trieval scheme will reduce the bias for the estimation of the real wavelength of a wave. The relationship between the retrieved horizontal wavelengths and the real wavelength is shown in Fig. 4.20. The satellite track is represented by the dark-blue arrow. The wave fronts of the GW are indicated by the light-blue shading. The retrieved horizontal wavelength in the along-track direction (λ_l) is represented by the red bar, and that in the across-track direction (λ_c) is represented by the yellow bar. However, the real horizontal wavelength of this simulated wave is the one that is represented by the black bar. In any case, the real horizontal wavelength of a wave can be derived by combining the horizontal wavelengths retrieved in the two directions perpendicular to each other. The main advantage of this observation mode is that the accuracy of retrieved horizontal wavelengths is independent of the angle between the satellite track and horizontal wave vector. Following a geometric transformation, an unbiased horizontal wavelength estimation can be obtained using this equation:

$$\lambda_r = \frac{\lambda_l \, \lambda_c}{\sqrt{\lambda_l^2 + \lambda_c^2}} \tag{4.3}$$

4.3 Chapter summary

In this chapter, two sweep modes, namely the 'sweep mode A' and the 'sweep mode B', are proposed for the reconstruction of 3-D atmospheric structures in the MLT region. The proposed sweep modes are applicable to satellite-borne limb sounders measuring airglow emissions in the atmosphere, including both layered and non-layered emissions. In this study, the sweep modes are simulated for an instrument that detects the atmospheric temperature from the measurements of the O_2 A-band airglow emissions.

The idea of the sweep modes is to horizontally sweep the instrument's LOS such that the volume of interest can be observed from multiple directions. The 'sweep mode A' is a combination of limb measurements from forward-, backward-, and side-looking. The tangent points of consecutive measurements form a 3-D volume in the region of interest, and therefore a 3-D tomography method can be applied to retrieve the atmospheric structures in this region. It has been demonstrated in a case study of GW retrieval that the orientation of a wave can be resolved from the 'sweep mode A'. The retrieval results also show that the 'sweep mode A' is more sensitive to GWs propagating perpendicularly to the orbital track. However, this observation mode has limited spatial resolution ($\sim$100 km) and extent ($\sim$400 km) in the direction along the orbital track.

Another observation strategy, called 'sweep mode B', is proposed by employing a different strategy in sweeping the instrument's LOS. The sweeping strategy of this observation mode ensures the tangent points from consecutive measurements are placed either along- or across the orbital track. Instead of forming a 3-D volume as in ‘sweep mode A’, the tangent points of ‘sweep mode B’ are dispersed in two orthogonal planes. Therefore, a pseudo 3-D tomographic reconstruction technique, which consists of two separate 2-D tomographic retrievals, is applied to resolve 3-D atmospheric structures exclusively for this observation geometry. The first step of this technique is to retrieve 2-D wave structures in the direction along- and across the orbital track separately. In the second step, the 3-D wave structures are reconstructed by combining the projected 2-D waves in two orthogonal planes. A case study of GW retrieval has shown that the spatial resolution and extent of the retrieved waves are influenced by the turning angle of this observation. In general, this pseudo 3-D tomographic reconstruction technique is independent of the angle between the orbital track and the wave fronts. It can be used to provide an unbiased estimation of the real horizontal wavelength of GWs, which is an important parameter for the calculation of GW momentum flux.

Chapter 5

Summary and outlook

The main objective of this work is the development of a tomographic reconstruction technique to derive GW parameters from satellite-borne multi-angle airglow observations. This study is based on an envisaged satellite-borne remote sensing instrument measuring the O_2 A-band airglow emissions near 762 nm. The rotational structure of the observed airglow emission is used to derive the atmospheric temperature in the MLT region. The GW parameters are quantified according to the temperature perturbations they induce on the background atmosphere. In this thesis, the forward model that simulates the spectral radiance received by the instrument was presented. It includes an O_2 A-band airglow emission model, a fast 3-D ray tracing, a GW perturbation calculation and the corresponding radiative transfer equations. A tailored retrieval scheme that is capable of deriving 3-D atmospheric temperature fields from the proposed airglow observations was introduced. Two types of observation strategies, namely the 'target mode' and the 'sweep mode', have been presented in view of their ability in resolving small-scale GW parameters.

The 'target mode' combines limb and sub-limb measurements for improving the spatial resolution that conventional limb sounders can achieve. In particular, this mode provides access to a part of the GW spectrum which is not accessible by conventional limb soundings. Conventional limb soundings are capable of deriving small-scale vertical structures of GWs because of their high vertical resolution. However, the horizontal wave structures they can observe are very limited due to the long horizontal sampling distance of the instrument and the long horizontal weighting function along the instrument's LOS. Studies show that limb sounders with an integration time of 10 s can resolve GWs with vertical and horizontal wavelength down to 7 km and 150 km in the mesopause region. The basic idea of the proposed 'target mode' is the use of sub-limb measurements to provide additional information on the horizontal structure of the atmospheric volume under investigation. The viewing geometry of this 'target mode' was simulated and analyzed in comparison to conventional limb measurements. The retrieval results show that a combination of limb and sub-limb measurements shifts the sensitivity to detect GWs by 50-100 km towards short horizontal wavelengths. Another advantage of this ‘target mode’ is that it reduces the phase shift effects that exist in the limb sounding retrieval results. However, an existing problem of this ‘target mode’ is that only the projection of the wave vector onto the instrument’s LOS can be resolved, which is enlarged by the the cosine of the angle between the wave vector and the instrument’s LOS. If the propagation direction of a wave is unknown, the real horizontal wavelength of the resolved wave can be biased.

To derive direction-resolved momentum flux and to initialize gravity wave ray-tracing simulations, a 3-D GW vector is needed. Therefore, a second type of observation strategy is proposed for the reconstruction of 3-D GW structures in the MLT region. This observation strategy consists of two different modes, namely the ‘sweep mode A’ and the ‘sweep mode B’. The proposed sweep modes are applicable to satellite-borne limb sounders measuring airglow emissions in the atmosphere, including both layered and non-layered emissions. The basic idea of the sweep modes is to horizontally sweep the instrument’s LOS in a way that the volume of interest can be observed from multiple directions. This can be done by adjusting the viewing azimuth angle of the instrument under a specific slew rate. The ‘sweep mode A’ is a combination of limb measurements from forward-, backward-, and side-looking. For this observation mode, a 3-D tomography method can be used to retrieve atmospheric structures in the region of interest. However, the ‘sweep mode A’ is more sensitive to waves propagating perpendicularly to the flight direction than waves along the flight direction. The ‘sweep mode B’ has a different strategy in sweeping the instrument’s LOS. It ensures that the tangent points are dispersed in two orthogonal planes, either along- or across the orbital track. The ‘sweep mode B’ uses a pseudo 3-D tomographic reconstruction technique to resolve small-scale wave structures. Utilizing this technique, a full 3-D wave vector can be reproduced indirectly by combining the 2-D wave projections that are retrieved in the along- and across-track directions. Therefore an unbiased estimation of the real horizontal wavelength of a wave can be obtained, thus reducing the errors in deducing GW momentum flux substantially.

A nano-satellite mission called ‘AtmoCube-1’ is under preparation to demonstrate these measurement modes in reality.

Appendix A

A.1 Line parameters of O_2 A-band

Table A.1: Line parameters of O_2 A-band in the 2016 edition of HITRAN (*Gordon et al.*, 2017)

Wavenumber cm^{-1}	Einstein A coefficient s^{-1}	Lower state energy cm^{-1}	Upper state degeneracy
13001.70951	2.19E-02	1246.4486	57
13002.18632	2.98E-07	1245.9718	57
13010.81234	2.31E-02	1085.2033	53
13012.58246	2.20E-02	1083.4332	53
13013.02394	3.00E-07	1082.9917	53
13014.29578	7.62E-08	260.6824	21
13021.29083	2.32E-02	933.5309	49
13023.07859	2.20E-02	931.7431	49
13023.48451	3.02E-07	931.3372	49
13031.39409	2.33E-02	793.2087	45
13033.19968	2.20E-02	791.4031	45
13033.2948	8.05E-08	188.8531	17
13033.56974	3.06E-07	791.0331	45
13041.12364	2.35E-02	664.2595	41
13042.94727	2.21E-02	662.4359	41
13043.28109	3.08E-07	662.102	41
13050.48076	2.37E-02	546.7042	37
13051.93672	8.75E-08	128.492	13
13052.32274	2.21E-02	544.8622	37

13052.61983	3.12E-07	544.5651	37
13059.46653	2.39E-02	440.5618	33
13061.32727	2.21E-02	438.701	33
13061.58694	3.16E-07	438.4413	33
13068.08182	2.42E-02	345.8495	29
13069.9619	2.22E-02	343.9694	29
13070.1832	3.21E-07	343.7481	29
13070.22159	9.95E-08	79.607	9
13076.32729	2.45E-02	262.5827	25
13078.22755	2.22E-02	260.6824	25
13078.4091	3.27E-07	260.5009	25
13084.20339	2.51E-02	190.7748	21
13086.12514	2.23E-02	188.8531	21
13086.26482	3.35E-07	188.7134	21
13088.15293	1.29E-07	42.2001	5
13091.71036	2.58E-02	130.4375	17
13093.65584	2.24E-02	128.492	17
13093.75013	3.45E-07	128.3977	17
13098.84825	2.70E-02	81.5805	13
13100.82175	2.26E-02	79.607	13
13100.86414	3.62E-07	79.5646	13
13105.61687	2.93E-02	44.2117	9
13105.75288	3.46E-07	16.2529	1
13107.60461	3.92E-07	42.224	9
13107.62847	2.29E-02	42.2001	9
13112.01587	3.51E-02	18.3372	5
13113.96544	4.65E-07	16.3876	5
13114.10019	2.36E-02	16.2529	5
13118.04466	8.78E-02	3.9611	1
13119.92145	1.02E-06	2.0843	1
13126.39197	8.78E-03	3.9611	5
13128.26876	2.03E-02	2.0843	5
13130.35305	2.30E-08	0	5
13131.49141	1.47E-02	18.3372	9
13133.44097	2.11E-02	16.3876	9
13133.57572	1.73E-07	16.2529	9

13136.21704	1.69E-02	44.2117	13
13138.20478	2.13E-02	42.224	13
13138.22863	2.15E-07	42.2001	13
13140.56737	1.81E-02	81.5805	17
13142.54087	2.36E-07	79.607	17
13142.58325	2.15E-02	79.5646	17
13144.54071	1.88E-02	130.4375	21
13146.48618	2.48E-07	128.492	21
13146.58047	2.16E-02	128.3977	21
13147.74429	1.93E-08	2.0843	9
13148.13516	1.93E-02	190.7748	25
13148.41074	2.12E-02	2956.3374	93
13150.05691	2.57E-07	188.8531	25
13150.19659	2.17E-02	188.7134	25
13150.78149	2.18E-02	2953.9666	93
13151.34863	1.97E-02	262.5827	29
13151.75387	2.12E-02	2703.8443	89
13153.24888	2.64E-07	260.6824	29
13153.43044	2.17E-02	260.5009	29
13154.10701	2.18E-02	2701.4912	89
13154.1788	2.00E-02	345.8495	33
13154.65278	2.11E-02	2462.413	85
13156.05888	2.68E-07	343.9694	33
13156.28018	2.17E-02	343.7481	33
13156.62315	2.02E-02	440.5618	37
13156.98831	2.18E-02	2460.0774	85
13157.11317	2.11E-02	2232.0828	81
13158.4839	2.71E-07	438.701	37
13158.67897	2.04E-02	546.7042	41
13158.74357	2.18E-02	438.4413	37
13159.14049	2.11E-02	2012.8914	77
13159.43107	2.18E-02	2229.7649	81
13160.34331	2.05E-02	664.2595	45
13160.52096	2.75E-07	544.8622	41
13160.73995	2.10E-02	1804.8745	73
13160.81804	2.18E-02	544.5651	41

13161.44076	2.18E-02	2010.5911	77
13161.61302	2.06E-02	793.2087	49
13161.91651	2.10E-02	1608.0661	69
13162.16695	2.77E-07	662.4359	45
13162.48473	2.07E-02	933.5309	53
13162.50077	2.18E-02	662.102	45
13162.67489	2.09E-02	1422.4983	65
13162.95486	2.08E-02	1085.2033	57
13163.01959	2.09E-02	1248.2013	61
13163.02256	2.18E-02	1802.5919	73
13163.4186	2.79E-07	791.4031	49
13163.78866	2.18E-02	791.0331	49
13164.04114	3.30E-08	16.3876	13
13164.18144	2.18E-02	1605.8012	69
13164.27249	2.81E-07	931.7431	53
13164.67841	2.18E-02	931.3372	53
13164.72498	2.82E-07	1083.4332	57
13164.77221	2.82E-07	1246.4486	61
13164.9221	2.18E-02	1420.2511	65
13165.16646	2.18E-02	1082.9917	57
13165.24902	2.18E-02	1245.9718	61
13179.92389	4.06E-08	42.224	17

A.2 Rate constants of O_2 A-band volume emission

Table A.2: Rate constants relevant for the production and loss of $O_2(b^1\Sigma)$.

Rate	Value	Reference
g_A	5.94×10^{-9}	(*Christensen et al.*, 2012)
g_B	3.54×10^{-10}	(*Christensen et al.*, 2012)
A_{771}	$0.070\ \mathrm{s}^{-1}$	(*Krupenie*, 1972)
$K_{0\mathrm{B}}$	$4.5 \times 10^{-12}\ \mathrm{cm}^3\mathrm{s}^{-1}$	(*Pejaković et al.*, 2005)
$K_{1\mathrm{B}}$	$4.2 \times 10^{-11}\mathrm{e}^{-312/T}\ \mathrm{cm}^3\mathrm{s}^{-1}$	(*Kalogerakis et al.*, 2002)
$K_{2\mathrm{B}}$	$5 \times 10^{-13}\ \mathrm{cm}^3\mathrm{s}^{-1}$	(*Hwang et al.*, 1999)
$K_{3\mathrm{B}}$	$3 \times 10^{-10}\ \mathrm{cm}^3\mathrm{s}^{-1}$	(*Yankovsky and Manuilova*, 2006)
J_2	See Sect. 2.1.2	-
J_3	See Sect. 2.1.2	-
k_1	$3.3 \times 10^{-11}\mathrm{e}^{55/T}\ \mathrm{cm}^3\mathrm{s}^{-1}$	(*Sander et al.*, 2006)
k_2	$2.15 \times 10^{-11}\mathrm{e}^{110/T}\ \mathrm{cm}^3\mathrm{s}^{-1}$	(*Sander et al.*, 2006)
$A_{1\mathrm{D}}$	$6.83 \times 10^{-3}\ \mathrm{s}^{-1}$	(*Kernahan and Pang*, 1975)
φ	0.95	(*Green et al.*, 2000)
k_5	$4.7 \times 10^{-33}(300/T)^2\ \mathrm{cm}^6\mathrm{s}^{-1}$	(*Campbell and Gray*, 1973)
k_5	$4.7 \times 10^{-33}(300/T)^2\ \mathrm{cm}^6\mathrm{s}^{-1}$	(*Campbell and Gray*, 1973)
$C_{\mathrm{O}_2}[\mathrm{O}_2]$	7.5	(*McDade et al.*, 1986)
$C_{\mathrm{O}}[\mathrm{O}]$	33	(*McDade et al.*, 1986)
F_c	0.93	(*Nicholls*, 1965)
k_0	$1.8 \times 10^{-15}\mathrm{e}^{45/T}\ \mathrm{cm}^3\mathrm{s}^{-1}$	(*Sander et al.*, 2006)
k_3	$3.5 \times 10^{-11}\mathrm{e}^{135/T}\ \mathrm{cm}^3\mathrm{s}^{-1}$	(*Sander et al.*, 2006)
k_4	$3.9 \times 10^{-17}\ \mathrm{cm}^3\mathrm{s}^{-1}$	(*Sander et al.*, 2006)
k_6	$8 \times 10^{-14}\ \mathrm{cm}^3\mathrm{s}^{-1}$	(*Sander et al.*, 2006)
$A_{1\Sigma}$	0.085	(*Burch and Gryvnak*, 1969)

Acknowledgements

Firstly, I would like to express my sincere gratitude to my advisor Prof. Martin Riese for offering me the opportunity to study at IEK-7 and the continuous support of my Ph.D study. I would also like to thank Prof. Ralf Koppmann for accepting me into the research group at the University of Wuppertal.

Special thanks to Dr. Martin Kaufmann for introducing me the topic, encouraging my research, and allowing me to grow as a research scientist. His advice on both research as well as on my career have been invaluable.

My sincere thanks also goes to Dr. Manfred Ern and Dr. Jörn Ungermann, who gave me precious comments on my thesis and papers to be published. Without their support it would not be possible to conduct this research.

I would like to thank Dr. Yajun Zhu, Dr. Michael Deiml for their support at the beginning of my Ph.D study. I thank also Daikang Wei, Jilin Liu, Oliver Wroblowski, Qiucheng Gong, Qiuyu Chen and all my colleagues at IEK-7 and the University of Wuppertal. I enjoyed the time of working with you.

I thank the Chine Scholarship Council (CSC) and the German Academic Exchange Service (DAAD) for sponsoring my Ph.D study in Germany during the three years and a half.

Last but not least, I would like to thank my family for their unconditional support. You are the one who let me finish my degree and I will keep on trusting you for my future.

Bibliography

Alexander, M. J., and C. Barnet (2007), Using satellite observations to constrain parameterizations of gravity wave effects for global models, *Journal of the Atmospheric Sciences*, *64*(5), 1652–1665, doi:10.1175/JAS3897.1.

Alexander, M. J., J. Gille, C. Cavanaugh, M. Coffey, C. Craig, T. Eden, G. Francis, C. Halvorson, J. Hannigan, R. Khosravi, D. Kinnison, H. Lee, S. Massie, B. Nardi, J. Barnett, C. Hepplewhite, A. Lambert, and V. Dean (2008), Global estimates of gravity wave momentum flux from high resolution dynamics limb sounder observations, *Journal of Geophysical Research: Atmospheres*, *113*(D15), doi:10.1029/2007JD008807, d15S18.

Angelats i Coll, M., and J. M. Forbes (2002), Nonlinear interactions in the upper atmosphere: The s = 1 and s = 3 nonmigrating semidiurnal tides, *Journal of Geophysical Research: Space Physics*, *107*(A8), SIA 3–1–SIA 3–15, doi:10.1029/2001JA900179.

Beer, R., T. A. Glavich, and D. M. Rider (2001), Tropospheric emission spectrometer for the Earth Observing System's Aura satellite, *Applied Optics*, *40*(15), 2356, doi:10.1364/AO.40.002356.

Bucholtz, A., W. Skinner, V. Abreu, and P. Hays (1986), The dayglow of the O_2 atmospheric band system, *Planetary and Space Science*, *34*(11), 1031–1035, doi:10.1016/0032-0633(86)90013-9.

Buehler, S., P. Eriksson, T. Kuhn, A. von Engeln, and C. Verdes (2005), ARTS, the atmospheric radiative transfer simulator, *Journal of Quantitative Spectroscopy and Radiative Transfer*, *91*(1), 65–93, doi:10.1016/j.jqsrt.2004.05.051.

Burch, D. E., and D. A. Gryvnak (1969), Strengths, widths, and shapes of the oxygen lines near 13,100 cm^{-1} (7620 Å), *Appl. Opt.*, *8*(7), 1493–1499, doi:10.1364/AO.8.001493.

Campbell, I., and C. Gray (1973), Rate constants for $O(^3p)$ recombination and association with $N(^4s)$, *Chemical Physics Letters*, *18*(4), 607–609, doi:10.1016/0009-2614(73)80479-8.

Carlotti, M., B. M. Dinelli, P. Raspollini, and M. Ridolfi (2001), Geo-fit approach to the analysis of limb-scanning satellite measurements, *Applied optics*, *40*(12), 1872–1885, doi:10.1364/ORS.2001.OWC5.

Ceccherini, S., and M. Ridolfi (2010), Technical note: Variance-covariance matrix and averaging kernels for the levenberg-marquardt solution of the retrieval of atmospheric vertical profiles, *Atmospheric Chemistry and Physics*, *10*(6), 3131–3139, doi:10.5194/acp-10-3131-2010.

Chapman, S., and R. S. Lindzen (1970), *Atmospheric tides: thermal and gravitational*, D. Reidel Publishing Company, Dordrecht, Holland, doi:10.1007/978-94-010-3399-2.

Chen, S., C. E. Meek, A. H. Manson, and T. Chshyolkova (2011), The 10-day planetary wave examined by Odin/OSIRIS ozone profiles during late March 2002: comparison with UKMO and MF radar data, *International Journal of Remote Sensing*, *32*(6), 1531–1544, doi:10.1080/01431160903571817.

Christensen, A. B., J.-H. Yee, R. L. Bishop, S. A. Budzien, J. H. Hecht, G. Sivjee, and A. W. Stephan (2012), Observations of molecular oxygen Atmospheric band emission in the thermosphere using the near infrared spectrometer on the ISS/RAIDS experiment, *Journal of Geophysical Research: Space Physics*, *117*(A4), doi:10.1029/2011JA016838, a04315.

Deiml, M., R. Song, D. Fröhlich, B. Rottland, F. Wagner, J. Liu, O. Wroblowski, Q. Chen, F. Loosen, M. Kaufmann, H. Rongen, T. Neubert, H. Schneider, F. Olschweski, P. Knieling, K. Mantel, B. Solheim, G. Shepherd, R. Koppmann, and M. Riese (2017), Test of a remote sensing Fourier transform interferometer for temperature measurements in the mesosphere on a REXUS rocket, in *The 23rd ESA Symposium on European Rocket and Balloon Programmes and Related Research*, Visby, Sweden.

Eckermann, S. D., and P. Preusse (1999), Global measurements of stratospheric mountain waves from space, *Science*, *286*(5444), 1534–1537, doi:10.1126/science.286.5444.1534.

Eriksson, P., S. Buehler, C. Davis, C. Emde, and O. Lemke (2011), ARTS, the atmospheric radiative transfer simulator, version 2, *Journal of Quantitative Spectroscopy and Radiative Transfer*, *112*(10), 1551–1558, doi:10.1016/j.jqsrt.2011.03.001.

Ern, M., P. Preusse, M. J. Alexander, and C. D. Warner (2004), Absolute values of gravity wave momentum flux derived from satellite data, *Journal of Geophysical Research: Atmospheres*, *109*(D20), doi:10.1029/2004JD004752, d20103.

Ern, M., P. Preusse, J. C. Gille, C. L. Hepplewhite, M. G. Mlynczak, J. M. Russell, and M. Riese (2011), Implications for atmospheric dynamics derived from global observations of gravity wave momentum flux in stratosphere and mesosphere, *Journal of Geophysical Research: Atmospheres*, *116*(D19), doi:10.1029/2011JD015821, d19107.

Ern, M., P. Preusse, S. Kalisch, M. Kaufmann, and M. Riese (2013), Role of gravity waves in the forcing of quasi two-day waves in the mesosphere: An observational study, *Journal of Geophysical Research: Atmospheres*, *118*(9), 3467–3485, doi:10.1029/2012JD018208.

Ern, M., L. Hoffmann, and P. Preusse (2017), Directional gravity wave momentum fluxes in the stratosphere derived from high-resolution AIRS temperature data, *Geophysical Research Letters*, *44*(1), 475–485, doi:10.1002/2016GL072007, 2016GL072007.

Fetzer, E. J., and J. C. Gille (1994), Gravity wave variance in LIMS temperatures. Part I: Variability and comparison with background winds, *Journal of the Atmospheric Sciences*, *51*(17), 2461–2483, doi:10.1175/1520-0469(1994)051<2461:GWVILT>2.0.CO;2.

Fritts, D. C., and M. J. Alexander (2003), Gravity wave dynamics and effects in the middle atmosphere, *Reviews of Geophysics*, *41*(1), doi:10.1029/2001RG000106, 1003.

Fritts, D. C., D. Janches, H. Iimura, W. K. Hocking, N. J. Mitchell, R. G. Stockwell, B. Fuller, B. Vandepeer, J. Hormaechea, C. Brunini, and H. Levato (2010), Southern Argentina Agile Meteor Radar: System design and initial measurements of large-scale winds and tides, *Journal of Geophysical Research: Atmospheres*, *115*(D18), doi:10.1029/2010JD013850, d18112.

Garcia, R. R., and S. Solomon (1985), The effect of breaking gravity waves on the dynamics and chemical composition of the mesosphere and lower thermosphere, *Journal of Geophysical Research*, *90*(D2), 3850, doi:10.1029/JD090iD02p03850.

Gille, J., J. Barnett, J. Whitney, M. Dials, D. Woodard, W. Rudolf, A. Lambert, and W. Mankin (2003), The High-Resolution Dynamics Limb Sounder (HIRDLS) experiment on AURA, in *Proc. SPIE 5152, Infrared Spaceborne Remote Sensing XI*, doi:10.1117/12.507657.

Gordon, I., L. Rothman, C. Hill, R. Kochanov, Y. Tan, P. Bernath, M. Birk, V. Boudon, A. Campargue, K. Chance, B. Drouin, J.-M. Flaud, R. Gamache, J. Hodges, D. Jacquemart, V. Perevalov, A. Perrin, K. Shine, M.-A. Smith, J. Tennyson, G. Toon, H. Tran, V. Tyuterev, A. Barbe, A. Császár, V. Devi, T. Furtenbacher, J. Harrison, J.-M. Hartmann, A. Jolly, T. Johnson, T. Karman, I. Kleiner, A. Kyuberis, J. Loos, O. Lyulin, S. Massie, S. Mikhailenko, N. Moazzen-Ahmadi, H. Müller, O. Naumenko, A. Nikitin, O. Polyansky, M. Rey, M. Rotger, S. Sharpe, K. Sung, E. Starikova, S. Tashkun, J. V. Auwera, G. Wagner, J. Wilzewski, P. Wcisło, S. Yu, and E. Zak (2017), The HITRAN2016 molecular spectroscopic database, *Journal of Quantitative Spectroscopy and Radiative Transfer*, doi: http://dx.doi.org/10.1016/j.jqsrt.2017.06.038.

Green, J. G., J. Shi, and J. R. Barker (2000), Photochemical kinetics of vibrationally excited ozone produced in the 248 nm photolysis of O_2/O_3 mixtures, *The Journal of Physical Chemistry A*, *104*(26), 6218–6226, doi:10.1021/jp000635k.

Hadamard, J. (1902), Sur les problèmes aux dérivées partielles et leur signification physique, *Princeton university bulletin*, pp. 49–52.

Hagan, M. E., and J. M. Forbes (2003), Migrating and nonmigrating semidiurnal tides in the upper atmosphere excited by tropospheric latent heat release, *Journal of Geophysical Research: Space Physics*, *108*(A2), doi:10.1029/2002JA009466, 1062.

Hedin, A. E. (1991), Extension of the MSIS Thermosphere Model into the middle and lower atmosphere, *Journal of Geophysical Research: Space Physics*, *96*(A2), 1159–1172, doi:10.1029/90JA02125.

Hoffmann, L., and M. J. Alexander (2009), Retrieval of stratospheric temperatures from atmospheric infrared sounder radiance measurements for gravity wave studies, *Journal of Geophysical Research: Atmospheres*, *114*(D7), doi:10.1029/2008JD011241, d07105.

Hoffmann, P., E. Becker, W. Singer, and M. Placke (2010), Seasonal variation of mesospheric waves at northern middle and high latitudes, *Journal of Atmospheric and Solar-Terrestrial Physics*, *72*(14-15), 1068–1079, doi:10.1016/j.jastp.2010.07.002.

Hoffmann, P., M. Rapp, W. Singer, and D. Keuer (2011), Trends of mesospheric gravity waves at northern middle latitudes during summer, *Journal of Geophysical Research: Atmospheres*, *116*(D4), doi:10.1029/2011JD015717, d00P08.

Holton, J. R. (1982), The role of gravity wave induced drag and diffusion in the momentum budget of the mesosphere, *Journal of the Atmospheric Sciences*, *39*(4), 791–799, doi:10.1175/1520-0469(1982)039<0791:TROGWI>2.0.CO;2.

Hwang, E. S., A. Bergman, R. A. Copeland, and T. G. Slanger (1999), Temperature dependence of the collisional removal of $O_2(b^1\Sigma_g^+,\upsilon=1$ and 2), at 110-260 K, and atmospheric applications, *The Journal of Chemical Physics*, *110*(1), 18–24, doi:10.1063/1.478079.

Kalicinsky, C., P. Knieling, R. Koppmann, D. Offermann, W. Steinbrecht, and J. Wintel (2016), Long-term dynamics of OH^* temperatures over central Europe: trends and solar correlations, *Atmospheric Chemistry and Physics*, *16*(23), 15,033–15,047, doi:10.5194/acp-16-15033-2016.

Kalogerakis, K. S., R. A. Copeland, and T. G. Slanger (2002), Collisional removal of $O_2(b^1\Sigma_g^+,\upsilon=2,3)$, *The Journal of Chemical Physics*, *116*(12), 4877–4885, doi:10.1063/1.1456026.

Kaufmann, M., J. Blank, T. Guggenmoser, J. Ungermann, A. Engel, M. Ern, F. Friedl-Vallon, D. Gerber, J. U. Grooß, G. Guenther, M. Höpfner, A. Kleinert, E. Kretschmer, T. Latzko, G. Maucher, T. Neubert, H. Nordmeyer, H. Oelhaf, F. Olschewski, J. Orphal, P. Preusse, H. Schlager, H. Schneider, D. Schuettemeyer, F. Stroh, O. Suminska-Ebersoldt, B. Vogel, C. M. Volk, W. Woiwode, and M. Riese (2015), Retrieval of three-dimensional small-scale structures in upper-tropospheric/lower-stratospheric composition as measured by GLORIA, *Atmospheric Measurement Techniques*, *8*(1), 81–95, doi:10.5194/amt-8-81-2015.

Kernahan, J. A., and P. H.-L. Pang (1975), Experimental determination of absolute A coefficients for 'Forbidden' atomic oxygen lines, *Canadian Journal of Physics*, *53*(5), 455–458, doi:10.1139/p75-058.

Krisch, I., P. Preusse, J. Ungermann, A. Dörnbrack, S. D. Eckermann, M. Ern, F. Friedl-Vallon, M. Kaufmann, H. Oelhaf, M. Rapp, C. Strube, and M. Riese (2017), First tomographic observations of gravity waves by the infrared limb imager GLORIA, *Atmospheric Chemistry and Physics*, *17*(24), 14,937–14,953, doi:10.5194/acp-17-14937-2017.

Krupenie, P. H. (1972), The spectrum of molecular oxygen, *Journal of Physical and Chemical Reference Data*, *1*(2), 423–534, doi:10.1063/1.3253101.

Levenberg, K. (1944), A method for the solution of certain non-linear problems in least squares, *Quarterly of Applied Mathematics*, *2*(2), 164–168.

Lieberman, R. S., D. M. Riggin, and D. E. Siskind (2013), Stationary waves in the wintertime mesosphere: Evidence for gravity wave filtering by stratospheric planetary waves, *Journal of Geophysical Research: Atmospheres*, *118*(8), 3139–3149, doi:10.1002/jgrd.50319.

Lindzen, R. S. (1981), Turbulence and stress owing to gravity wave and tidal breakdown, *Journal of Geophysical Research: Oceans*, *86*(C10), 9707–9714, doi:10.1029/JC086iC10p09707.

Liu, A. Z. (2003), A modeling study of O_2 and OH airglow perturbations induced by atmospheric gravity waves, *Journal of Geophysical Research*, *108*(D4), doi:10.1029/2002JD002474.

Liu, X., J. Yue, J. Xu, W. Yuan, J. M. Russell, and M. E. Hervig (2015), Five-day waves in polar stratosphere and mesosphere temperature and mesospheric ice water measured by SOFIE/AIM, *Journal of Geophysical Research: Atmospheres*, *120*(9), 3872–3887, doi: 10.1002/2015JD023119, 2015JD023119.

Livesey, N. J., and W. G. Read (2000), Direct retrieval of line-of-sight atmospheric structure from limb sounding observations, *Geophysical Research Letters*, *27*(6), 891–894, doi:10.1029/1999GL010964.

Marquardt, D. W. (1963), An algorithm for least-squares estimation of nonlinear parameters, *Journal of the Society for Industrial and Applied Mathematics*, *11*(2), 431–441, doi:10.1137/0111030.

McDade, I., D. Murtagh, R. Greer, P. Dickinson, G. Witt, J. Stegman, E. Llewellyn, L. Thomas, and D. Jenkins (1986), ETON 2: Quenching parameters for the proposed precursors of $O_2(b_1\Sigma_g^+)$ and $O(^1S)$ in the terrestrial nightglow, *Planetary and Space Science*, *34*(9), 789–800, doi:10.1016/0032-0633(86)90075-9.

Mitchell, N. J., H. R. Middleton, A. G. Beard, P. J. S. Williams, and H. G. Muller (1999), The 16-day planetary wave in the mesosphere and lower thermosphere, *Annales Geophysicae*, *17*(11), 1447–1456, doi:10.1007/s00585-999-1447-9.

Miyoshi, Y., D. Pancheva, P. Mukhtarov, H. Jin, H. Fujiwara, and H. Shinagawa (2017), Excitation mechanism of non-migrating tides, *Journal of Atmospheric and Solar-Terrestrial Physics*, *156*, 24 – 36, doi:http://dx.doi.org/10.1016/j.jastp.2017.02.012.

Murtagh, D., G. Witt, J. Stegman, I. McDade, E. Llewellyn, F. Harris, and R. Greer (1990), An assessment of proposed $O(^1S)$ and $O_2(b^1\sum g+)$ nightglow excitation parameters, *Planetary and Space Science*, *38*(1), 43 – 53, doi:10.1016/0032-0633(90)90004-A.

Nakamura, T., A. Higashikawa, T. Tsuda, and Y. Matsushita (1999), Seasonal variations of gravity wave structures in OH airglow with a CCD imager at Shigaraki, *Earth, Planets and Space*, *51*(7), 897–906, doi:10.1186/BF03353248.

Nicholls, R. (1965), Franck-condon factors to high vibrational quantum numbers v: O2 band systems, *J. Res. Natl. Bur. Stand. Sect. A*, *69*, 369.

Pancheva, D., A. G. Beard, N. J. Mitchell, and H. G. Muller (2000), Nonlinear interactions between planetary waves in the mesosphere/lower-thermosphere region, *Journal of Geophysical Research: Space Physics*, *105*(A1), 157–170, doi:10.1029/1999JA900332.

Pautet, D., and G. Moreels (2002), Ground-based satellite-type images of the upper-atmosphere emissive layer, *Appl. Opt.*, *41*(5), 823–831, doi:10.1364/AO.41.000823.

Pejaković, D. A., E. R. Wouters, K. E. Phillips, T. G. Slanger, R. A. Copeland, and K. S. Kalogerakis (2005), Collisional removal of $O_2(b^1\Sigma_g^+$, u=1) by O_2 at thermospheric temperatures, *Journal of Geophysical Research: Space Physics*, *110*(A3), doi:10.1029/2004JA010860, a03308.

Phillips, D. L. (1962), A technique for the numerical solution of certain integral equations of the first kind, *J. ACM*, *9*(1), 84–97, doi:10.1145/321105.321114.

Placke, M., P. Hoffmann, E. Becker, C. Jacobi, W. Singer, and M. Rapp (2011), Gravity wave momentum fluxes in the MLT—Part II: Meteor radar investigations at high and midlatitudes in comparison with modeling studies, *Journal of Atmospheric and Solar-Terrestrial Physics*, *73*(9), 911 – 920, doi:http://dx.doi.org/10.1016/j.jastp.2010.05.007, scientific Results from Networked and Multi-instrument studies based on MST Radar.

Preusse, P., A. Dörnbrack, S. D. Eckermann, M. Riese, B. Schaeler, J. T. Bacmeister, D. Broutman, and K. U. Grossmann (2002), Space-based measurements of stratospheric mountain waves by CRISTA 1. Sensitivity, analysis method, and a case study, *Journal of Geophysical Research: Atmospheres*, *107*(D23), doi:10.1029/2001JD000699, 8178.

Puķīte, J., S. Kühl, T. Deutschmann, S. Dörner, P. Jöckel, U. Platt, and T. Wagner (2010), The effect of horizontal gradients and spatial measurement resolution on the retrieval of global vertical NO_2 distributions from SCIAMACHY measurements in limb only mode, *Atmospheric Measurement Techniques*, *3*(4), 1155–1174, doi:10.5194/amt-3-1155-2010.

Remsberg, E. E., L. L. Gordley, B. Marshall, R. Thompson, J. Burton, P. Bhatt, V. Harvey, G. Lingenfelser, and M. Natarajan (2004), The Nimbus 7 LIMS version 6 radiance conditioning and temperature retrieval methods and results, *Journal of Quantitative Spectroscopy and Radiative Transfer*, *86*(4), 395 – 424, doi:http://dx.doi.org/10.1016/j.jqsrt.2003.12.007.

Riese, M., H. Oelhaf, P. Preusse, J. Blank, M. Ern, F. Friedl-Vallon, H. Fischer, T. Guggenmoser, M. Höpfner, P. Hoor, M. Kaufmann, J. Orphal, F. Plöger, R. Spang, O. Suminska-Ebersoldt, J. Ungermann, B. Vogel, and W. Woiwode (2014), Gimballed Limb Observer for Radiance

Imaging of the Atmosphere (GLORIA) scientific objectives, *Atmospheric Measurement Techniques*, *7*(7), 1915–1928, doi:10.5194/amt-7-1915-2014.

Rocken, C., R. Anthes, M. Exner, D. Hunt, S. Sokolovskiy, R. Ware, M. Gorbunov, W. Schreiner, D. Feng, B. Herman, Y.-H. Kuo, and X. Zou (1997), Analysis and validation of GPS/MET data in the neutral atmosphere, *Journal of Geophysical Research: Atmospheres*, *102*(D25), 29,849–29,866, doi:10.1029/97JD02400.

Rodgers, C. D. (2000), *Inverse methods for atmospheric sounding: theory and practice*, vol. 2, World scientific.

Rodrigo, R., J. Lopez-Moreno, M. Lopez-Puertas, F. Moreno, and A. Molina (1986), Neutral atmospheric composition between 60 and 220 km: A theoretical model for mid-latitudes, *Planetary and Space Science*, *34*(8), 723 – 743, doi:http://dx.doi.org/10.1016/0032-0633(86)90126-1.

Sander, S., D. Golden, M. Kurylo, G. Moortgat, P. Wine, A. Ravishankara, C. Kolb, M. Molina, B. Finlayson-Pitts, R. Huie, et al. (2006), Chemical kinetics and photochemical data for use in atmospheric studies evaluation number 15, *Tech. rep.*, Pasadena, CA: Jet Propulsion Laboratory, National Aeronautics and Space Administration, 2006.

Smith, F. L., and C. Smith (1972), Numerical evaluation of Chapman's grazing incidence integral ch(X, χ), *Journal of Geophysical Research*, *77*(19), 3592–3597, doi:10.1029/JA077i019p03592.

Stamnes, K., G. E. Thomas, and J. J. Stamnes (2017), *Radiative Transfer in the Atmosphere and Ocean*, 2 ed., Cambridge University Press, doi:10.1017/9781316148549.

Strong, K., B. M. Joseph, R. Dosanjh, I. C. McDade, C. A. McLinden, J. C. McConnell, J. Stegman, D. P. Murtagh, and E. J. Llewellyn (2002), Retrieval of vertical concentration profiles from OSIRIS UV-visible limb spectra, *Canadian Journal of Physics*, *80*(4), 409–434, doi:10.1139/p01-153.

Suzuki, S., K. Shiokawa, Y. Otsuka, T. Ogawa, and P. Wilkinson (2004), Statistical characteristics of gravity waves observed by an all-sky imager at Darwin, Australia, *Journal of Geophysical Research: Atmospheres*, *109*(D20), doi:10.1029/2003JD004336, d20S07.

Suzuki, S., T. Nakamura, M. K. Ejiri, M. Tsutsumi, K. Shiokawa, and T. D. Kawahara (2010), Simultaneous airglow, lidar, and radar measurements of mesospheric gravity waves over Japan, *Journal of Geophysical Research: Atmospheres*, *115*(D24), doi:10.1029/2010JD014674, d24113.

Tikhonov, A. N., and V. I. Arsenin (1977), *Solutions of ill-posed problems*, Scripta series in mathematics, Winston ; distributed solely by Halsted Press, Washington : New York.

Tsuda, T., M. Nishida, C. Rocken, and R. H. Ware (2000), A global morphology of gravity wave activity in the stratosphere revealed by the GPS occultation data (GPS/MET), *Journal of Geophysical Research: Atmospheres*, *105*(D6), 7257–7273, doi:10.1029/1999JD901005.

Tunbridge, V. M., D. J. Sandford, and N. J. Mitchell (2011), Zonal wave numbers of the summertime 2 day planetary wave observed in the mesosphere by EOS Aura Microwave Limb Sounder, *Journal of Geophysical Research: Atmospheres*, *116*(D11), doi:10.1029/2010JD014567, d11103.

Twomey, S. (1963), On the numerical solution of fredholm integral equations of the first kind by the inversion of the linear system produced by quadrature, *J. ACM*, *10*(1), 97–101, doi:10.1145/321150.321157.

Ungermann, J., L. Hoffmann, P. Preusse, M. Kaufmann, and M. Riese (2010), Tomographic retrieval approach for mesoscale gravity wave observations by the PREMIER Infrared Limb-Sounder, *Atmospheric Measurement Techniques*, *3*(2), 339–354, doi:10.5194/amt-3-339-2010.

Ungermann, J., J. Blank, J. Lotz, K. Leppkes, L. Hoffmann, T. Guggenmoser, M. Kaufmann, P. Preusse, U. Naumann, and M. Riese (2011), A 3-D tomographic retrieval approach with advection compensation for the air-borne limb-imager GLORIA, *Atmospheric Measurement Techniques*, *4*(11), 2509–2529, doi:10.5194/amt-4-2509-2011.

Vallance Jones, A. (1974), Aurora geophysics and astrophysics monographs, *D. Reidel, Hingham, Mass.*

Vargas, F., G. Swenson, A. Liu, and D. Gobbi (2007), O(^{1}S), OH, and O_2(b) airglow layer perturbations due to AGWs and their implied effects on the atmosphere, *Journal of Geophysical Research*, *112*(D14), doi:10.1029/2006JD007642.

Vincent, R. A. (2015), The dynamics of the mesosphere and lower thermosphere: a brief review, *Progress in Earth and Planetary Science*, *2*(1), doi:10.1186/s40645-015-0035-8.

Ward, W. E. (1999), A simple model of diurnal variations in the mesospheric oxygen nightglow, *Geophysical Research Letters*, *26*(23), 3565–3568, doi:10.1029/1999GL003661.

Waters, J. W., W. G. Read, L. Froidevaux, R. F. Jarnot, R. E. Cofield, D. A. Flower, G. K. Lau, H. M. Pickett, M. L. Santee, D. L. Wu, M. A. Boyles, J. R. Burke, R. R. Lay, M. S. Loo, N. J. Livesey, T. A. Lungu, G. L. Manney, L. L. Nakamura, V. S. Perun, B. P. Ridenoure, Z. Shippony, P. H. Siegel, R. P. Thurstans, R. S. Harwood, H. C. Pumphrey, and M. J. Filipiak (1999), The UARS and EOS Microwave Limb Sounder (MLS) experiments, *Journal of the Atmospheric Sciences*, *56*(2), 194–218, doi:10.1175/1520-0469(1999)056<0194:TUAEML>2.0.CO;2.

Wright, C. J., S. M. Osprey, J. J. Barnett, L. J. Gray, and J. C. Gille (2010), High Resolution Dynamics Limb Sounder measurements of gravity wave activity in the 2006 Arctic stratosphere, *Journal of Geophysical Research: Atmospheres*, *115*(D2), doi:10.1029/2009JD011858, d02105.

Wu, D. L. (2004), Mesoscale gravity wave variances from AMSU-A radiances, *Geophysical Research Letters*, *31*(12), doi:10.1029/2004GL019562, l12114.

Yankovsky, V. A., and R. O. Manuilova (2006), Model of daytime emissions of electronically-vibrationally excited products of O_3 and O_2 photolysis: application to ozone retrieval, *Annales Geophysicae*, *24*(11), 2823–2839, doi:10.5194/angeo-24-2823-2006.